UNIVERSITY OF OKLAHOMA

GRADUATE COLLEGE

# MODULAR OPTICAL WIRELESS ELEMENTS

A DISSERTATION

SUBMITTED TO THE GRADUATE FACULTY

in partial fulfillment of the requirements for the

Degree of

DOCTOR OF PHILOSOPHY

in

Electrical and Computer Engineering

By

**Asaad Kaadan**

Norman, Oklahoma

2016

**MODULAR OPTICAL WIRELESS ELEMENTS**

A DISSERTATION APPROVED FOR THE

SCHOOL OF ELECTRICAL AND COMPUTER ENGINEERING

BY

Dr. Hazem Refai, Chair

Dr. Peter LoPresti

Dr. Thordur Runolfsson

Dr. Ali Imran

Dr. William Ray

TO THE TWO PEOPLE WHO MADE ME WHO I AM TODAY... **MOM & DAD**,

TO MY BELOVED **SISTERS** & MY DEAR **BROTHER**,

TO **THE LOVE** OF MY LIFE... I FINALLY FOUND YOU!,

TO ALL MY **TEACHERS** & **MENTORS**,

AND TO MY HEARTBROKEN LAND **SYRIA**,

I DEDICATE THIS WORK.

ASAAD

# Acknowledgements

I would like to extend my heartfelt thanks and sincere gratitude to my adviser **Dr. Hazem Refai** for his nurturing, support, and mentorship over the years and for believing in this project and supporting it even without external funding. This work would not have been possible without his vision and guidance. In addition, I extend sincere appreciation to my Ph.D. committee members **Dr. Peter LoPresti**, **Dr. Thordur Runolfsson**, **Dr. Ali Imran** and **Dr. William Ray** for their time and insightful comments. Appreciation goes as well to **Michelle Farabough** for editing this dissertation and for her supportive and educating comments over the years.

As always, every scientific achievement is the outcome of many people involved. Thus, I am grateful for help and every piece of advice I received from **Dr. Peter LoPresti and his team** at Tulsa University; **Fahed Babelli**, **Naim Bitar**, **Walid Balid** and **Nishaal Palmer** at Oklahoma University; and **Brady Deetz and his team** at the **Tandy Supercomputing Center** in Tulsa, Oklahoma.

To my extended OU family... professors, students and staff... my sincere appreciation to all of you.

# Contents

# List of Tables

# List of Figures

# Abstract

Optical wireless has gained attention in recent years as an efficient and secure way to provide broadband connectivity to mobile platforms, isolated communities, and crowded public events. Companies like NASA, Google, Facebook, and others have demonstrated its potential. However, current optical wireless technology remains mostly heavy, bulky, and expensive, making it impractical for many scenarios and inaccessible to most students/researchers.

This work presents the concept of *Modular Optical Wireless Elements* (MOWE), a novel system composed of multiple electrically interconnected optical modules (i.e., elements) forming a flat or curved terminal that is inexpensive, lightweight, and easy-to-assemble. The technology enables cost-effective access to wide field-of-view optical communication for last-mile broadband connectivity. Smart modules provide reconfigurability, as well as local and central processing capabilities. The modules enable innovative short- and medium-range applications for free-space optics (FSO) in indoor communication and navigation, MIMO, and optical sensing, among others. This dissertation introduces the MOWE concept and provides in-depth information about modeling, analysis, hardware, and firmware, along with proof-of-concept examples and demonstrations. The notions of software-defined optics and cognitive optics are introduced and analyzed in a MOWE context. Several experiments and case studies covering a wide spectrum of applications−from intelligent power control to passive beam steering−are presented in detail. This dissertation also discusses the future of MOWE technology and suggests possible improvements for high performance systems.

# Chapter 1: Introduction

## 1.1. Background

Free-space optical (FSO) communication has primarily been considered for long-range and fixed (or partially-mobile) point-to-point terrestrial and satellite applications where terminals are heavy, bulky, and expensive [1–4]. Vast opportunities, however, lie in the short-range, last-mile market where mobile users seek wireless broadband connectivity at the lowest cost, smallest size, lightest weight, and with minimal power consumption.

Although dominated by traditional radio frequency (RF) communication, the mobile wireless broadband market increasingly faces difficult challenges (e.g., a crowded, expensive spectrum; privacy leaks; security concerns; power consumption; miniaturization; and interference issues, among others). One solution is going higher in the electromagnetic spectrum toward mmWave, microwave, and even light waves. Directional communication technologies have many clear advantages relative to security, interference, spectrum availability, power consumption, and antenna size. Mobility, however, becomes a real challenge, especially as you go up in the spectrum and the wavelength shrinks considerably.

FSO is clearly not competitive for mobile applications when compared with RF, mmWave, and microwave. Nonetheless, it has the highest bandwidth and a free spectrum. Another advantage for FSO is that light, unlike radio, already has many other applications in our daily life: indoor and street lighting, photography, and remote sensing, just to name a few.

## 1.2. Related Work

Gimbals are the state-of-the-art alignment and tracking solution for aerial photography, astronomy, and long-range FSO links, among others [5–8]. These mechanical devices, however, lack the appropriate size, weight, and power (SWaP) specifications for most mobile wireless broadband applications. One method to overcome light directionality without reverting to gimbals is to exploit spatial diversity of multiple optical antennas [9] (i.e., *Optical Arrays*). We will review next the candidate technologies for optical arrays and discuss the pros and cons of each one.

### *1.2.1 Photonics Integrated Circuits*

Advantages of spatially distributed optical arrays were first recognized with the introduction of semiconductor laser arrays [10–12]. Currently, different wavelength lasers can be assembled on the same monolithic integrated circuit [13] (i.e., large-scale photonics integrated circuits [PIC]), which enable wavelength and spatial diversity. A focal-point array (FPA) refers to the assembly of individual detector picture elements (i.e., pixels) located at the focal plane of an imaging system. Monolithic FPAs have achieved extremely high integration, yielding resolution as high as 2 gigapixels for charge coupled devices (CCDs) and 147 megapixels for infrared arrays targeted at astronomy applications [14] (See Figure 1.1). Monolithic integration of semiconductor-based optical transceivers, however, is a costly process requiring significant initial investments. Because the process is not scalable beyond chip dimensions, its use is

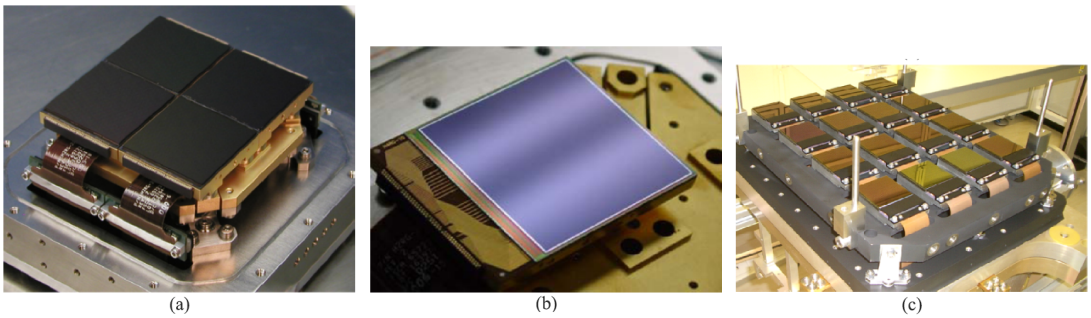

(a) (b) (c)

**Figure 1.1. Multiple large FPAs used for astronomy observations: (a) four Hawaii-2RG-18 (4096×4096 pixels, 18-$\mu$m pitch), (b) Hawaii-4RG-10 (4096×4096 pixels, 10-$\mu$m pitch), and (c) sixteen 2048×2048 HgCdTe arrays assembled for the VISTA telescope (Reproduced from [14]).**

inappropriate for large optical apertures in non-imaging systems.

### *1.2.2 Bio-inspired Optics*

Biologically inspired optics is a field of research attempting to mimic nature-like sophisticated imaging systems, achieving wide FoV, supporting mobility, and providing tracking and localization information at the lowest SWaP [15, 16]. Advances in materials science allow integration of hundreds of optical receivers on curved elastic geometries (e.g., elastomeric microlens arrays [17, 18]), which provide a nearly hemispherical (about 160°) FoV mimicking arthropod eye. University of California, Berkeley researchers created an array of tunable microdoublet lenses to create dual modes of biconvex or meniscus lenses that can be used in artificial compound eyes [19, 20] (See Figure 1.2). Novel Biomimetic Gradient Index (GRIN) Lenses have also been developed by scientists at the Naval Research Laboratory (NRL). The purpose is to replace current lens systems with those composed of fewer and lighter lenses [21]. Although biomimetic arrays are expected to yield substantial advancements in low-SWaP optical imaging, detection, and tracking systems, there is no practical way to extend the design toward a transceiver system. The very special advantage of biomimetic optics (i.e., using elastic non-rigid materials) might be a disadvantage for

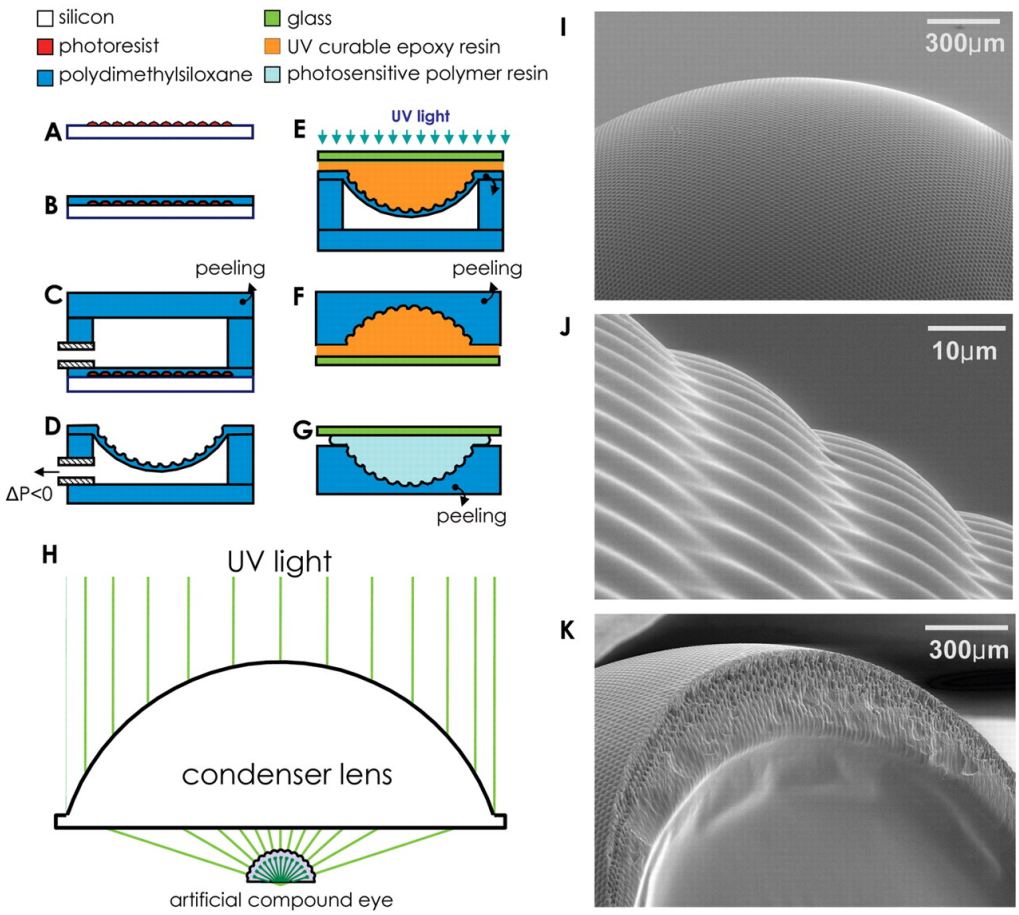


**Figure 1.2. An artificial compound eye developed by the BioPOETS lab at the University of California, Berkeley [20]. On the left, 3D polymer synthesis of biomimetic artificial compound eyes is illustrated. Pictures on the right show spherical arrangement of 8370 artificial ommatidia (eye elements) consisting of microlenses, polymer cones, and waveguide arrays assembled on a hemispherical polymer dome 2.5 mm in diameter.**

many applications that require a rigid structure.

### *1.2.3 Fiber-optic Bundles*

Fiber bundle technology is a strong candidate for mobile FSO communication, and several research groups have been actively working in this area. A collaborative effort between the University of Oklahoma and Tulsa University has resulted in an all-optical receiver fiber bundle design with optical combining and a related lens system [22, 23]. The group also developed a transmitter fiber bundle with various optical

switching schemes in [24]. Both bundles are shown during an outdoor test in Figure 1.3. Direct optical coupling of fiber bundles is discussed by Takahashi and Nakajima in [25]. Heng et al. used sets of MEMS-based switches and microlens arrays to control beam splitting and propagation through multiple fibers [26]. Johns Hopkins University Applied Physics Laboratory (APL) has developed a receiver fiber-bundle system with piezoelectric-controlled microlenses to optimize power coupling into a given fiber core, allowing relative motion between the transmitter and receiver [27, 28]. Even though fiber bundle-based transceiver technology is much faster than semiconductor-based, the technology is still in its infancy with many barriers to commercialization (e.g., high cost of fibers and lenses, precision assembly requirements, and limited coverage, as well as scalability and manufacturability challenges).

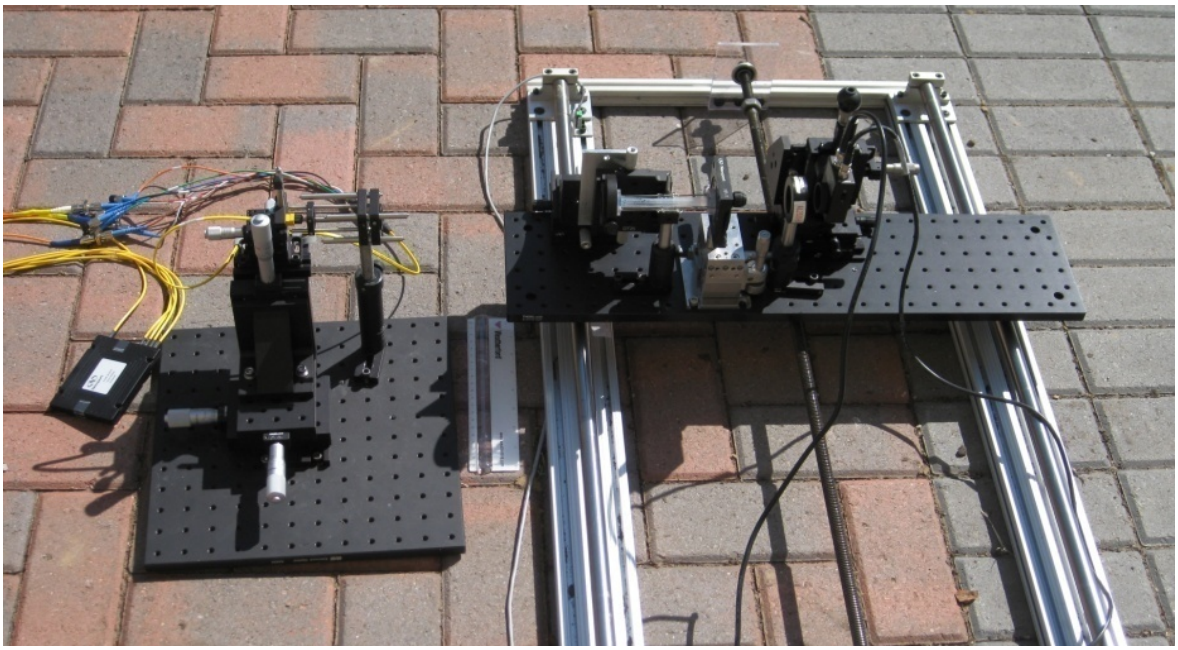

**Figure 1.3. A receiver fiber-bundle (right) and a transmitter fiber-bundle (left) being tested outdoors at Tulsa University campus [29]. The receiver consists of 19 fibers in a hexagonal pattern while the transmitter is a linear stripe of 8 fibers, laid out horizontally.**

### *1.2.4 Electrically-interconnected Optical Arrays*

LEDs (light-emitting diodes), VCSELs (vertical cavity surface emitting lasers), PDs (photo diodes), and PTs (photo transistors) can be assembled on separate printed circuit boards (PCBs) that are spatially positioned in different geometries, resulting in an optical array that is interconnected electrically. This solution, although slower than all-optical solutions, such as fiber bundles, is inexpensive, scalable, and within reach of current technology. Transceiver boards were assembled in a spherical configuration in [31, 32] and in a cylindrical configuration in [33]. The latter work did not provide implementation details to prove feasibility. The former work by the University of Nevada is, to this author's knowledge, the most extensive: Researchers in [34] developed line-of-sight (LoS) alignment and tracking algorithms for their spherical terminals and analyzed crosstalk among neighboring transceivers. They also performed theoretical analysis and simulation of coverage, node density, and network

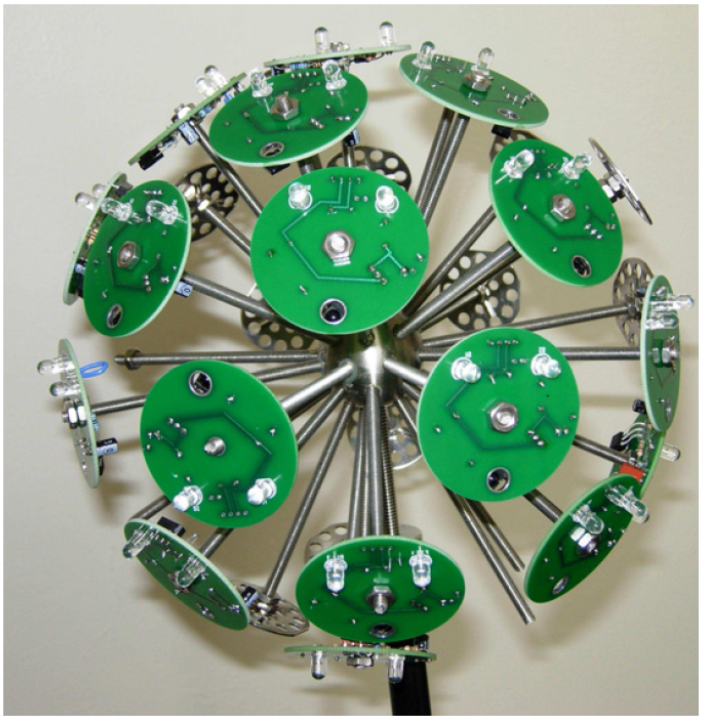

**Figure 1.4. A picture of the prototype optical antenna developed by the University of Nevada in [30].**

end-to-end performance in [31, 35], and proposed 3D optical localization in [36]. Although the group provided implementation details in [30] (shown in Figure 1.4), their proposed concept is not scalable and does not accommodate various geometrical configurations (e.g., non-spherical and flat terminals). Weight and size of supporting structure constrains and limits the number of possible applications. Furthermore, no clear pathway is provided to reduce technology cost and barriers-to-market, which are essential for mass adoption.

### *1.2.5 Mobile Platforms and Optical Arrays*

Although mobile platforms include ground- and air-based vehicles, it is in aerial communication that we can leverage the full potentials of FSO since optical blocking is less likely to occur in free space high above the ground. Some aerial platforms (e.g., multirotor UAVs), however, are particularly challenging for FSO. The combination of fast dynamics, high instability, and payload weight and power restrictions make these vehicles unable to benefit from state-of-the-art mechanical pointing, acquisition, and tracking (PAT) solutions.

In previous works [37,38], I analyzed the effects of platform dynamics and attitude deviation on the mutual alignment of two multirotors—a quantity directly related to FSO link performance. Since present day FSO communication technology is too heavy for small multirotors, a different approach using pixelated optical arrays was explored. Optical elements assembled in array-fashion can provide a wide FoV to compensate for platform attitude noise and instability. Optical and/or electrical switching can replace heavy and bulky mechanical gimbals for steering and alignment. An open-loop stability/alignment model for a flat transmitter and a flat receiver array was developed in [9]. Analytical stability/alignment models for a spherically shaped receiver array and a flat transmitter array were also introduced in [39].

### 1.3. Modular Optical Wireless Elements

I set forth to develop a low-SWaP optical wireless communication technology that is suitable for small mobile platforms and, at the same time, takes advantage of current advances in semiconductors, photonics, and abundant computing resources. After I proved the utility of optical arrays for mobile/unstable platforms in [9, 39] and the University of Nevada team showed feasibility of a spherical optical terminal in [30], it was clear that the best way forward is building an optical array using mainly semiconductor components. The main question was, however, how to efficiently design and build such an array in a scalable matter?

Inspired by nature, I found that *modularity* is the answer. Basic geometric elements (e.g., hexagons, pentagons and triangles, among others) are used by nature to create modular flat and curved surfaces at various scales and for various utilities. My proposed solution, Modular Optical Wireless Elements (MOWE) [40], is a scalable, modular architecture that utilizes smart optical modules (transmitters and receivers) to build a variety of larger structures. These shell-like structures could be made flat, spherical, or in any geometric shapes that can be created from individual, smaller elements (modules). The proposed architecture is built around a community-based development model, which is uncommon in optical wireless. The LEGO-like modular system offers students and researchers an economic access to optical wireless and FSO for research and development. The system is available as open-source and aims to stimulate the community to develop innovative solutions for real-life challenges, such as spectrum scarcity, remote Internet access, and post-disaster emergency communication, among other applications.

Figure 1.5 shows individual MOWE modules of various shapes and sizes (1.1.E), as well as an assembled array (1.1.D). The figure also illustrates natural implementations of the modularity concept that was borrowed to create MOWE. Flat and curved

modular hexagonal surfaces are common in nature, whether in insect eyes (1.1.A), plants and animals (1.1.C), or on a molecular level (1.1.B).

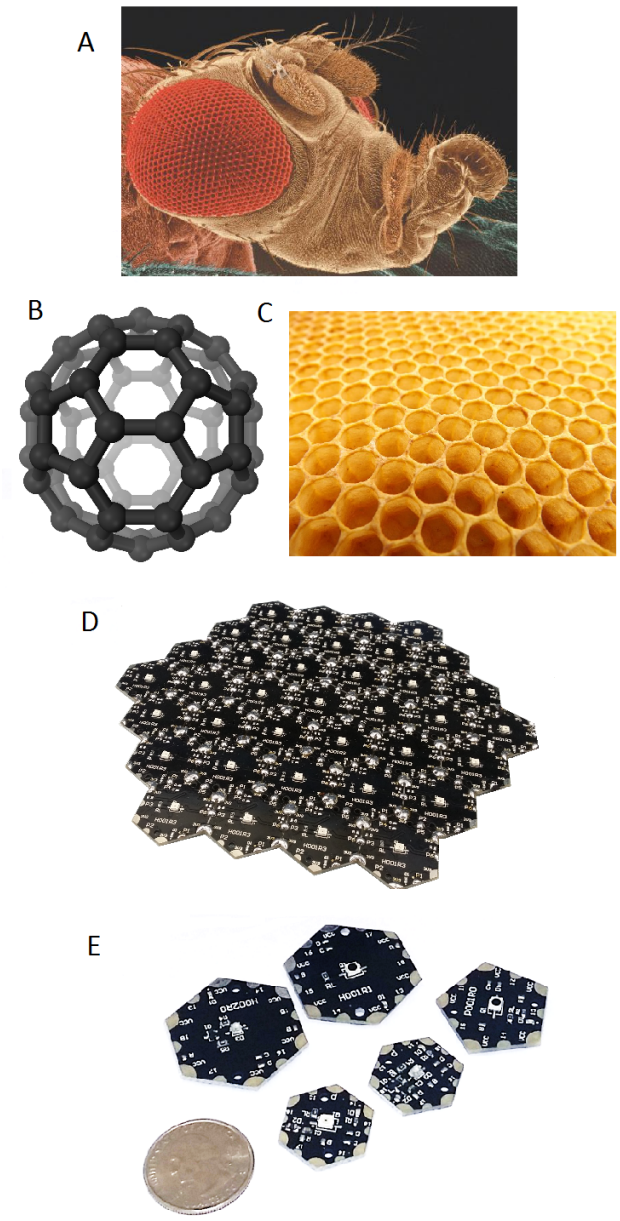


**Figure 1.5. Modularity in nature and optics.**

**A: Each compound eye of the fruit fly contains 760 hexagonal unit eyes (i.e., ommatidia) [41]. B: The Buckminsterfullerene ($C_{60}$) long-chain carbon molecule [42]. C: Honeycomb structure in a beehive. D: MOWE-based flat hexagonal detector array. E: Individual MOWE modules pictured aside a US quarter dollar for size comparison.**

### *Motivation for an Open-source Solution*

FSO communication has long been a science field restricted to mainly large government-funded projects with most applications in military and space domains. As a result, access to this field was restricted to only those lucky few who could afford the cost and navigate the logistics. This has stalled development efforts in civilian and terrestrial optical wireless applications, especially with the severe reduction of research funds and budgets during the last decade.

These limitations began to change recently, however, with the elevated interest in commercial applications of optical wireless and with additional funds available from industry. RF spectrum scarcity, the ever-increasing demand for bandwidth, and privacy issues have spurred recent interest in visible-light communication (VLC) [43–45]. Ambitious projects undertaken by industry giants (e.g., Google [46] and Facebook [47]), have brought optical wireless to center-stage, attempting to solve extreme challenges such as global Internet connectivity. Nevertheless, the field is still dominated by large research groups (i.e., well-funded companies and universities), and there is little space for individual creativity and community makers and tinkerers.

The maker movement, cherished by other research fields (e.g., robotics, embedded systems, and software-defined radio−the well-known Gnu Radio [48]), has stemmed numerous innovations so far, unlike in the optical wireless domain where community-based efforts are still scarce. This is due to the prohibitive logistical and cost barriers to enter the field. Open-source projects are more common on the software and protocol side. One notable example is the OpenVLC project [49], which provides a rich software library for visible light communication running on a BeaglBone board and a standard optical transceiver module. However, given all recent advances in embedded computing, semiconductors, and laser technology, our research group thinks the time has come to start a community-based initiative to foster innovation and creativity using a more flexible optical wireless hardware architecture.

## 1.4. Contributions

Contributions of this dissertation can be summarized, as follows:

### *Concept, Theory, & Analysis*

1. Developing the concept of a modular optical wireless communication system that facilitates designing flat, curved, and spherical optical arrays out of modular basic elements with specific geometries.

2. Modeling and characterization of combined FoV and other optical properties of flat and truncated icosahedron-based spherical optical arrays.

3. Introducing the concepts of Software-defined Optics (SDO) and Cognitive Optics (CO) while comparing and contrasting with Software-defined Radio and Cognitive Radio.

4. Introducing the concept of hybrid optical/electrical arrays by combining MOWE with fiber-optic bundles.

5. Analyzing the path toward next generation of high-performance MOWE and discussing research directions, including possible integration with Gnu Radio.

### *Design & Implementation*

1. Hardware designing, fabricating, and testing of multiple MOWE modules.

2. Designing, assembling, and testing of various wide-area optical detector arrays with flat, spherical, and tube shapes, including optically inhomogeneous arrays.

3. Designing and testing multiple structural and protecting plastic frames, holders, and fixtures for MOWE arrays.

4. Developing a real-time operating system for MOWE that integrates a FreeRTOS core, peripheral drivers, command line interface, and application level APIs.

***Testing & Experiments***

1. Measuring and characterizing various optical and electrical properties of MOWE modules and arrays.

2. Conducting multiple experiments for passive and active optical beam detection, tracking and measurement with various MOWE arrays.

3. Demonstrating passive optical beam switching with less than $10\mu sec$ switching time.

4. Demonstrating a closed-loop passive optical beam steering and alignment using inertial measurement unit (IMU) sensor (gyroscope and accelerometer) and a complementary data-fusion filter.

5. Designing a closed-loop active optical beam steering system using fine steering mirrors and an optimal controller.

6. Building a misalignment testbed to test against random and known misalignment affecting MOWE arrays in real-life scenarios. The testbed is controllable through servo motors and MOWE modules.

7. Designing and building an optical receiver that decodes two overlapping signals by utilizing wavelength diversity.

8. Designing and building a cognitive optical terminal that employs machine learning to adapt its power according to the environment.

***Publications***

1. All MOWE schematics, firmware, and mechanical designs are available to the community as open-source materials on the famous code-sharing website GitHub; the website contains a detailed wiki that explains setup, connection, and various projects: http://ouwecad.github.io/MOWE/.

2. Design framework and templates for MOWE detector arrays of any shape and size are available on the project website to help shorten design time.

3. This project resulted in the following publications:

   - **A. Kaadan**, H. H. Refai and P. G. LoPresti, "*Wide-area and Omnidirectional Optical Detector Arrays using Modular Optical Elements*," Journal of Appl. Opt. 55, 4791-4800 (2016).
   - **A. Kaadan**, H. H. Refai, and P. G. LoPresti, "*Spherical FSO Receivers for UAV Communication: Geometric Coverage Models*," IEEE Transactions on Aerospace and Electronics Systems, vol. 52, 2016.
   - **A. Kaadan**, H. H. Refai and P. G. LoPresti, "*On the Development of Modular Optical Wireless Elements (MOWE)*," 2015 IEEE Globecom Workshops (GC Wkshps), San Diego, CA, USA, 2015, pp. 1-7.
   - **A. Kaadan**, H. H. Refai and P. G. LoPresti, "*Multielement FSO Transceivers Alignment for Inter-UAV Communications*," Lightwave Technology, Journal of, vol.32, no.24, pp.4785,4795, Dec.15, 2014.
   - **A. Kaadan**, D. Zhou, H. H. Refai, and P. G. LoPresti, "*Modeling of aerial-to-aerial short-distance free-space optical links*," in Integrated Communications, Navigation and Surveillance Conference (ICNS), 2013, 2013, pp. 1-12.

4. MOWE won an **Honorary Mention** at the **2015 IEEE ComSoc Student Competition** "*Communications Technology Changing the World*." The project was ranked among the top nine projects from nearly 50 original works submitted worldwide.

This dissertation will further introduce the concept of modular optical wireless elements (MOWE) in Chapter 2. MOWE hardware specifications and software architecture are discussed in Chapter 3. Chapter 4 features a detailed case study about wide-area and omnidirectional optical detector arrays for optical detection and motion tracking applications. Chapter 5 introduces the concept of software and cognitive optics with detailed analysis and comparisons with their RF counterparts. Then, Chapter 6 presents various demonstrations and experiments showcasing some MOWE potentials and applications. Finally, Chapter 7 discusses the future of MOWE and the path toward next generation high-performance arrays. The chapter also discuses other interesting concepts, such as hybrid arrays and Gnu Optics. The dissertation concludes in Chapter 8. Two appendices are included to explain nomenclature used herein and to guide readers through the MOWE website.

# Chapter 2: Modular Optical Wireless Elements Concept

A single *array* is composed of multiple *modules* soldered side-by-side to form a single, continuous flat or curved surface that could be structurally supported by a 3D-printed plastic *frame*. The array, frame, and a *central controller* with wired or wireless interface constitute a complete optical *terminal*. The MOWE concept is depicted in Figure 2.1.

## 2.1. The Optical Module

Modules come in specific, standard polygonal shapes (e.g., hexagons, pentagons, and triangles) to form contiguous surfaces. Each module serves as a single optical point−either transmitter, receiver, or transceiver. Transmitters can be either LEDs for short-range communication or VCSELs for longer range and higher output power.

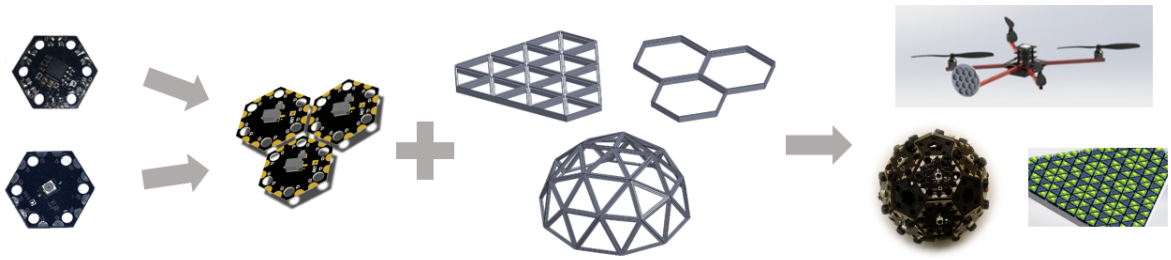

**Figure 2.1. Modular optical wireless elements concept.**

***From left to right*: Individual modules are assembled into an array. Arrays are fitted with structural 3D-printed frames. Arrays and frames make a complete terminal that can be used in various applications, e.g., on board a multirotor UAV.**

Receivers are photo diodes (or photo transistors) with high responsivity at visible or infrared light. Both transmitters and receivers are surface-mounted devices with small form factor to free the underside (bottom) of the PCB, accommodating additional electronics. Although a single module might have multiple VCSELs/LEDs/PDs to increase transmission power or receiver sensitivity, it is still considered and treated as single optical point when integrated within an array.

Figure 2.2 shows top-bottom illustrations of several modules fashioned from a variety of shapes and sizes. Hexagon modules shown in (a) and (d) have a short diagonal (or side-to-side width−a quantity we call *Optical Resolution*) of $20mm$; hexagons in (b) and (e) have a width of $30mm$. Pentagons in (c) and (f) are compatible with $30mm$-hexagons. The module topside holds the optical front-end (e.g., LED, VCSEL or PD) precisely at the center of the board, while a microcontroller (MCU) and other electronic components are placed on the bottom side. Optical modules are free from connectors, wires, cables, and any other assemblies, rendering them as small and lightweight as possible. *Edge pcb connectors* are small areas of exposed copper positioned at module edges and sides for physically and electrically connecting adjacent modules. Larger edge connectors are used for power connection, while smaller ones are used for signal connection and networking. Hardware and firmware are designed so that the optical module connects with other modules using any of its side ports, regardless of its orientation. The only constraint is to solder all modules facing the same direction (upwards or downwards).

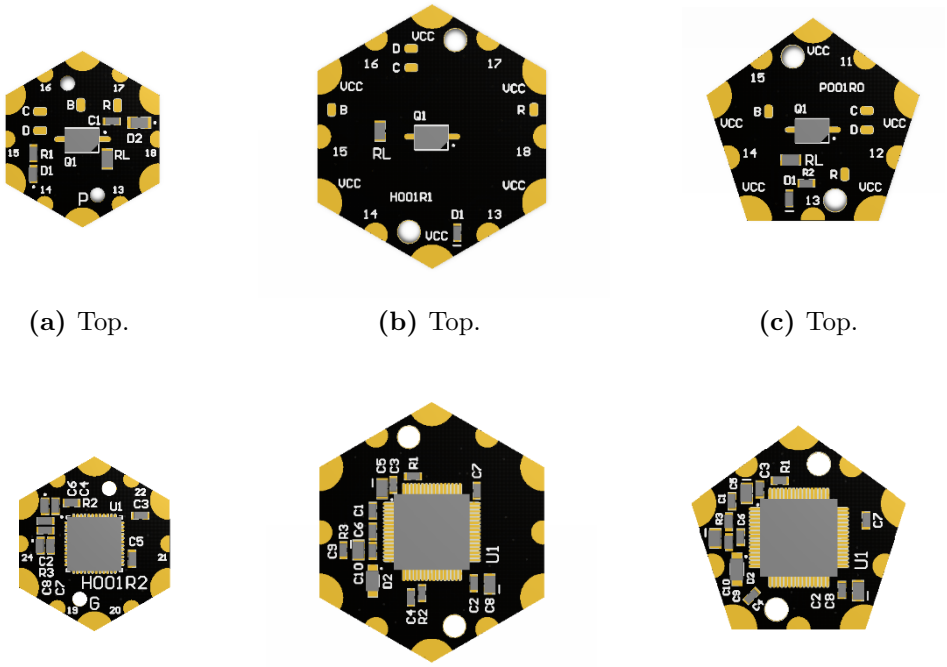


**(a)** Top. **(b)** Top. **(c)** Top.

**(d)** Bottom. **(e)** Bottom. **(f)** Bottom.

**Figure 2.2. 3D illustration of optical modules (Scale 1:1).**

Modules communicate with each other using an asynchronous half duplex or full duplex serial protocol. Given a hexagon shape, each MCU employs six serial ports to communicate with neighboring modules. A direct memory access (DMA) controller manages data transfers between ports with minimal CPU intervention, making the modules *invisible* for transit traffic and enabling non-adjacent modules to connect seamlessly with one another. The MCU within each module renders it as a smart module, not merely an I/O point. Basic calculations can be run locally (e.g., noise cancellation, channel coding, and signal modulation/demodulation, among others), while higher-level functionality are managed by a central controller. A complete distributed sensing and control architecture is also possible, where all algorithms run locally and the central controller is merely used as an interface with the outside world.

## 2.2. The Optical Array

Hexagons can be used to construct flat arrays (i.e., beehive-like structures). Hexagons and pentagons are used to create spherical arrays. A full spherical array (e.g., soccer ball or truncated icosahedron) is composed of 20 hexagons and 12 pentagons. Triangles are also used to create spherical arrays called geodesic spheres or geodesic domes.

Modules can be soldered horizontally to create flat arrays or at a specific angle to form curved arrays. The array is usually homogeneous, meaning that any module can be used as an I/O module to interface the array with the central controller. Although the configuration of some arrays could be self-supporting with merely solder joints, additional structural support could be provided via special 3D-printed plastic frames that take on the surface shape for added support and protection. These hollow structures add minimal overhead weight to the terminal. Figure 2.3 shows a variety of flat and curved structural frames fitted with modules.

It is important to assess mathematically the combined coverage of the assembled array, whether it was the total field-of-view (FoV) for multiple receivers or the total field-of-regard (FoR) for multiple transmitters. This information is essential to determine terminal aperture size, adjacent interference, coverage blind spots, and diversity gains, among others. Following is an analysis of some common contiguous-array configurations to serve as an example. Note that many other configurations, including non-contiguous, are also possible.

### *2.2.1 Flat Hexagonal Array*

#### Receivers-only Array

The FoV of a photo-diode (PD) or photo-transistor (PT) can be modeled asymptotically as a solid cone with its vertex at the center of the PD/PT and its circular base

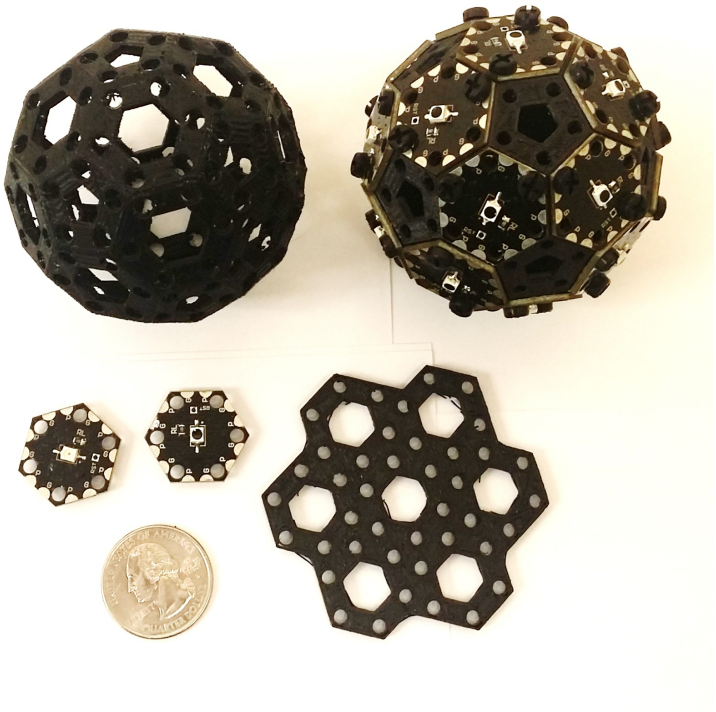

**Figure 2.3. Frames, arrays, and modules.**

***Upper left*: A spherical 3D-printed structural frame.**
***Upper right*: Same frame fitted with hexagonal modules.**
***Lower right*: A flat 3D-printed structural frame.**
***Lower left*: Hexagonal modules with a US quarter Dollar for size comparison.**

parallel to the module surface. The cone-opening angle is $2\theta_r$, where $\theta_r$ is the PD/PT angle of half sensitivity (i.e., where relative sensitivity drops to 50%). Figure 2.4 illustrates the combined FoV of multiple receivers in a flat hexagonal array. The hexagon side length is denoted $s$, while the short diagonal is denoted $d$, which is also the array optical resolution (i.e., the distance between any two modules center-to-center). Both quantities are related by the equation $d = s\sqrt{3}$.

Figure 2.4 shows the FoVs where communication is possible, as well as the *blind spots* (i.e., areas where no communication is possible). As we go further away from the array, individual FoVs begin to converge into a combined FoV. We identify two distinctive planes parallel to the array surface. The first is called the *Contact Plane*

and is defined as the plane at which the individual FoVs first touch each other. It is located at a distance of $d_{rr}$ from the array surface. The second plane is called the *Convergence Plane* and is defined as the plane at which individual FoVs are completely converged and there are no blind spots. It is located at a distance of $d_{Rr}$ from the array surface. At the contact plane, the receiver FoV cross-section is the hexagon's *in-circle*, and its radius is denoted $r_r = d/2$. At the convergence plane, the receiver FoV cross-section is the hexagon's *ex-circle*, and its radius is denoted $R_r = s = d/\sqrt{3}$. The subscript $r$ refers to a receiver.

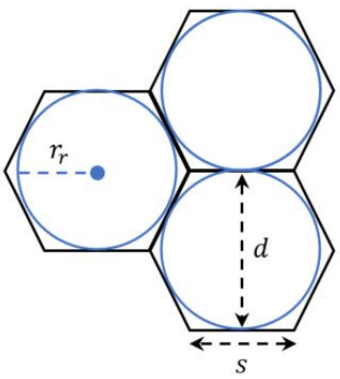


**(a)** Projection at the Contact Plane.

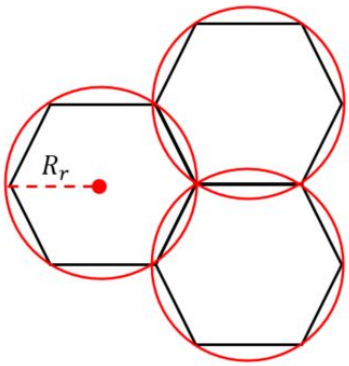


**(b)** Projection at the Convergence Plane.

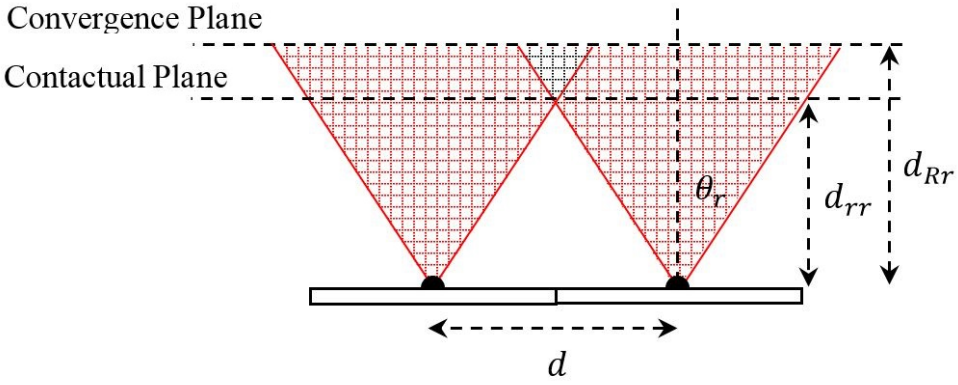


**(c)** Side View.

**Figure 2.4. Combined FoV of multiple receivers in a flat hexagonal array.**

For a continuous coverage, a transmitter must be located at or farther away from the convergence distance $d_{Rr}$, which is given by the following equation:

$$d_{Rr} = \frac{s}{\tan\theta_r} = \frac{d}{\sqrt{3}\tan\theta_r}. \tag{2.1}$$

We define the *Maximum Aperture Area* (MAA) as the sum of all FoV cross-sections (ex-circles) at convergence plane minus the overlapping areas. For the configuration shown in Figure 2.4, we subtract three overlapping lens-shaped areas from three ex-circle areas:

$$MAA = 3\pi {R_r}^2 - \Re\left(3\left[2{R_r}^2\cos^{-1}\left(\frac{d}{2R_r}\right) - \frac{d}{2}\sqrt{4{R_r}^2 - d^2}\right]\right), \tag{2.2}$$

where $\Re$ is the real part of a complex number. (Notably, it takes the value zero when there is no overlapping.) The general case of equation 2.2 is given by:

$$MAA = N\pi {R_r}^2 - \Re\left(M\left[2{R_r}^2\cos^{-1}\left(\frac{d}{2R_r}\right) - \frac{d}{2}\sqrt{4{R_r}^2 - d^2}\right]\right), \tag{2.3}$$

where $N$ is the number of receivers (modules) and $M$ is the number of overlapping lens-shaped areas, which depends on the array shape and topology.

The *Total Aperture Area* (TAA) at a given distance $h$ is defined as the sum of all FoV cross-sections minus the overlapping areas at a given plane above the array surface by $h$ distance-unit:

$$TAA(h) = N\pi r^2 - \Re\left(M\left[2r^2\cos^{-1}\left(\frac{d}{2r}\right) - \frac{d}{2}\sqrt{4r^2 - d^2}\right]\right), \tag{2.4}$$

where $r = h\tan(\theta_r)$ is the FoV cross-section radius at plane $h$. When $d \geq 2r$ (i.e., when there are no overlapping areas) the second term is zero. A useful measure is the ratio of TAA to MAA at a given plane $h$, which gives us the percentage of

useful areas with possible communication links, as compared to the non-useful areas or blind spots. This equation can be used to estimate blockage probability of a mobile transmitter moving at plane $h$.

$$TAA_{\%}(h) = 100 \cdot \frac{TAA(h)}{MAA}, \quad BlindSpots_{\%}(h) = 100 - TAA_{\%}(h). \tag{2.5}$$

Table 2.1 provides optical design examples for the 3-module hexagonal flat array shown in Figure 2.4. To illustrate how these numbers can be used to design for real scenarios, a simple example will be offered. Assuming a single transmitter is moving in a plane parallel to the array surface at an average speed of $v(m/sec)$, and assuming the transmitter has a way to steer and align its beam with the closest receiver module, we can calculate the outage and the blockage time probabilities that affect throughput and quality of service (QoS). To guarantee a continuous coverage,

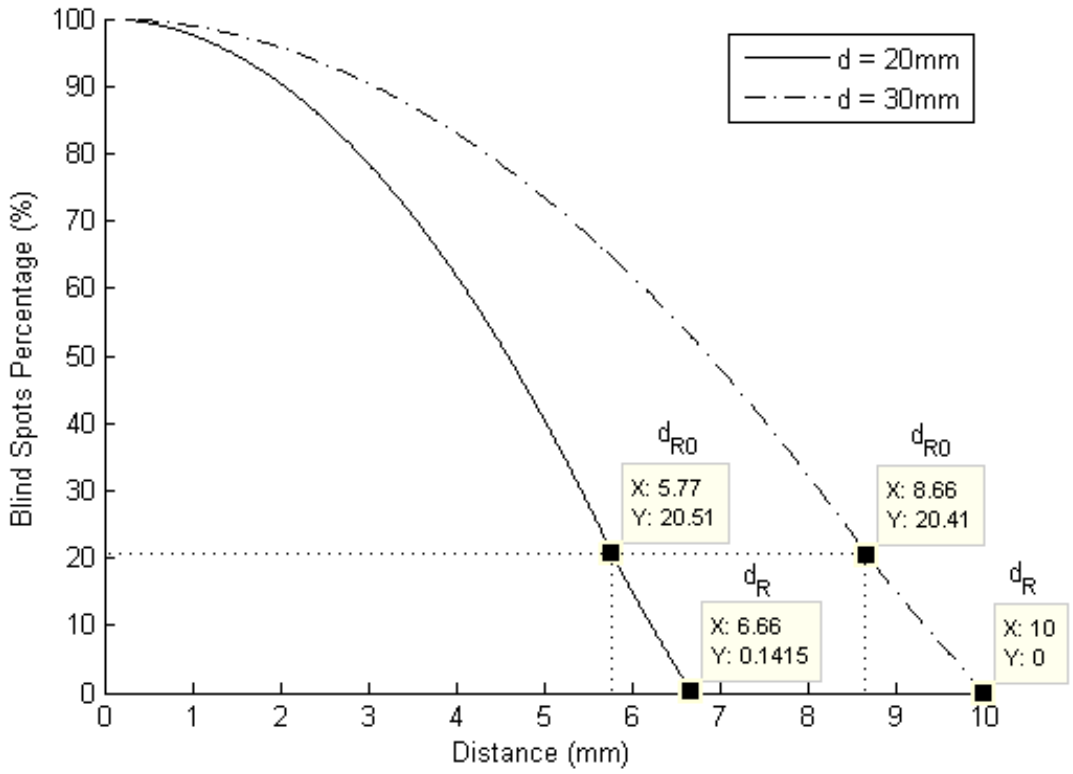


**Figure 2.5. Blind spots percentage in a three-module flat hexagonal array.**

the transmitter must move in a plane at or above the convergence distance $d_{Rr}$. When moving below the convergence plane, outage probability equals $BlindSpots_{\%}$ and is a function of plane height $h$, assuming random uniform transmitter movement. Figure 2.5 plots the percentage blind spots against distance in a flat hexagonal array using the two available MOWE optical resolutions (i.e., $20mm$ and $30mm$).

**Table 2.1. Various Optical Design Examples for the Hexagonal Flat Array Illustrated in Figure 2.4**

| **Optical Resolution** $d\ (mm)$ | **Angle of Half Sensitivity** $\theta_r(^\circ)$ | **Convergence Distance** $d_{Rr}\ (mm)$ | $MAA$ $(mm^2)$ | **Distance** $h\ (mm)$ | $TAA(h)$ $(mm^2)$ | $TAA_{\%}(h)$ |
|---|---|---|---|---|---|---|
| 20 | 60 | 6.67 | 1184 | $d_{Rr}/2$ | 314.2 | 26.53 |
| | | | | $d_{rr} = 5.77$ | 942.5 | 79.59 |
| 20 | 10 | 65.49 | 1184 | $d_{Rr}/2$ | 314.2 | 26.53 |
| | | | | $d_{rr} = 56.7$ | 942.5 | 79.59 |
| 30 | 60 | 10 | 2664 | $d_{Rr}/2$ | 706.9 | 26.53 |
| | | | | $d_{rr} = 8.66$ | 2120.6 | 79.59 |
| 30 | 10 | 98.2 | 2664 | $d_{Rr}/2$ | 706.9 | 26.53 |
| | | | | $d_{rr} = 85.1$ | 2120.6 | 79.59 |
| 60 | 60 | 20 | 10658 | $d_{Rr}/2$ | 2827.4 | 26.53 |
| | | | | $d_{rr} = 17.3$ | 8482.3 | 79.59 |
| 60 | 10 | 196.5 | 10658 | $d_{Rr}/2$ | 2827.4 | 26.53 |
| | | | | $d_{rr} = 170.1$ | 8482.3 | 79.59 |

Maximum blockage time $t_{off,max}$ occurs in the rare scenario of traversing over all blind spots. Time can be estimated using the average transmitter speed ($v$), maximum array aperture area (MAA), and array percentage blind spots. Note that since multiplication of the later two quantities yields an area rather than a distance−which is what we need to calculate time−a factor of $\sqrt{2}$ was used to convert to distance. This is an estimate assuming the shortest path to cross a squared unit area using a straight line by following its diagonal. Figure 2.6 plots estimated maximum blockage times at various planes and speeds.

$$t_{off,max}(h) = \frac{\sqrt{2} \cdot \frac{BlindSpots_{\%}(h)}{100} \cdot MAA}{v} = \frac{\sqrt{2}\Big(MAA - TAA(h)\Big)}{v}. \tag{2.6}$$

**Transmitters-only Array**

There are multiple methods to reduce outage probability and minimize blockage time for the flat receiver array analyzed in the previous section, including:

- Using a higher-optical resolution receiver array.
- Increasing transmitter speed.
- Increasing transmitter beam divergence to cover more than one receiving module.
- Increasing transmitter beam footprint using a transmitter array.

Since increasing beam divergence reduces power and, thus, range, the technique is not recommended. One can increase beam footprint and maintain power levels at the same time by combining multiple transmitter modules in a configuration similar to the one depicted in Figure. 2.4. However, a transmitter FoR, unlike receiver FoV, does not extend to infinity. If module spacing (i.e., the optical resolution) is not

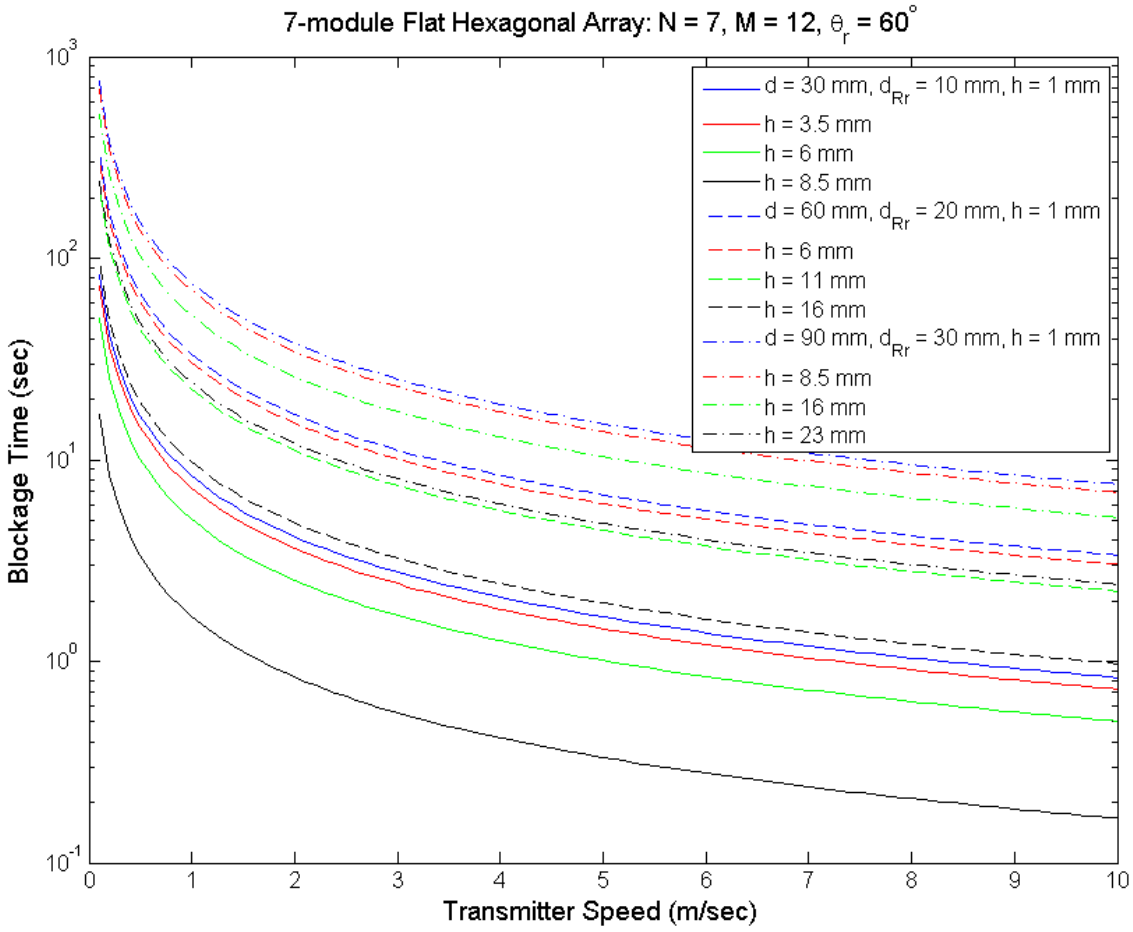


**Figure 2.6. Maximum blockage time for a 7-module flat hexagonal array at various transmitter planes and velocities.**

chosen carefully, gaps or blind spots will appear. Given that the goal is to increase beam footprint by combining individual FoRs, then gaps are undesirable and must be eliminated or minimized. Otherwise, if the goal is to utilize each transmitter module separately, then gaps are necessary to eliminate or reduce co-interference from neighboring modules.

For LED-based transmitters, the optical intensity profile follows the Lambartian law, which can be approximated asymptotically by solid cones, as shown in [31]. Since the analysis is very similar to the one presented in the previous section, this information will not be repeated in this section. The most important parameter is

the convergence distance $d_{Rt}$, where subscript $t$ refers to a transmitter and $\theta_t$ is the beam full-width-at-half-maximum (FWHM) divergence angle:

$$d_{Rt} = \frac{s}{\tan\theta_t} = \frac{d}{\sqrt{3}\tan\theta_t}. \tag{2.7}$$

### *2.2.2 Truncated Icosahedron-based Spherical Array*

Based on the analysis detailed in Section 2.2.1, we can port the same concepts to a spherical array topology. Using 20 hexagons and 12 pentagons, we can build a spherical structure called a *truncated icosahedron*—commonly known as a soccer ball. Although a specific hexagon/pentagon size can create only a single-size truncated icosahedron-based spherical array, there are two other methods to build larger spherical structures based on modular elements: (a) using equilateral triangles to build larger hexagons/pentagons and, hence, larger truncated icosahedrons, or (b) directly building geodesic spheres (a platonic solid) using two or more irregular triangles [50].

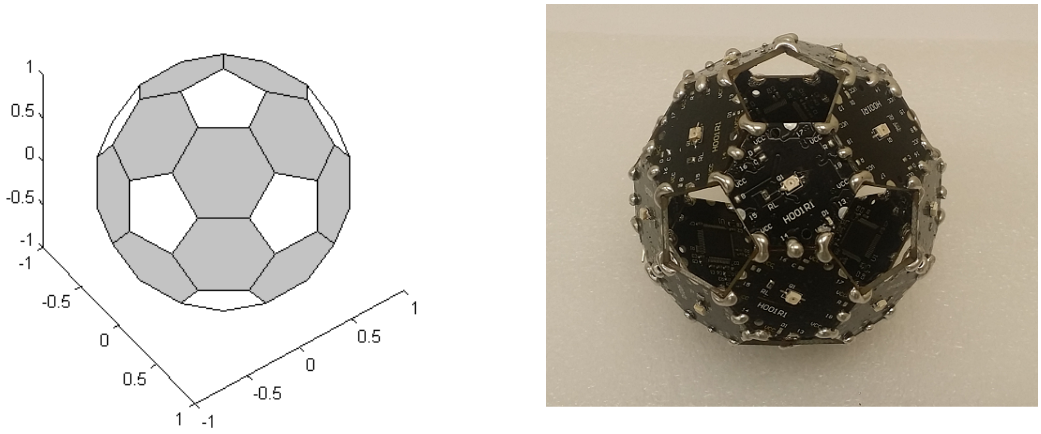


**(a)** **(b)**

**Figure 2.7. A spherical array based on a truncated icosahedron.**

**(a) A 3D illustration of a truncated icosahedron with hexagon faces in gray and pentagon faces in white. (b) Actual spherical array based on a truncated icosahedron with hexagonal receivers.**

Figure 2.7 shows a 3D illustration and actual construction of a truncated icosahedron-based spherical array with hexagonal receivers. Using hexagons allows continuous physical and electrical connection between all modules without the need for cables or supporting structure. The $20mm$ modules create a sphere with an approximate diameter of $56mm$, while the $30mm$ modules create a sphere with an approximate diameter of $84mm$. The angles between any two adjacent hexagons is 138.19°; between any two adjacent hexagon and pentagon is 142.62°; and between the nearest pentagons is 116.57°. These figures can be used to calculate convergence distances for receivers and transmitters ($d_{Rr}$, $d_{Rt}$) in various configurations. Here, convergence planes are parallel to the surface of each module (i.e., at their intersections they form an enlarged copy of the truncated icosahedron).

Figure 2.8 illustrates the combined FoV of two adjacent non-parallel modules. The tilt angle between the two modules is called $\alpha$; and in the case of a truncated icosahedron it may take any one of the following values: 138.19°, 142.62°, or 116.57°.

Using some trigonometric derivations, the contactual distance $d_{rr}$ can be calculated as:

$$d_{rr} = -\frac{d \cdot \sin(\frac{\alpha}{2}) \cdot \cos(\theta_r)}{2 \cdot \cos(\theta_r + \frac{\alpha}{2})}. \tag{2.8}$$

The beam cross-section radius at the contact plane $r_r$ can then be calculated from:

$$r_r = d_{rr} \cdot \tan(\theta_r), \tag{2.9}$$

which shares the following relationship with beam cross-section radius at the convergence plane $R_r$ (in-circle and ex-circle of a hexagon):

$$\frac{r_r}{R_r} = \frac{d/2}{d/\sqrt{3}} \rightarrow R_r = \frac{2}{\sqrt{3}} r_r. \tag{2.10}$$

Finally, convergence distance $d_{Rr}$ can be calculated from the following equation. Table 2.2 lists convergence distances for various configurations in a truncated icosahedron-based spherical array.

$$d_{Rr} = \frac{R_r}{\tan(\theta_r)}. \tag{2.11}$$

In the case of non-adjacent pentagons, Equation 2.8 is modified as follows:

$$d_{rr} = -\frac{1.413 \cdot d \cdot \cos(\theta_r)}{2 \cdot \cos(\theta_r + \frac{\alpha}{2})}. \tag{2.12}$$

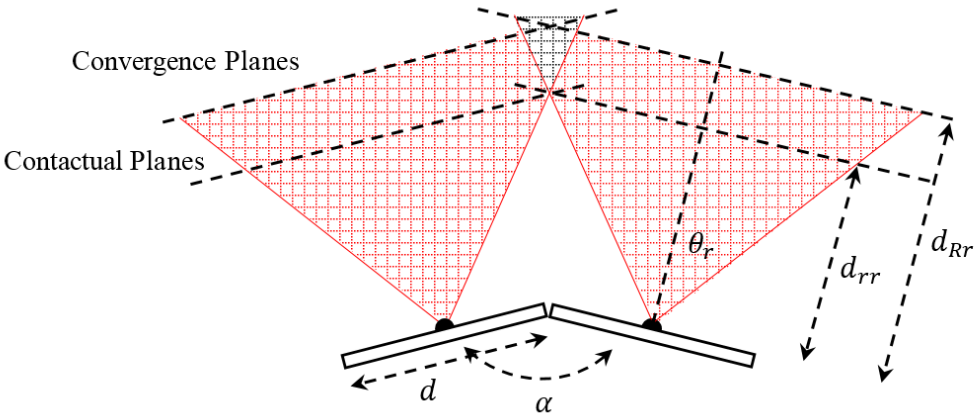


**Figure 2.8. Illustration of a combined FoV of two adjacent non-parallel modules.**

**Table 2.2. Convergence Distances for Various Configurations in a Truncated Icosahedron-based Spherical Array**

| **Configuration** | **Optical Resolution** $d$ $(mm)$ | **Convergence Distance** $(mm)$ |
|---|---|---|
| Hexagonal receivers only ($\theta_r = 60°$, $\alpha = 138.19°$) | 20 | $d_{Rr} = 8.55$ |
| | 30 | $d_{Rr} = 12.83$ |
| Hexagonal transmitters only ($\theta_r = 10°$, $\alpha = 138.19°$) | 20 | No convergence |
| | 30 | No convergence |
| Pentagonal receivers only (Non-adjacent, $\theta_r = 60°$, $\alpha = 116.57°$) | 20 | $d_{Rr} = 17.22$ |
| | 30 | $d_{Rr} = 25.82$ |
| Pentagonal transmitters only (Non-adjacent, $\theta_r = 10°$, $\alpha = 116.57°$) | 20 | No convergence |
| | 30 | No convergence |

## 2.3. The Optical Terminal

In most scenarios, the array cannot solely communicate with the outside world. Instead, a central controller is needed to configure the array, send transmitted data, and forward received data to the user via a wired (e.g., Ethernet/fiber optics) or a wireless (e.g., cellular/WiFi) interface. Figure 2.9 illustrates three possible configurations for a terminal: (a) A single array connected to a single controller; (b) More than one array connected to the same controller; or (c) A single array connected to multiple controllers. A fourth option without a central controller is also viable when running distributed control and sensing applications.

The assembled terminal can either be utilized as a fixed node or be carried aboard a mobile unmanned ground vehicle (UGV) or unmanned aerial vehicle (UAV) [9,37]. Battery and data storage capabilities might be added to the system, depending on operating scenarios.

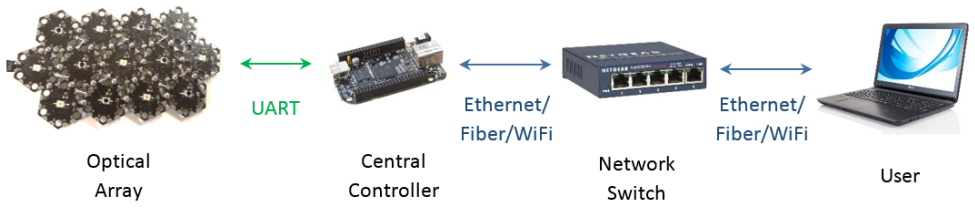


(a)

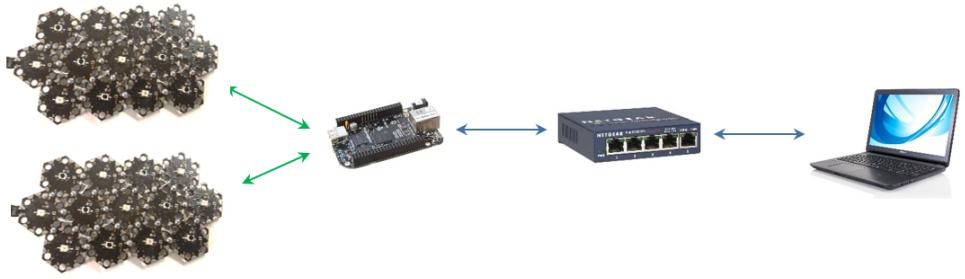

(b)

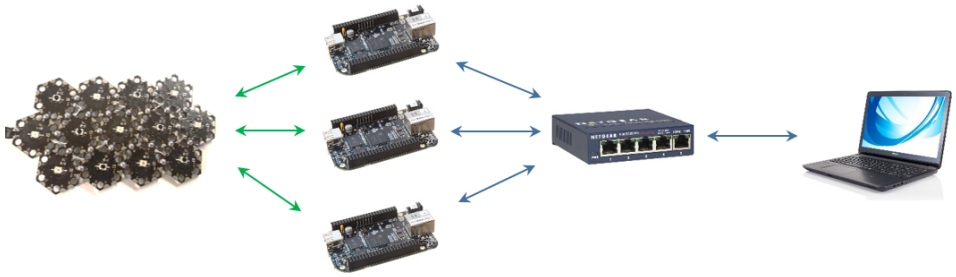

(c)

**Figure 2.9. Possible configurations for an optical terminal.**

## 2.4. Applications

The following list gathers some research topics and applications that can be prototyped using MOWE. Though it is not meant to be comprehensive by any means, it gives an idea of the breadth of applications for this technology:

- Short- and medium-range fixed FSO links.
- Short- and medium-range mobile FSO (air-to-air, air-to-ground, and ground-

to-ground links).

- Infrared and visible light communications (ILC/VLC).
- Indoor optical wireless communications.
- Broadband optical communications and LiFi.
- Last-mile FSO technology.
- User tracking and 3D localization.
- Multi-input-multi-output (MIMO) optical antennas.
- Testbeds for spatial and wavelength diversity.
- Testbeds for optical wireless networks.
- Optical relays and switches.
- Background noise measurement and estimation.
- Optical channel modeling and estimation.
- Optical radar and remote optical sensing.
- Distributed sensing, estimation and control.
- Distributed computing systems.
- Motion detection and obstacle avoidance for mobile platforms.
- Optical navigation and stabilization for UAVs.
- Optical flow sensors.
- Software-defined optics.
- Cognitive optics.
- Educational platforms and lab experiments for the topics listed above.

# Chapter 3: MOWE Hardware and Firmware

MOWE hardware has been through two iterations thus far. First generation proof-of-concept prototype consisted of only $20mm$ modules ($20mm$-optical resolution) with a bus architecture and 8-bit microcontrollers (MCUs). Second generation MOWE features six module designs: two small $20mm$-hexagons (transmitter and receiver) for dense flat arrays plus two larger hexagons ($30mm$), and two pentagons ($30mm$) for flat and spherical arrays. Second generation improved on the first one in many aspects, including a peer-to-peer architecture, faster streaming speeds, and 32-bit MCUs. Module specifications are listed in Table 3.1.

## 3.1. Optical Specifications

Available modules feature an $850nm$ LED with $10°$ FWHM divergence angle for transmitters and either an $850nm$ or $940nm$ photo-transistor (PT) with $60°$ angle of half sensitivity for receivers. The $940nm$ PT comes with a daylight filter and can be used for infrared invisible communication. Future modules might also include laser diodes (VCSELs) as transmitters to offer higher power and longer range.

Communication range basically depends on receiver sensitivity, which is related to load resistor ($R_L$) value. Default value was chosen to enable indoor communication with 2-3$m$ range. It can be adjusted, however, according to application requirements. Maximum range $R_{max}$ can be estimated based on four key parameters, namely the *received light intensity*, *PT's sensitivity*, *atmospheric attenuation*, and *geometric attenuation* [31].

Receiver optical sensitivity ($S$), using a 620-$\Omega$ load resistor, is about $5\mu W/cm^2$. The PT surface area is $\pi(1.2)^2 = 4.53mm^2$, which results in $0.226\mu W$ minimum

received power (i.e., $S = -36.46 dBm$). Assuming $P$ is transmitter optical power in $dBm$, the following inequality must be satisfied for PT to detect any optical signal [31, 51]:

$$P - S > -(A_L + A_G), \tag{3.1}$$

where $A_L$ is the atmospheric attenuation given by Beer's Law as:

$$A_L = 10 \log(e^{-\sigma R/1000}), \tag{3.2}$$

and $A_G$ is the geometric attenuation:

$$A_G = 10 \log \left( \frac{\zeta}{\gamma + 100 R \theta_t} \right)^2. \tag{3.3}$$

In equation 3.3, $\zeta$ and $\gamma$ are receiver and transmitter radii in $cm$, respectively; $R$

**Table 3.1. MOWE Hardware Specifications**

| | |
|---|---|
| **Architecture** | Peer-to-peer |
| **Streaming speed** | up to $1 Mbps$ |
| **MCU** | 32-bit ARM Cortex-M0, $48 MHz$ with DMAs, $256 Kb$ Flash memory |
| **Module thickness** | $3.2 mm$ |
| **Optical resolution (Module center to center)** | $20 mm$, $30 mm$ |
| **Module weight** | $< 2g$ |
| **Module cost** | Approx. \$6 |
| **Module power consumption (without sleep mode)** | 40-66$mW$ |
| **LED wavelength** | $850 nm$ |
| **LED FWHM divergence angle** | $\pm 10^o$ |
| **LED radiant intensity** | $100 mW/sr$ |
| **PT wavelength** | $850 nm$, $940 nm$ |
| **PT angle of half sensitivity** | $\pm 60^o$ |
| **PT optical sensitivity** | $\approx 5 \mu W/cm^2$ for $R_L = 620\ \Omega$ |

is the communication range in $m$; and $\theta_t$ is the FWHM divergence angle in *radians*. In equation 3.2, $\sigma$ is the attenuation coefficient, mainly based on Mie scattering:

$$\sigma = \frac{3.91}{V} \cdot \left(\frac{\lambda}{550}\right)^{-q}, \tag{3.4}$$

where $\lambda$ is the wavelength in $nm$; $V$ is the atmospheric visibility in $km$; and $q$ is the size distribution of the scattering particles whose value is dependent on the visibility $V$.

Substituting both equations 3.2 and 3.3 in inequality 3.1 yields:

$$-(P + 36.46) < 10\log(e^{-\sigma R}) + 10\log\left(\frac{\zeta}{\gamma + 100R\theta_t}\right)^2. \tag{3.5}$$

Solving for $R$ yields the range where communication is possible. Maximizing 3.5 results in the maximum range $R_{max}$ for the given visibility, wavelength, divergence, load resistor, and receiver and transmitter radii. Table 3.2 lists maximum range simulations for MOWE with various sensitivity thresholds using the following parameters: $\lambda = 850nm$, $V = 6km$ (normal weather, $q = 1.3$), $P = 32mW = 15.05dBm$ (typical $10mA$ LED), and $\theta_t = 10^\circ = 0.1745rad$.

Shorter distances have been recorded in experiments due to noise-limiting effects of simplified receiver design. Since the purpose of second generation MOWE was to develop and test the firmware and all system components rather than optimizing the receiver/transmitter hardware design, the system achieved shorter range in lab setting. We conducted two sets of experiments to measure optical characteristics

**Table 3.2. MOWE Maximum Range Simulation**

| **Transmitter** | **Receiver** | **Load Resistor** $R_L$ $(\Omega)$ | **Receiver Sensitivity** $S$ $(dBm)$ | **Maximum Range** $R_{max}$ $(m)$ |
|---|---|---|---|---|
| Single module | Single module | 620 | -36.46 | 2.59 |
| ($\zeta = 0.09cm$) | ($\gamma = 0.12cm$) | 1200 | -38.67 | 3.34 |
| | | 2400 | -41.68 | 4.72 |
| | | 3900 | -44.41 | 6.45 |

of individual MOWE receivers. One set of experiments characterized the receiver distance-power relationship by laterally translating a laser beam across the FoV at multiple separation distances (a sample data shown in Figure 3.1 at 19.05$cm$ separation). The other set of experiments measured receiver angular FoV by shining a laser beam at the receiver from multiple angles, and then recording relative measured intensity (a sample data shown in Figure 3.2). The measured FoV reached ±85°.

### *3.1.1 Optical Sensitivity and Dynamic Range*

Optical sensitivity and dynamic range are properties of individual detector modules and do not change when assembling modules in an array. They depend, however, on the module hardware design, including ADC resolution, supply voltage, and load resistors, among others. In anticipation of a simple and inexpensive design, detector modules simply utilize a photo-transistor (PT) and measure voltage across a load resistor. Next, approximate calculations are provided for these optical properties.

Optical sensitivity is defined herein as the minimum amount of optical irradi-

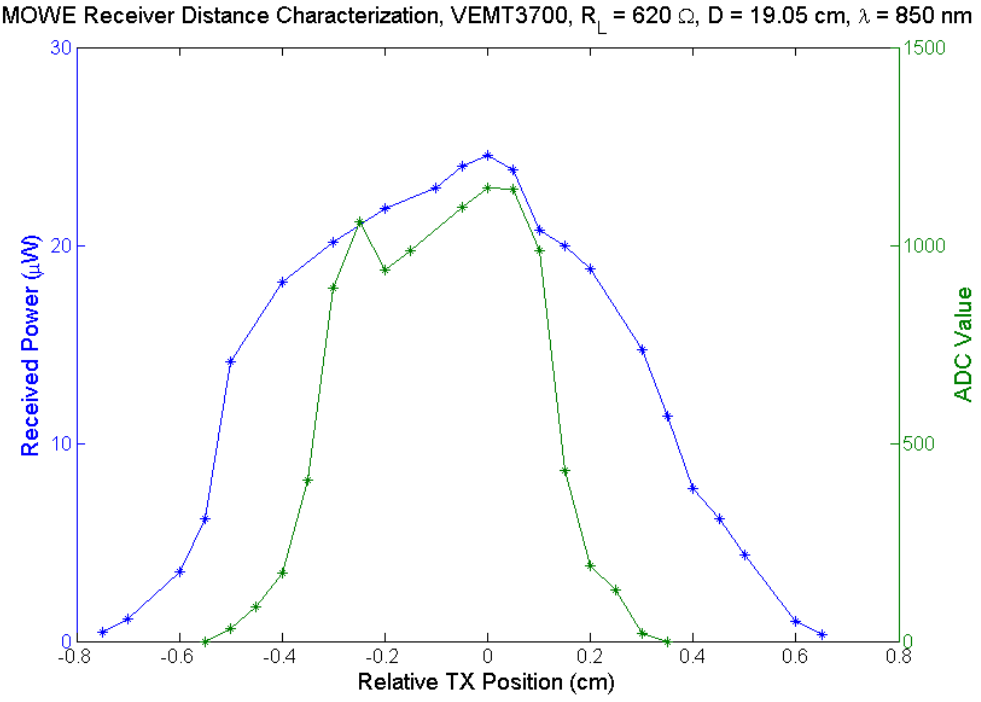


**Figure 3.1. MOWE receiver distance-power characterization.**

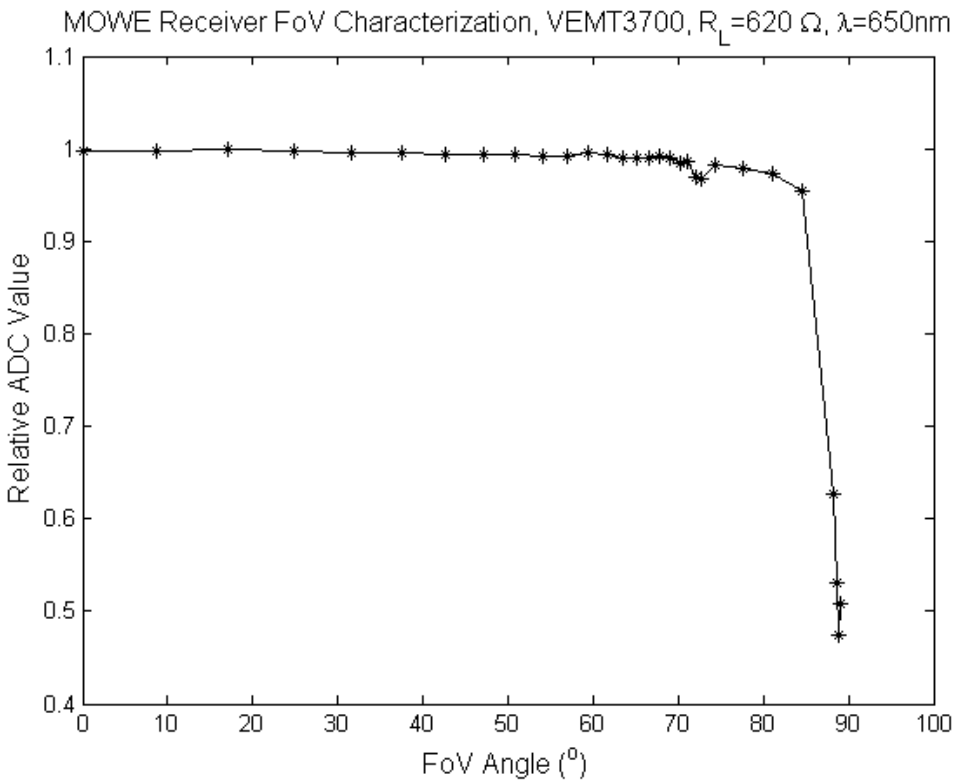


**Figure 3.2. MOWE receiver individual FoV characterization (Only half the FoV is shown).**

ance reliably detectable by the module. For a 12-bit ADC and 3.3V supply voltage, minimum detectable PT collector light current is given by the following (assuming a single-bit measurement is reliable):

$$I_{c_{min}} = \frac{3.3V}{2^{12} \cdot R_L} = \frac{0.80566mV}{R_L}, \tag{3.6}$$

where $R_L$ is the PT load resistor in $\Omega$. Using $I_{c_{min}}$ and the PT *Collector Light Current vs. Irradiance* curve in the datasheet, one can determine the minimum detectable optical irradiance or detector optical sensitivity in $mW/cm^2$. Using PT surface area of $\pi(1.2)^2 = 4.53mm^2$, the minimum detected optical power or receiver sensitivity in $dBm$:

$$S = 10 \cdot \log\left(f\left(\frac{0.80566mV}{R_L}\right) \cdot 0.0453cm^2\right), \tag{3.7}$$

where $f$ is the mapping function between optical irradiance (in $mW/cm^2$) and col-

lector light current (in mA). When $R_L = 620\Omega$, then $S = -36.45dBm$.

The maximum measurable PT collector light current is defined by the maximum measurable voltage across the load resistor. Given a 3.3V supply voltage and an average PT collector-emitter saturation voltage of 0.3V, maximum measurable PT collector light current is approximately:

$$I_{c_{max}} \approx \frac{3V}{R_L}. \tag{3.8}$$

Maximum measurable optical irradiance was determined by returning to datasheet curves. Detector optical dynamic range can then be estimated according to PT load resistor. Note that all previous calculation must be adjusted according to the correct wavelength and PT spectral sensitivity curves. Based on PT collector light current

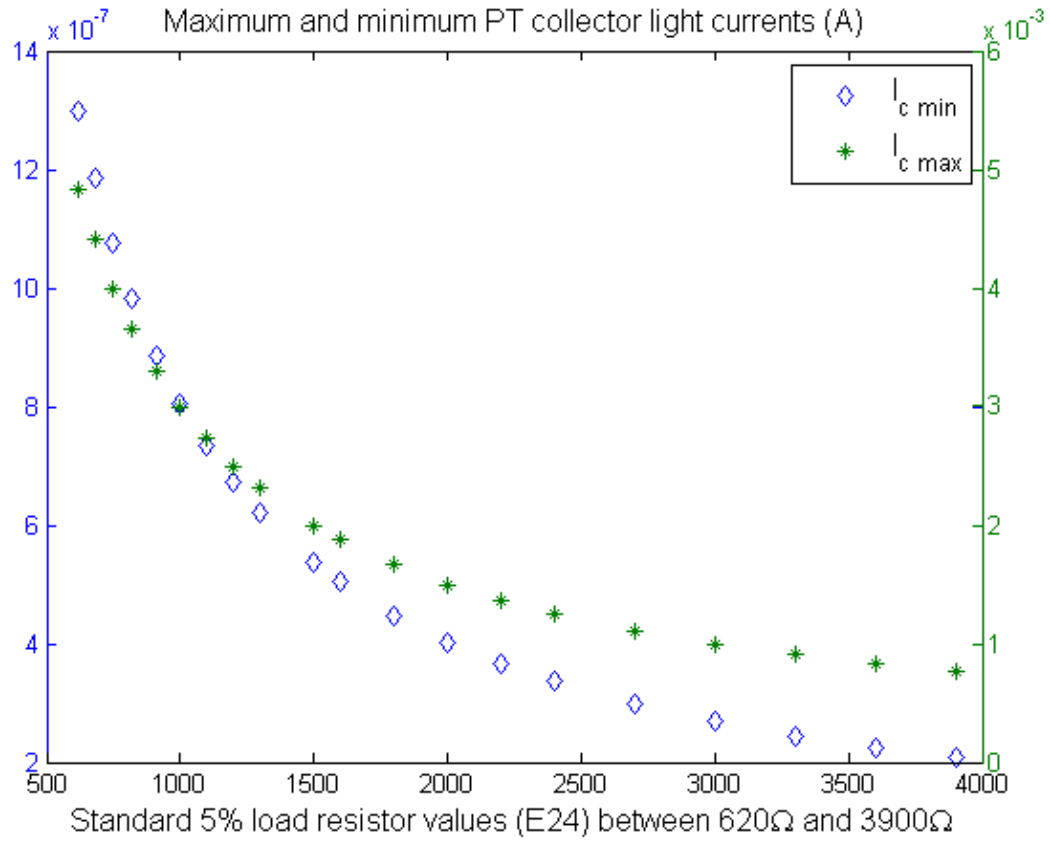


**Figure 3.3. MOWE receiver maximum and minimum PT collector light currents vs. PT load resistor value.**

range provided in the datasheet and using standard 5% resistor values (E24), a load resistor between 620Ω and 3900Ω is suitable. Figure 3.3 plots minimum and maximum collector light currents against these resistors. Larger resistor values yield higher sensitivity (lower $I_{c_{min}}$), thus longer detection range, while smaller resistor values yield lower sensitivity and more immunity to background noise.

## 3.2. Electrical Specifications

Every module is fitted with a 32-bit ARM Cortex-M0 MCU from STMicroelectronics on its backside. Debugging and programming ports are provided on the topside along with a small LED indicator for easy module identification. Table 3.1 lists some of the modules' electrical specifications. Power consumption measurements represent module active state and vary depending on MCU clock frequency and whether transmitter LEDs are on or off. Configuring the module to sleep or enter low power modes greatly reduces average and total power consumption. The $1 Mbps$ streaming speed is achieved via direct memory access (DMA) and depends on the configured MCU clock frequency and USART baudrate. Experiments showed maximum speed of $3 Mbps$ for raw inter-array streams, which might slow down a bit in practical scenarios. Future generations will most likely boost higher communication speeds and use hardware accelerators.

## 3.3. Firmware Architecture

MOWE firmware is written in embedded C (C99) language using Keil uVision 5 IDE. There are two versions. The first is *Array Operating System* (AOS), which is not based on a real-time operating system (RTOS). AOS firmware is more comprehensive, having more command line parser (CLP) commands and inter-array communication routines. However, AOS is poor in multitasking and multithreading. The second version of MOWE firmware is called *AOS+FreeRTOS* and is based on the widely known open-source real-time operating system FreeRTOS [52]. This firmware also makes use of a modified version of the command line interface (CLI) module provided by FreeRTOS to facilitate user interaction (replacing the old CLP).

### *3.3.1 AOS Firmware Overview*

AOS firmware is separated into four layers, as detailed in Figure 3.4:

- **Hardware Abstraction Layer (HAL) Drivers**: The HAL library is provided by MCU manufacturers (STMicroelectronics [ST] and ARM) and provides many APIs (application program interfaces) and low level access to the Cortex-M0 core and STM32F0xx MCU peripherals.

- **Array Operating System (AOS)**: AOS is a custom-designed operating system that handles user interactions, inter-array communication, and array housekeeping functionality (e.g., cross-array routing, module labeling and identification, broadcast commands, firmware update, and others.) AOS has four modules:

  - **Peripheral Drivers (PDs)**: PD files were initially generated by the STM32-CubeMX utility and later modified to provide a higher abstraction layer for MCU peripherals.

  - **Module Drivers (MDs)**: MDs provide routines for various module functionality (e.g., front-end routines, module parameters, EEPROM emulation, and others).

- **Inter-array Communication (IAC)**: IAC provides routines to handle all inter-array (intra-module) communication needs, such as single-casting (routing), multicasting, and broadcasting.
- **Command Line Parser (CLP)**: The CLP processes user input from a serial terminal, and then executes various commands. Commands are used to adjust module and array parameters, test the module, stream in/out at specific rates, stream using DMAs, update firmware, and others. Developers can enable or disable specific commands in their firmware compilation.

- **Local Applications**: This layer contains all application-level routines running locally on the module, including the *main.c* file and any user applications.
- **Distributed Applications**: This module is intended for user applications that run in a distributed manner (i.e., on multiple modules simultaneously).

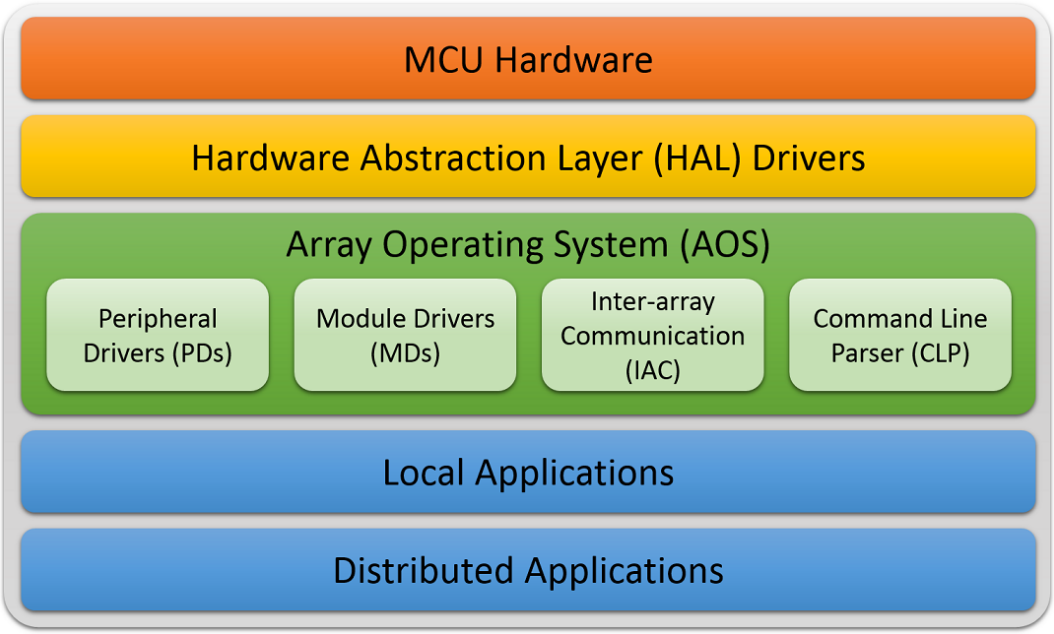


**Figure 3.4. MOWE firmware overview.**

A *regular* user can interact with the array via the *command line parser* (CLP) utility within the AOS. The CLP can be accessed via any port in any module and features various intuitive control commands in a plain English language. Some commands are used to setup the array, ping the modules, rename them, and group them; other commands read samples from receiver modules and stream data in/out of the modules at various speeds. More advanced commands are also available to update modules firmware on the fly, setup inter-array DMA streams, link two modules, and send a predefined signal out a transmitter module, among others. These intuitive commands make the MOWE system easily accessible by any student/researcher regardless if he or she has hardware or Embedded Systems development expertise. *Experienced* users, on the other hand, can further leverage the system by writing their own firmware in C language or modifying the AOS and other available firmware implementations to suit their specific application.

### *3.3.2 AOS+FreeRTOS Firmware Overview*

The AOS+FreeRTOS firmware defines eight threads or tasks (seven in case of pentagons):

- **The DefaultTask** can be used for signaling via the indicator LED.
- **Port tasks** (P1Task, P2Task, P3Task, P4Task, P5Task and P6Task) can be used to handle communication through module ports.
- **The FrontEndTask** can be used to run user programs and is given a higher priority.

### *3.3.3 Direct Memory Access Streams*

The firmware supports two modes of inter-module communication, namely routing and streaming. *Routing* protocol transfers messages between modules in single-cast, multi-cast, or broadcast fashion. The process utilizes short packets and keeps the port

open for others. The speed, however, is slow (i.e., in the range of *kbps*), and the connection is not reliable. In *streaming* mode, dedicated DMA channels are configured, which supports reliable connections at speeds up to 1-2*Mbps*. Nevertheless, once configured as DMA streams, ports will be blocked and cannot be accessed for messaging. DMA streams are very reliable, although difficult to control. They can be configured for single-input-single-output (SISO) and single-input-multiple-output (SIMO) fashion. Figure 3.5 depicts an example of array-level DMA streams. Examples of such streams include:

- **Port-to-front-end and front-end-to-port**: A single stream connecting the front-end (LED or PT) with a serial port.
- **Memory-to-front-end and front-end-to-memory**: A single stream connecting the front-end (LED or PT) with a memory location.
- **Port-to-memory**: Multiple streams available. Each stream can transfer a specific amount of bytes from a serial port to a specific memory address.
- **Port-to-port**: Multiple streams available. Each stream can transfer a specific amount of bytes from one serial port to another. Multiple streams can be combined to transfer data from a single port to multiple other ports at the same time.

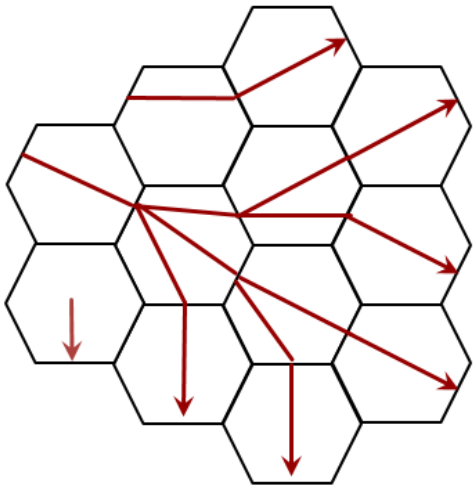

**Figure 3.5. Example of array-level DMA streams.**

## 3.4. Software Development Tools

MOWE development framework features free software tools that aid in designing and debugging MOWE arrays, especially for large, complex designs.

### *3.4.1 MOWE-Tandy Simulator*

Although MOWE arrays are inexpensive and easy to assemble, massive MIMO arrays composed of hundreds or thousands of modules are difficult to build and debug. Our research group collaborated with the Tandy Supercomputing Center (TSC) [53] to create a simulator for MOWE arrays. The Tandy Simulator is a C/C++ multi-agent simulator based on Message Passing Interface (MPI) protocol and allows users to develop and test high-level MOWE applications or low-level AOS algorithms that can scale up to thousands of modules. Each module is simulated as a separate process that could run independently on a separate core or share resources with other processes.

### *3.4.2 MOWE Automatic Topology Generator*

The Automatic Topology Generator (ATG) is a MATLAB tool used to graphically design a MOWE array and automatically generate all required configuration and topology files. This will save developers a great deal of tedious, error-prone work. The tool is particularly useful when dealing with large arrays.

The tool generates two outputs: a MATLAB figure that graphically demonstrates the array where transmitter modules are shown in red and receiver modules in green, along with a topology header file. The header file "topology.h" is used in the firmware to setup module part number, port swap configuration, and array topology for routing and inter-array communication routines. A similar file can be generated, as well, and used to setup the MOWE-Tandy Simulator. Figure 3.6 illustrates a design for a flat 7-module array.

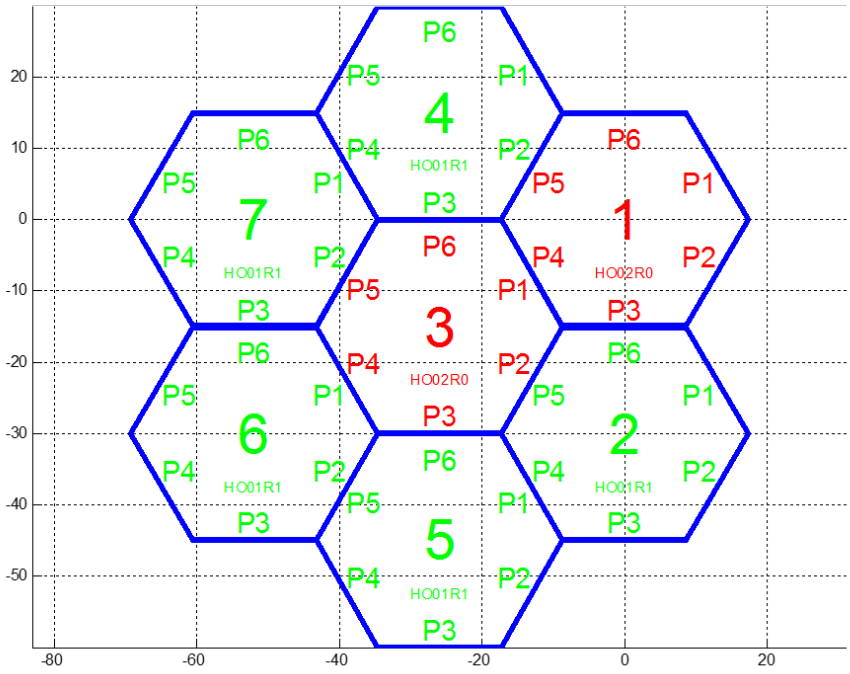


**Figure 3.6. An example using the automatic topology generator.**

# Chapter 4: Case Study: Wide-area Optical Detector Arrays

MOWE can be used to construct large and complex optical detector arrays that provide wide-area−even omnidirectional-field-of-view (FoV). Programmable optical modules synchronously sample the environment, and then route measurements to the user via a dedicated electrical backbone. The arrays are inexpensive, easy to construct, and can be made with homogeneous/inhomogeneous optical properties. Applications include remote sensing, motion detection, optical navigation, and medical imaging, among others.

## 4.1. Introduction

Since the early days of digital imaging, it has been obvious that a single imaging element (i.e., pixel) is not ample for capturing meaningful information. A photosensitive device equivalent to traditional sensitive photographic plates is needed. Multiple imaging elements must be assembled side-by-side to create such a device. Early in 1960s, photo-lithography enabled monolithic integration of silicon imaging focal plane arrays (FPAs) for the visible and infrared spectrum. FPA refers to the assembly of individual detector picture elements (i.e., pixels) located at the focal plane of an imaging system [54]. FPAs are primarily two-dimensional, yet occasionally one-dimensional (i.e., linear), structures that are always flat. Monolithic FPAs have achieved extremely high integration, yielding resolution as high as 2 gigapixels for charge coupled devices (CCDs) and 147 megapixels for infrared arrays targeted at astronomy applications [14].

Just like other innovations, the concept of a pixelated imaging system emerged from observing nature [17]. Camera-type eyes feature a single adaptive lens focusing

light on multiple receptors, much like a CMOS/CCD-based imaging device. Compound eyes have arrays of lenses and other optical structures focusing light on receptors. The latter type of eye has been bio-mimicked using microlens arrays [17]. Both types of eyes feature thousands of light receptors that have been outperformed by man-made FPAs, as mentioned above. However, natural eyes are defined by a curved structure that is exceptionally difficult to implement. Native eyes have curved structures for substantially increasing the FoV. Both lens and receptor arrays are curved and sometimes have nearly hemispherical shapes. Conventional electronic processing techniques, including most types of lithography, are strictly planar. Various attempts have been made to combat this problem by fabricating photodetector arrays with flexible interconnects (i.e., making a curved artificial retina) [55,56], or by combining deformable arrays of thin photodetectors with elastometric microlens arrays made of special polymers [18].

Although these techniques are expected to yield substantial advancements in optical imaging, detection, and tracking technology, they remain complicated, expensive, and inaccessible to most researchers and engineers. They are also not suitable for applications that require large spatial coverage or situations when resolution is not necessarily important. Modularity and programmablity of MOWE architecture allow large arrays of optical detectors to be assembled in flat, spherical, or even uncommon shapes. Researchers and engineers can rapidly and inexpensively prototype large-FoV optical detector arrays by merely using standard and mainstream hardware prototyping tools. Although MOWE-based arrays cannot compete with custom-built solutions in terms of optical resolution, speed, or efficiency, they offer researchers an accessible entry to this field. Their programmability supports many novel applications that require processing capabilities at the optical front end.

An optical detector array is made of multiple optical receivers (e.g., photo-diodes, photo-transistors, and others) and has two distinct features: *synchronization* and *data reporting*. Synchronization refers to the fact that all optical points (i.e., modules) must sample the FoV at the exact same moment. This is important since spatial correlations between samples cannot be deducted unless measurements are synced in

time. Data reporting means the array should report all measurements before the next sampling epoch arrives. Although measurements can be processed locally without the need to report all data, we prefer the scheme wherein all measurements are reported and processing is performed online or offline on an external platform. There are two benefits to this method: first, the ability to run complex computations on the data (e.g., FFT) and second, the ability to analyze the entire array and check for correlations between faraway modules. Preferably, the user will read data from a single port rather than accumulating it from multiple ports. Single-port reporting, however, complicates the array design.

## 4.2. Design Methodology

When designing a MOWE-based detector array, two important aspects must be examined: 1) The array combined FoV, informing about FoV gaps and defining array optical properties (See Section 2.2); and 2) the array electrical backbone defining the maximum rate at which data can be streamed out with zero bit error rate (BER).

### *4.2.1 Challenges and Solutions*

Due to strict modularity and symmetry requirements, MOWE modules do not feature a hard synchronization signal line. Figure 2.2-E shows edge-connectors. The signaling connector pair on top and bottom provides full-duplex serial communication (i.e., RXD and TXD) and is positioned exactly in the middle of each module side. In this way, modules can be assembled irrespective of orientation given that they face either up or down. Adding a hard synchronization signal line would complicate the design and implementation of the module or result in either an asymmetric design or half-duplex communication. Bus architecture was rejected, as mentioned earlier, to provide more flexibility in array design without the capacity/topology limitations of an electrical bus. The result, however, is that modules lack hardware-level synchronization, which is crucial for detector arrays.

These issues were compromised by tailgating DMA streams to mimic a hard synchronization signal line with a known, fixed delay. DMA streams are constructed between module ports so that an incoming synchronization signal is forwarded immediately to the next module(s) via another port(s). DMA transfers are strictly performed in hardware and are independent of the running algorithm or whether the CPU is busy. Instead, DMA transfers depend on the consistently fixed MCU internal bus clock. The synchronization algorithm commences when the master transmits a *sync code*. Each receiving slave module immediately forwards the code to its designated neighbors, and then pauses for a specific propagation delay. This delay is fixed and depends only on the number of hops in the array. Thus, a frame-level synchronization-up to a *microsecond*-resolution-can be achieved.

### *4.2.2 Array Electrical Backbone*

After the array optical design is complete, its electrical properties must be defined, including delays, sampling rate, and data reporting techniques. Each sampling cycle (i.e., *scan*) consists of two main processes: *uploading* (or synchronization) wherein the master module transmits a sync code to all slave modules, and *downloading* where the master collects measured samples from all modules. Samples are collected via DMA streams designed to streamline the process as much as possible.

Successful data reporting requires that efficient and non-overlapping communication routes are planned throughout the array. Routes built from DMA streams will be used for both synchronization (i.e., port-to-port) and downloading (i.e., port-to-memory) processes. *Array Depth* is the maximum number of hops required for routes, and it directly affects the scan delay (i.e., maximum rate at which the entire array can be scanned). Array depth can be minimized by devising additional parallel routes that combine at *multiplexing* modules.

Figure 4.1 illustrates example communication routes in a flat 37-module array. First, module 1 is arbitrarily chosen as the master node and then the electrical backbone is designed. Maximum array depth following any route remains at six hops, while propagation delay in various routes is balanced as much as possible. Modules 1, 3, 12, 23, and 24 are multiplexing nodes that combine multiple data streams from various ports before forwarding them to the subsequent destination. Propagation delay at a multiplexing node should be set according to its deepest route (i.e., the

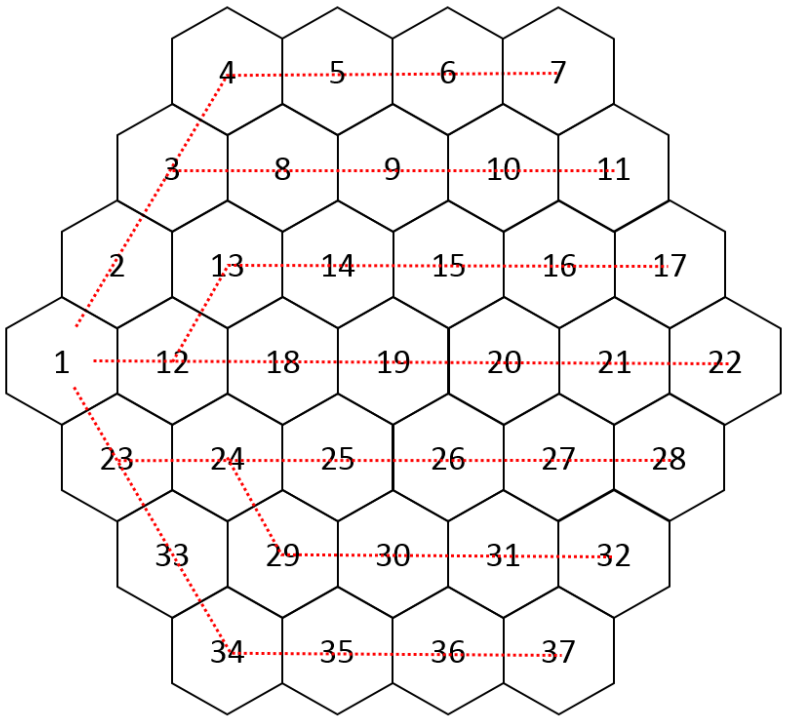


**Figure 4.1. Example of DMA routes (or electrical backbone) in a 37-module flat hexagonal array.**

route branch with maximum number of hops). Scan rate in this array could easily reach 1000 Hz given that each module is sending a two-byte value. Algorithms 1 and 2 provide a high-level representation of master and slave algorithms, respectively.

**Algorithm 1** Master's scan algorithm.

```
1:  while 1 do                                              ▷ Infinite loop
2:      if Timer has expired then
3:          Transmit a sync code
4:          Wait for propagation                            ▷ Based on maximum depth
5:          Sample the ADC
6:          Write ADC samples into buffer
7:          Wait till data from all modules are downloaded
8:          Send all measurements to user
9:          Reset the buffer
10:     else
11:         Wait
12:     end if
13: end while
```

**Algorithm 2** Slave's scan algorithm.

```
1:  while 1 do                                              ▷ Infinite loop
2:      if Sync code was received then
3:          Wait for propagation                            ▷ Based on module depth
4:          Sample the ADC
5:          Write ADC samples into buffer
6:          Wait till data from previous modules are downloaded
7:          Forward the buffer to next module
8:          Reset the buffer
9:      else
10:         Wait
11:     end if
12: end while
```

## 4.3. Design Examples

In the following sections, MOWE-based detector array examples are featured so as to showcase their characteristics and potential, as well as to stimulate further ideas and applications. Four examples are included: (a) a large flat array, (b) a spherical omnidirectional array, (c) an optically-inhomogeneous flat array, and (d) a tube-shaped array.

### *4.3.1 Large Flat Arrays*

The 37-module flat hexagonal array analyzed in Figure 4.1 was constructed to demonstrate arrays with large spatial coverage (See Figure 4.2). The combined FoV cross-section area is $299.8cm^2$ at the convergence distance, where $d_R = 8.66mm$ from the array surface. Maximum measured scan rate reached $794Hz$ when reporting 74 bytes per scan. Additional tuning, as well as increasing the serial ports baudrate, can increase the scan rate well above $1KHz$. Each module samples FoV with a 12-bit ADC and reports the result in a 16-bit value, which renders the four most significant bits

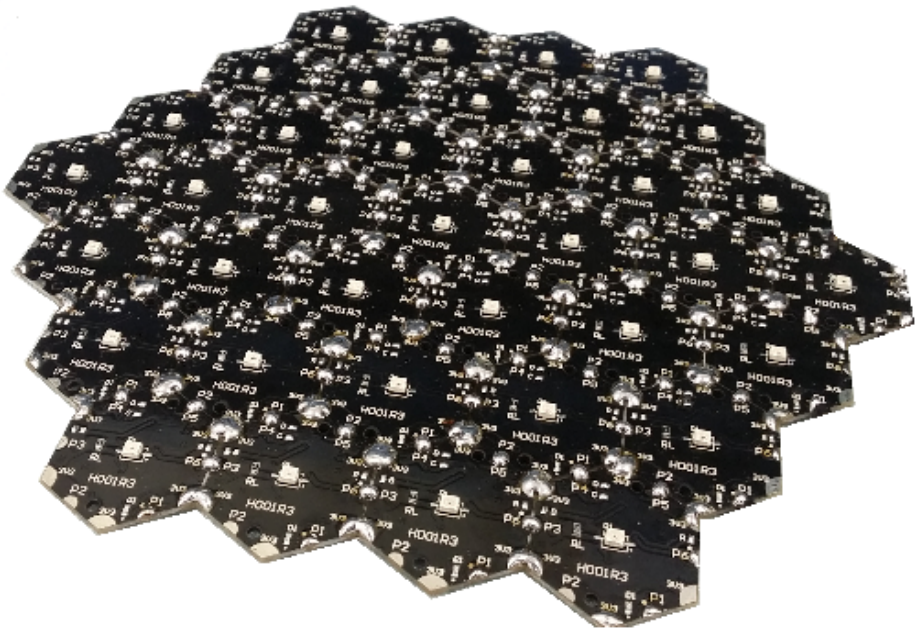

**Figure 4.2. 37-module flat hexagonal detector array.**

(MSB) redundant. (These bits can be used for signaling or for data integrity.) The array measures 21$cm$ from corner to corner, weighs about 75 grams, and costs less than $200 to fabricate.

Figure 4.3.a shows a plot for array measurements of background light in a lab environment. The discrete red markers are actual array measurements (i.e., FoV samples). Natural (or Gaussian) interpolation is used to predict intensity values between discrete samples. Intensity values in the color map are in ADC units (i.e., counts). Although no external passive stimulation (i.e., object blocking the background light) or active stimulation (i.e., directed light beam) is available, the array shows intensity

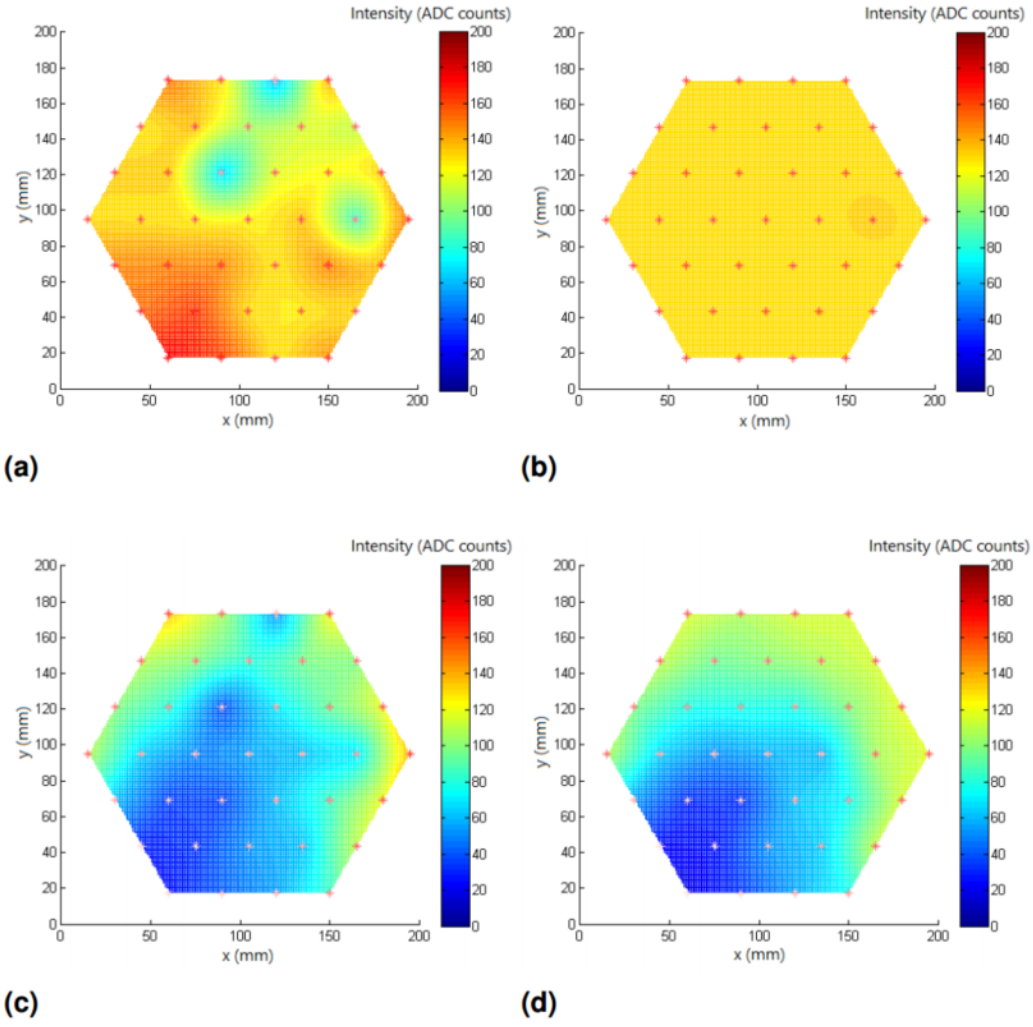


**Figure 4.3. Equalized and unequalized passive detection in a 37-module flat array.**

variations between the modules. This result is attributable to a number of factors in the fabrication and assembly process (e.g., variations in optical components characteristics, assembly tolerances, variations in PT load resistance, and others). Optical inhomogeneity can be easily removed in software through simple filtering and signal processing techniques. Figure 4.3.b shows measurements after the array is equalized.

Figures 4.3.c and 4.3.d show un-equalized and equalized passive detection, respectively, of an object (here, a human hand) blocking the background light. Passive detection is useful in applications such as proximity sensing and touch-less gesture detection. Visualizations 1 and 2 [57, 58] show passive detection animation. Close-range motion detection serves as another application. Room-range detection is also possible with higher sensitivity detectors. Although MOWE-based detector arrays

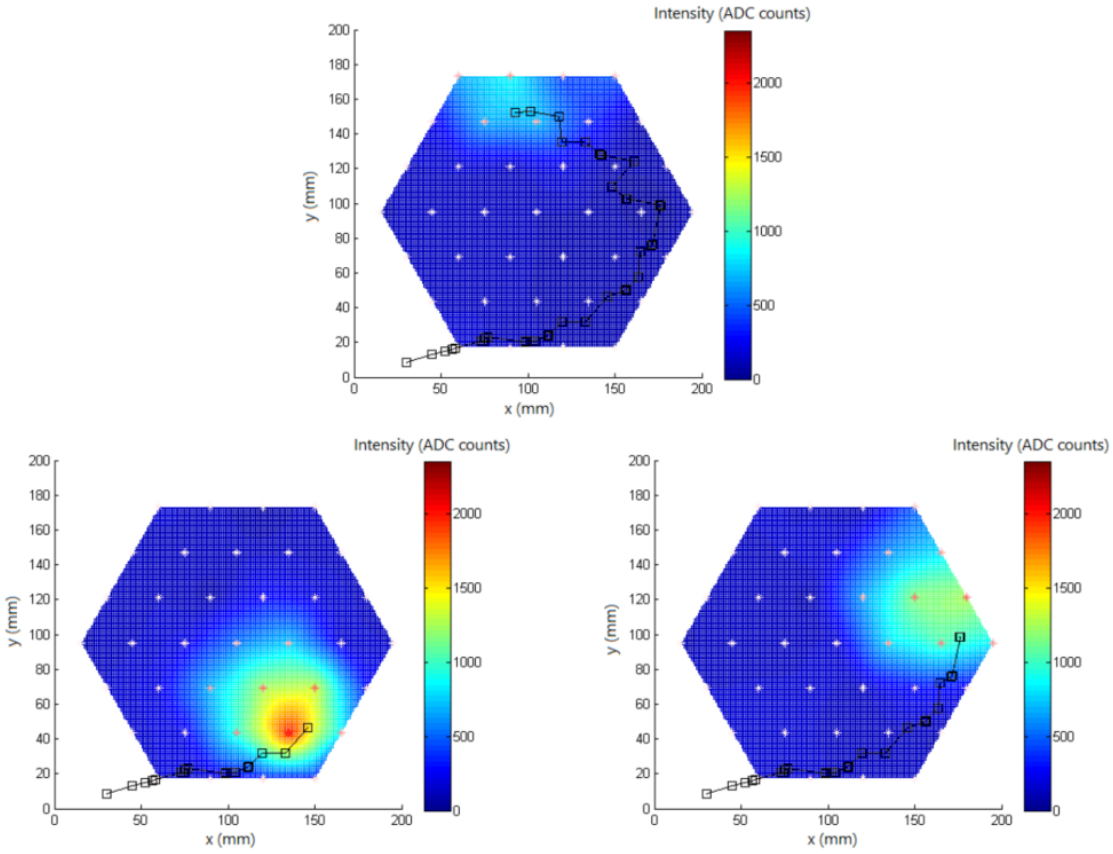


**Figure 4.4. Active detection and tracking of a single light beam in the flat array.**

cannot provide a competitive resolution when compared with other types of FPAs (e.g., CMOS and CCDs), the novel solution has a fast scan rate advantage. Notably, most detection applications do not require high resolution, as the image is reduced to a small number of IR or visible markers, totaling only a few pixels. Whereas expensive motion tracking cameras achieve at best a few thousand frames per second (*fps*) with limited FoV, MOWE-based detector arrays at their current specifications achieve at least 1000*fps* or more while providing exceedingly wide FoV, as shown earlier.

Figure 4.4 shows active detection and tracking of a single light beam. All three frames (starting from left bottom) illustrate the mobile beam passing through the array, while being detected and tracked by a simple tracking algorithm. Interested readers can see Visualization 3 [59] for more information about active detection and tracking animation. Figure 4.5 features three snapshots from Visualization 4 [60]

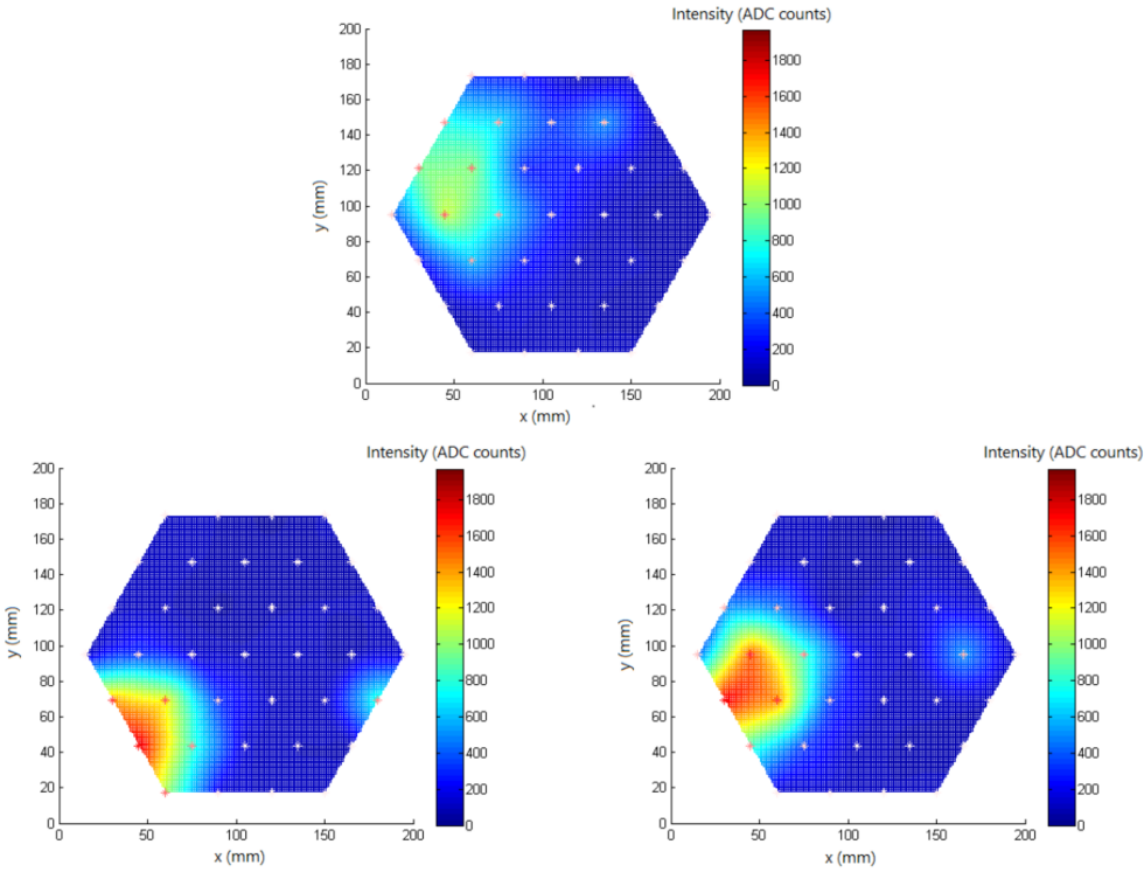


**Figure 4.5. Measurements of multiple light beams in a flat array.**

showing two light beams with various intensities moving across the array. Notably, the detection and tracking problem becomes more challenging, especially when beams overlap. This calls for the use of innovative signal processing and filtering techniques or perhaps borrowing ideas from machine vision and image/video processing algorithms. Again, the purpose of this section is not to discuss detection and tracking algorithms, rather the goal is to illustrate features and capabilities of MOWE-based detector arrays.

The last experiment using this array is concerned with velocity estimation of fast passive/active mobile objects. Figure 4.6 shows the time domain intensity measurements of an object crossing the array near its long diagonal. Seven modules of the long diagonal (34, 29, 25, 19, 15, 10, and 7) are shown. The active object generated clear pulses that can be used to calculate time difference, hence velocity, accurately. Time difference between pulse peaks is $20msec$; therefore, ve-

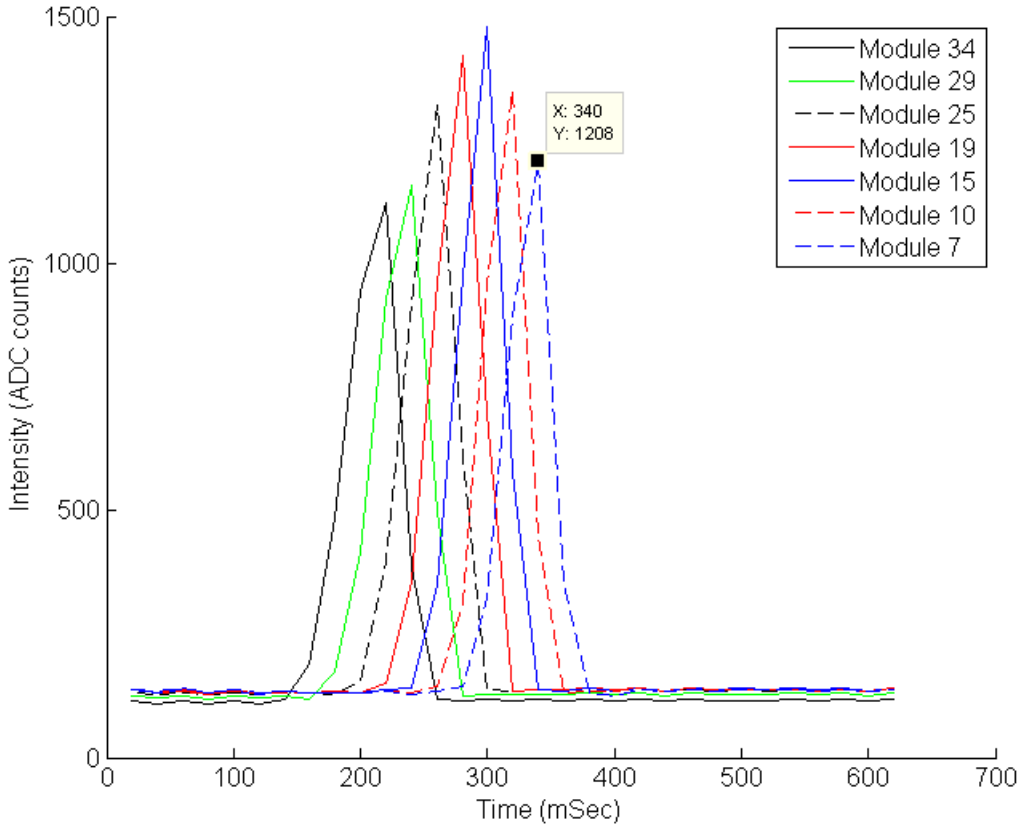


**Figure 4.6. Velocity estimation in a flat $30mm$-resolution array.**

locity is estimated at $30mm/20msec = 1.5m/sec$. This example array can measure a max velocity of $30mm/(1/794Hz) = 23.82m/sec \approx 52mph$ at its full resolution. However, at the lowest possible resolution (i.e., when the object is only detected by the two most separated modules) maximum detected velocity reaches $180mm/(1/794Hz) = 142.9m/sec \approx 320mph$, given that intensity pulses can be clearly identified from noise.

### *4.3.2 Spherical Omnidirectional Arrays*

A truncated icosahedron (e.g., soccer ball) is comprised of 20 hexagons and 12 pentagons. This shape is used to construct a spherical array using hexagonal faces only, thus achieving low complexity, omnidirectional FoV, and contiguous array design (See Figure 4.7). Figure 4.8 shows the assembled array with its 3D-printed protecting frame and holder. The array is shown in two configurations measuring background light in a lab environment. The top graphs illustrate reconstructed FoV based on discrete intensity measurements. Black markers represent discrete spatial samples taken by the array. Intensity values in ADC units are then 3D-interpolated, and the interpolant is evaluated at a sphere surface that closely matches array dimensions. The configuration pictured on the right demonstrates the array FoV northern hemisphere open from all directions and measuring florescent light from the ceiling. The configuration pictured on left has its FoV blocked from most directions except where

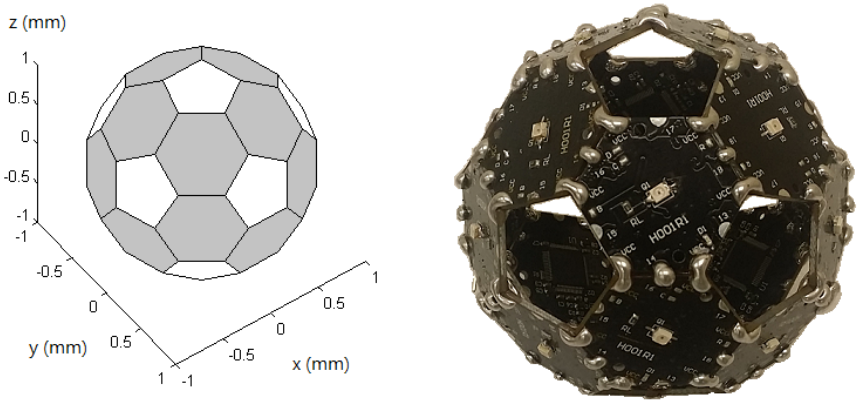


**Figure 4.7. Spherical detector array based on a truncated icosahedron.**

it faces the reader, which is apparent from the reconstructed FoV graph located above the photos.

The array electrical backbone was designed as five parallel routes with maximum array depth of 5 hops. Maximum measured scan rate reached $1581Hz$ when reporting a 16-bit value per module. Figure 4.9 plots a number of (though not all) module measurements for a passive object passing nearby. Reconstructed FoV is shown at two time epochs−one just before the object had passed and the other in the middle of its passage.

The final experiment for this array (See Figure 4.10) is a reconstruction of a

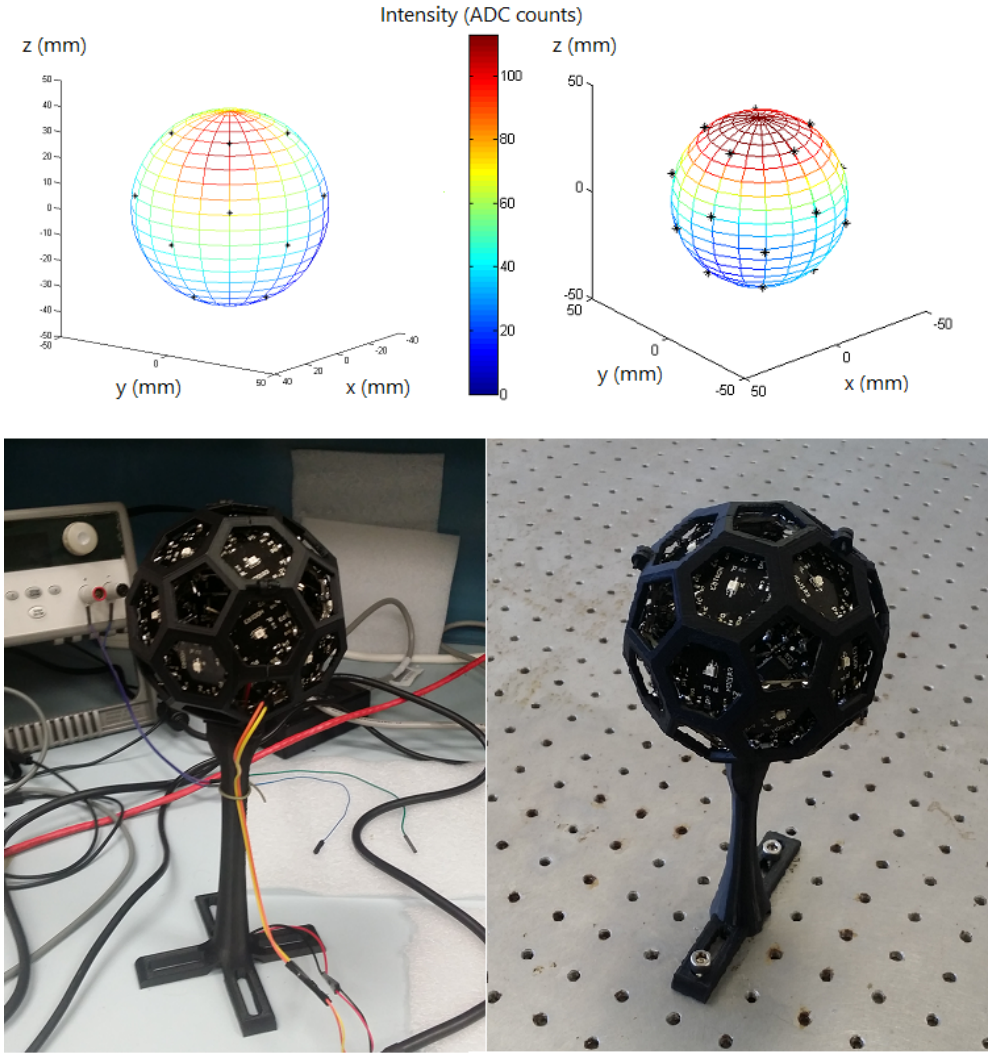


**Figure 4.8. Background light measurements and reconstructed FoV of a spherical array.**

mobile active object rotating around the array−Visualization 5 [61]. Both object directionality and its approximate distance to the array can be determined based on the detector's power/distance characteristic curve. Table 4.1 lists specifications for the spherical terminal prototype.

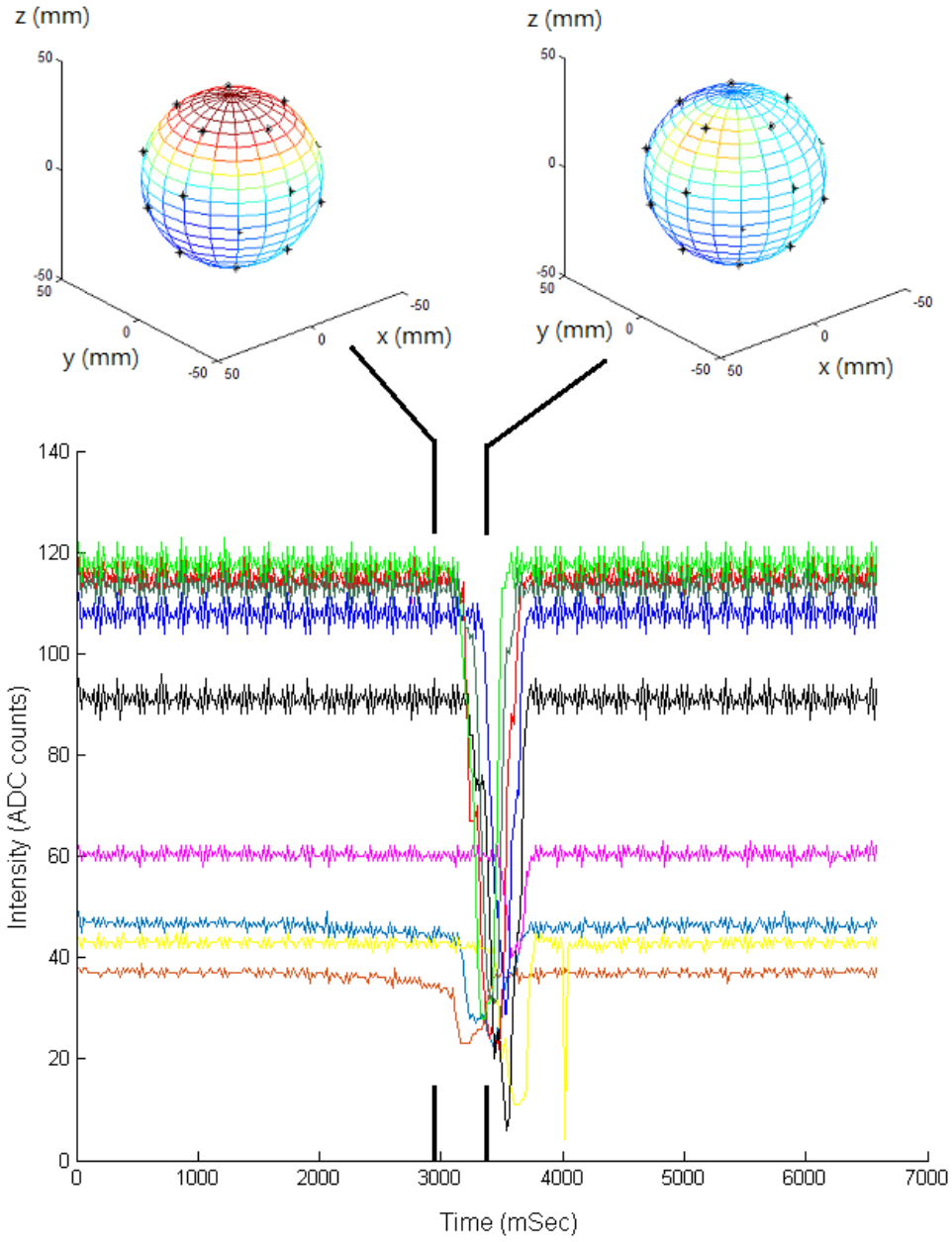


**Figure 4.9. Detection of a passive mobile object in the spherical array (Not all modules shown.)**

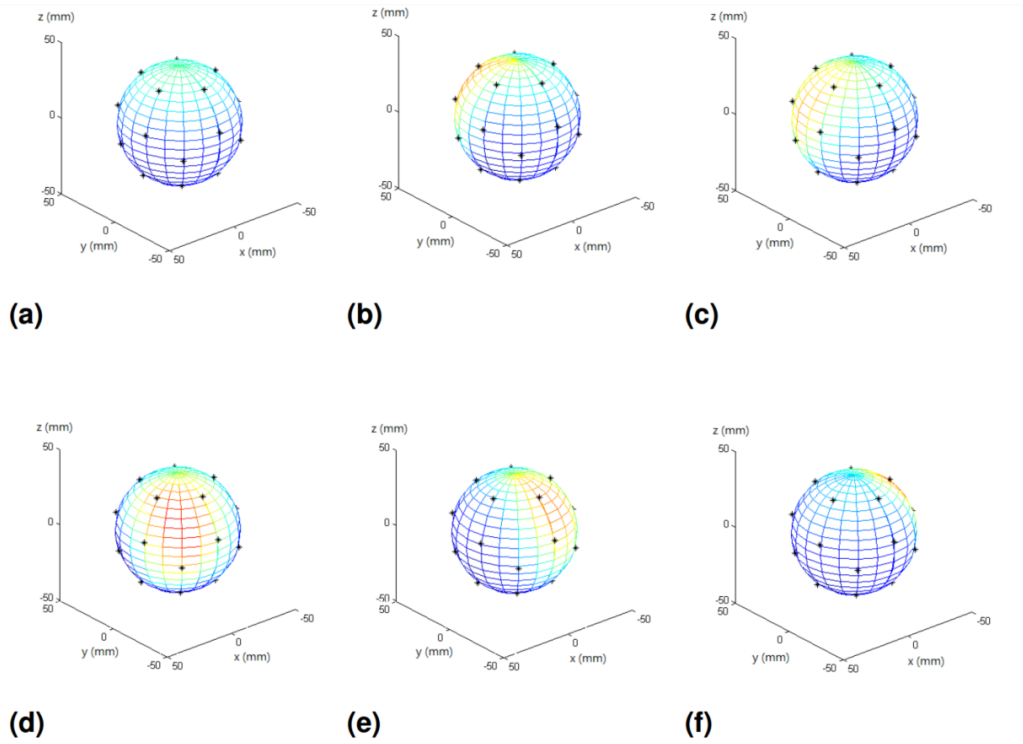


**Figure 4.10. Measurements-based reconstruction of an active object rotating around the spherical array.**

**Table 4.1. Rough Estimates of Spherical Omnidirectional Terminal Specifications**

| **Model** | **All-receivers** | **Hexagon-only-receivers** | **Transceiver** |
|---|---|---|---|
| Modules weight ($g$) | 58 | 40 | 58 |
| Extra weight for solder and cables ($g$) | 32 | 20 | 32 |
| Frame weight ($g$) | 55 | 55 | 55 |
| Optical table holder weight ($g$) | 25 | 25 | 25 |
| Hook attachment weight ($g$) | 5 | 5 | 5 |
| Total weight using the holder ($g$) | 170 | 140 | 170 |
| Total weight using the hook ($g$) | 150 | 120 | 150 |
| Terminal cost without an external controller (\$) | 200 | 150 | 200 |
| Assembly time ($minutes$) | 180 | 120 | 180 |
| Terminal power consumption (without sleep mode) ($mW$) | 1267-2112 | 792-1320 | 1267-2112 |

### *4.3.3 Optically-inhomogeneous Arrays*

Detector arrays do not have to be optically homogeneous. One can mix detectors with different wavelength, sensitivity, and FoV to achieve desired optical characteristics. A 12-module flat inhomogeneous array was constructed from six $850nm$ and six $940nm$ detectors. The $940nm$ detectors came equipped with a daylight filter, making them sensitive mostly to infrared wavelengths. The array shown in Figure 4.11 was subjected to the following test. First, an $850nm$ laser was shot on the array through a diverging lens so that it can cover the entire array. Next, the experiment was repeated with a $980nm$ laser. (Notably, the beam did not cover the entire array.) Figure 4.12 shows a snapshot of array measurements for the $850nm$ laser. As expected, only respective detectors at $850nm$ (solid white) captured the laser. The $980nm$ laser was captured by both types of detectors, as shown in Figure 4.13. Maximum scan rate for this array was near $2500Hz$.

To demonstrate wavelength diversity in MOWE-based arrays, the following experiment was conducted wherein the inhomogeneous array was used to detect and decode two transmitters, one at $850nm$ and another at $980nm$, both shining at the


**Figure 4.11. 12-module flat array with $850nm$ detectors (solid white) and $940nm$ detectors (white with black dot).**

array at the same time and sending different data streams. A single $850nm$ module would receive both signals, overlapped, and thus cannot decode them. However, by communicating with the neighboring $940nm$ module that received only the $980nm$ signal, the $850nm$ module was able to decode both signals by performing basic signal processing. Similar collaborative, array-based algorithms can be developed to separate multi-user streams and decode communication in noisy environments by utilizing array spatial and wavelength diversity.

Figure 4.14 shows experimental results. CH1 (up) is the digitized overlapping signal received at the $850nm$ detector. The normal digitization threshold is unable to decode data correctly or separate the two streams. CH3 (bottom) is the digitized $980nm$ signal after it is measured by the $940nm$ detector, and then forwarded to the $850nm$ module. As expected, some inter-array communication errors and delays might affect the measured signal, especially at low sampling rates. Nonetheless, this does not prevent the other signal from being decoded correctly most of the time. Finally, CH2 (middle) is the decoder output−the decoded $850nm$ signal that was originally overlapping and not separable with a simple threshold. The array was

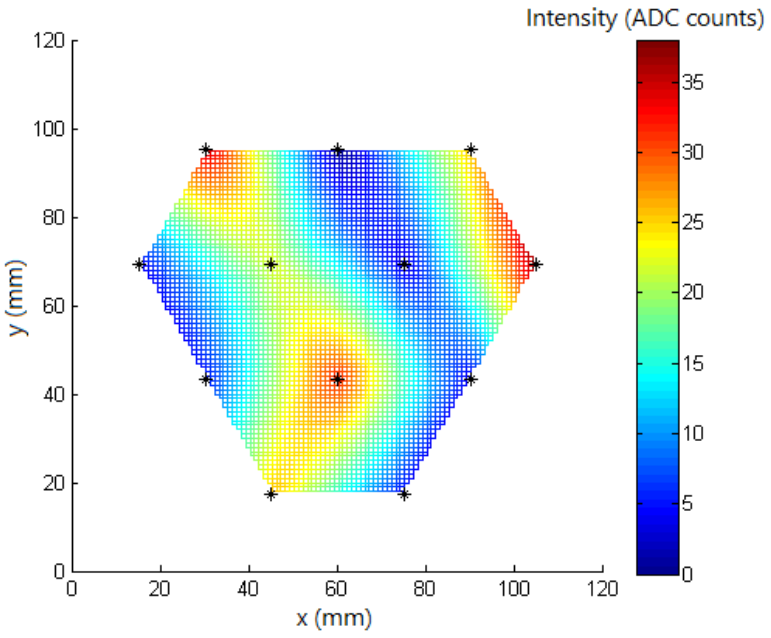


**Figure 4.12. $850nm$-laser measurements using the optically inhomogeneous array.**

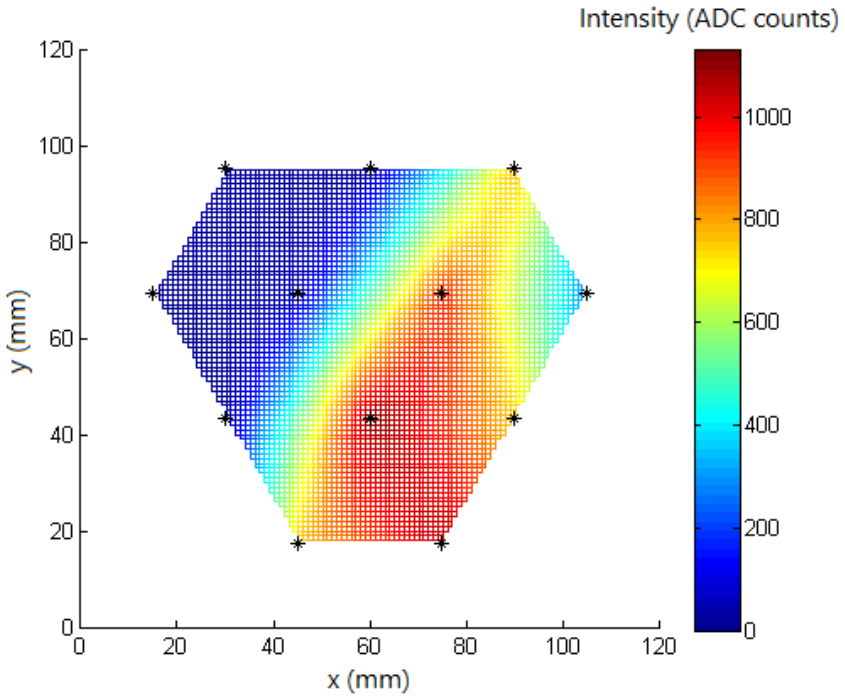


**Figure 4.13. 980*nm*-laser measurements using the optically inhomogeneous array.**

sampled at $500Hz$ in this experiment, and transmitter signals were random streams at $1Hz$ and $10Hz$ for the $850nm$ and the $980nm$ lasers, respectively. These figures are a proof-of-concept and can be increased many fold. It is also worth noting that this simple experiment can be expanded in many directions to feature more detectors, different geometries, and more wavelengths.

Finally, a simple experiment was conducted to showcase turbulence effects on received signal strength. Figure 4.15 shows measurements of a single $850nm$ module in a clear channel, a weak lab-induced turbulence state ($C_n^2 = 3 \times 10^{-13}\ m^{-2/3}$), and a strong lab-induced turbulence state ($C_n^2 = 1 \times 10^{-11}\ m^{-2/3}$). The laser was modulated with a random binary sequence at $1Hz$. The figure confirms relative degradation of signal (intensity) for both 1's and 0's when moving from a clear channel to a turbulent one. Figure 4.16 shows the experimental lab setup.

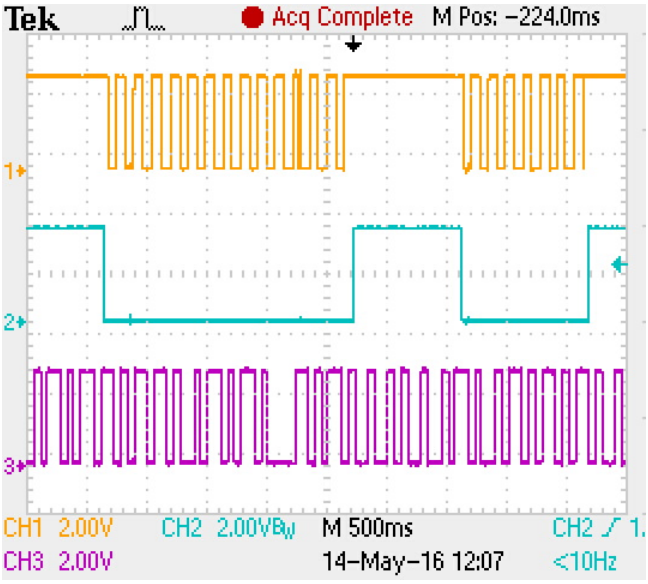


**Figure 4.14. Decoding two overlapping signals by utilizing wavelength diversity in an optically-inhomogeneous MOWE array. Up: two overlapping signals at 850$nm$ and 980$nm$. Middle: the decoded 850$nm$ signal at $1Hz$. Bottom: the measured 980$nm$ signal at $10Hz$. Note that these are not analog intensity values measured directly rather a digitized representative version measured on the MCU output pins.**

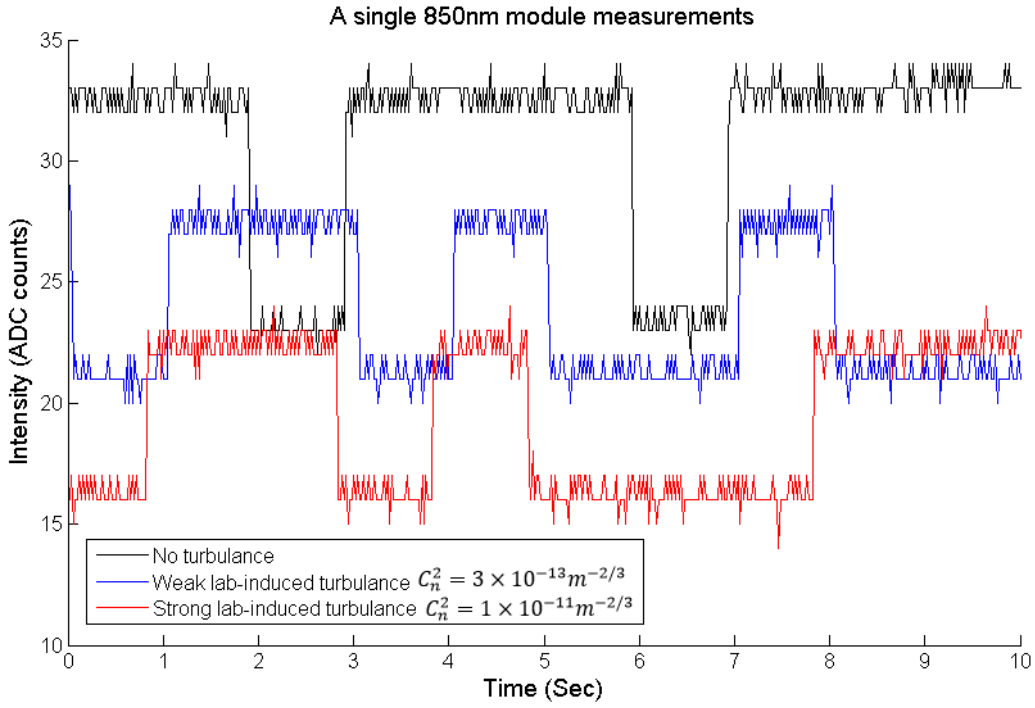


**Figure 4.15. Turbulence effects on 850$nm$-laser intensity.**

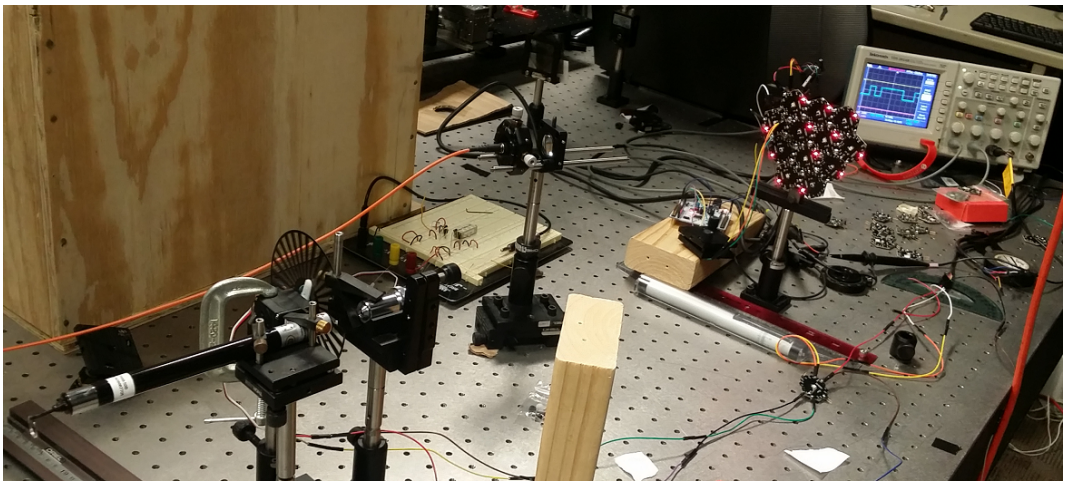

**Figure 4.16. The flat optically-inhomogeneous array lab setup. The array is subjected to two different laser sources at the same time: a 850$nm$ laser modulated by a pseudo-random generator and delivered via a single-mode fiber, and a 980$nm$ laser modulated by a rotating disc attached to a servo motor. The servo motor is controlled by a MOWE module as well. The wooden turbulence-generating box to the upper left is used in turbulence emulation experiments.**

### *4.3.4 Odd-shaped Arrays*

This section demonstrates the use of MOWE modules to create complex arrays with odd-shapes or configurations that allow for innovative applications. Earlier in this section, it was shown that fast-moving objects can be detected and tracked and how their velocity measured in two dimensions. Here, this concept is extended into three dimensions by tracking the object in both horizontal and vertical planes.

The device presented herein and shown in Figure 4.17 consists of three consecutive detector rings, wherein detectors are assembled inwards. This design allows detectors to *monitor* the FoV inside each ring from eight equally spaced directions. Each ring provides *continuous* object tracking in its own vertical plane, and the collection of rings provides *discrete* object tracking across the horizontal plane. Rings are linked together via two modules that are only used to pass data, effectively acting as wires with some delay. Each ring has eight detectors and measures approximately 70$mm$ in diameter. Ring-to-ring separation is approximately 50mm. The array showed a maximum scan rate of 1300$Hz$ in experiments.

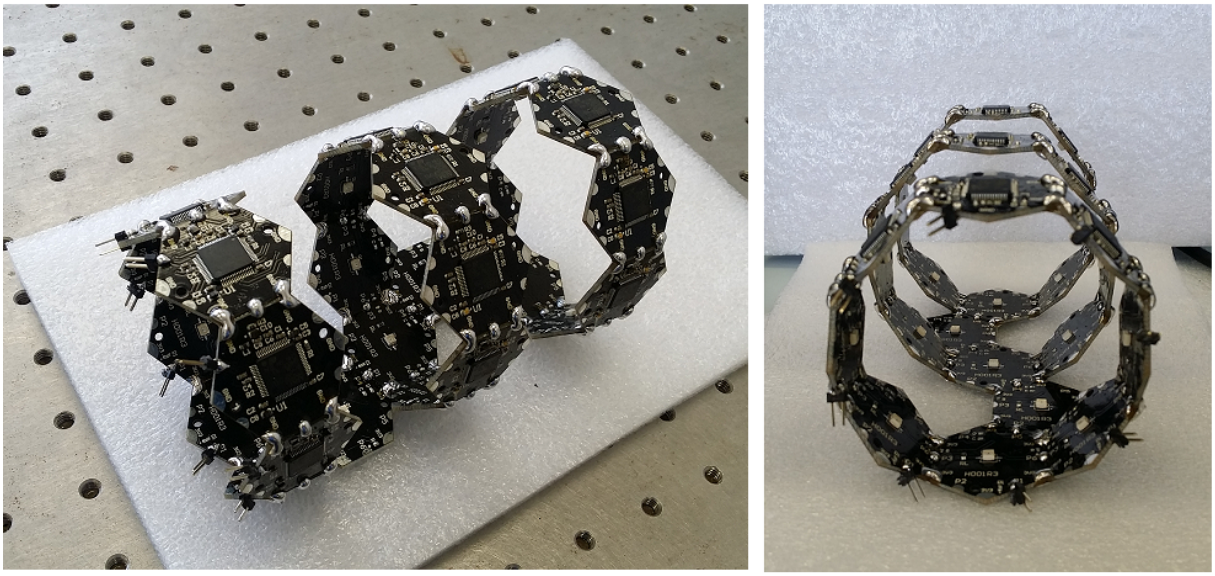

**Figure 4.17. Example of a complex, odd-shaped detector array. A *tube* design for tracking objects across vertical and horizontal plains.**

The *tube* array is based on *passive* tracking (i.e., an object blocks the ambient background light while moving through the tube, thus providing a means for detection and tracking). This method requires initial measurement and characterization of ambient light before detection is possible. Active tracking can also be implemented by shining visible or infrared light inside the tube and measuring reflections, thus providing higher accuracy and immunity to ambient light variations. Transmitter MOWE modules or external light sources can be embedded in the array for such purposes.

# Chapter 5: Software & Cognitive Optics

## 5.1. Introduction

The concept of a programmable digital radio (i.e., a radio system with its parameters coded in software and easily modified on the fly) stemmed from military needs to unify dozens of legacy wireless communication systems in a single configurable device. DoD and DARPA funded projects, such as SPEAKeasy and the Joint Tactical Radio System (JTRS), were fundamental to ramp up research efforts into what has become known as software-defined radio (SDR)−and later cognitive radio (CR) technology [62]. Nevertheless, the most influential force bringing SDR to the masses was the advent of open-source community-based projects such as the widely known Gnu Radio, using Universal Software Radio Peripheral (USRP) SDR [48,63]. Such projects inherited the works and traditions of two highly engaged collaborative communities, namely the Amateur Radio community and the Open Source Software movement.

Once the concept of SDR matured and computing resources (e.g., digital signal processors [DSPs] and general-purpose processors [GPPs]) became fairly accessible in the late 1990s, adding more intelligence to the radio design was the next logical step. In 1998, Joseph Mitola coined the term Cognitive Radio (CR) to describe a system wherein the wireless device and its related networks are aware of radio resources, user needs, and the application context with the goal of providing optimal functionality. Although much of what Mitola described in terms of the ideal cognitive radio (iCR) functionality is now implemented in present day smartphones, the need for self-adaptable, intelligent radio transceivers has since grown with the increasingly crowded spectrum and the need to hunt spectrum white spaces or negotiate busy ISM bands.

The situation is different in the THz regime. FSO communication—long dominated by large military and space demonstrations—has not progressed significantly from the long-range, high-power, point A-to-point B links. A number of reasons could be cited for this phenomenon. First, the inherent directivity and limited coverage of light waves implies sophisticated PAT technology is needed. Widespread mechanical gimbals proved irrelevant for many applications due to their size, weight, and reliability concerns. Second, rapid advances in the past two decades in RF technology, especially for mobile platforms, have nearly eliminated the case for optics in mobile, multi-user environments. (This situation literally occurred when WiFi outpaced IR for indoor wireless broadband.) Third, FSO technology, depending primarily on lasers, has not been easy to integrate within mass-produced semiconductor chips and densely packed printed circuit boards, both of which are basic pillars of present-day personal communication devices.

All of this, however, is due to change as opportunities and advancements open new markets for FSO. The technology has even been re-branded for short- and medium-range. Following a steady decline over the past decade of government funding for long-range applications, the industry has been increasingly interested in exploring FSO for 5G cellular communication, wireless LANs and indoor broadband wireless communication, and localization, among other uses. Optical wireless is the latest term mostly used to differentiate these venues from point-to-point, long-range, traditional FSO. Recent challenges facing RF communication (e.g., privacy, coexistence, interference, and spectrum costs) have reignited the search for a long-term solution. Advances in photonics integrated circuits and vertical-cavity surface-emitting lasers (VCSELs) are forging communication-grade optical transmitters and receivers into mass production. Furthermore, innovations in bio-inspired optics, fiber bundles, and modular optical/electrical elements promise an alternative to bulky gimbals. With optical communication closer to the end-user and more integrated into consumer devices, there is a need to incorporate additional intelligence and agility for adapting to user needs and environmental conditions.

One element in the optical communication stack, however, has already enjoyed some *softwarization* and agility, namely the network side. Software-defined optical networks (SDONs) [64] borrow similar concepts currently nurtured within the networking community in software-defined networks (SDNs) and apply them to terrestrial fiber networks to reduce costs and provide more services. Although optical wireless terminals eventually interface directly with terrestrial networks−whether fiber optic or copper, the analysis in this section is focused on softwarization of the optical wireless physical layer without advancing into higher layers. The following sections will discuss the MOWE-centered vision of SDOs and COs, and will detail how they compare to present-day SDRs and CRs. The purpose is not to provide a complete analysis of SDO and CO architecture, but rather to shine light on various ideas and to show how they can be easily prototyped using MOWE.

## 5.2. Software-defined Radio

Software Defined Radio (SDR) is a flexible and reconfigurable radio communications architecture in which the functionality associated with Physical Layer (PHY) is implemented, in part or in total, through Digital Signal Processing (DSP), effectively emulating the same operations that take place in equivalent analog circuitry. DSP yields docility, upgradeability, and adaptability to system operation within certain bounds as given by the actual system [62, 65].

For the last 20 years, SDR has been the topic of great interest, garnering extensive research and development for both military and commercial use [66]. In the Radio Frequency (RF) domain, communications technologies found in widely used devices, such as smartphones, greatly appeal to SDR's reconfigurable nature, as they inherently include a multitude of radios optimized for various signals in different frequency bands. Examples include Wi-Fi $2.4GHz$ & $5GHz$, Long Term Evolution (LTE) $800MHz$, Global System for Mobile Communications (GSM) $900MHz$, Universal Mobile Telecommunications System (UMTS) $2.1GHz$, Global Positioning System (GPS) $1.5GHz$, Bluetooth $2.4GHz$, Near Field Communications (NFC) $13.56MHz$, and FM radio, to name a few. Furthermore, future devices will also include radios that operate custom waveforms catered to the Internet of Things (IoT) and its applications.

From a conceptual standpoint, the ideal SDR, which is yet to be realized commercially [66], would capture and digitize all the aforementioned wide range of signals. It would comprise only of an RF section (e.g., antenna, amplifiers and filters) and a very high speed Analog-to-Digital Converter (ADC) and Digital-to-Analog Converter (DAC) pair that have been interfaced with a powerful DSP processor or computing system (e.g., FPGA). The move to sample RF signals directly, and down-convert them to baseband in a single stage is possible only through major advancements currently underway in hardware design and embedded systems manufacturing.

Conventionally, digital hardware radio systems consist of five cardinal segments: 1) antenna, which receives (or transmits) information encoded in radio waves; 2) RF front-end, responsible for transmitting/receiving RF signals from the antenna and converting them to an intermediate frequency (IF); 3) ADC/DAC, which performs analog-to-digital/digital-to-analog conversion; 4) digital up-conversion (DUC) and digital down-conversion (DDC) blocks, where signal modulation and demodulation is performed; and finally, 5) baseband (BB) segment, which performs operations such as coding/decoding, equalization, and frequency hopping, and also implements the link layer protocol. However, a number of challenges still remain in the transition from hardware radio to an SDR [66]. First, the transition from hardware to

software processing results in a substantially increased computation, which causes an increased power consumption. This reduces battery life and is a key factor in explaining why SDR has not been deployed in end-user devices. Rather SDR is used in base stations and access points that leverage external power resources. Second, because the ultimate goal for software radio is moving the ADC/DAC conversion as close as possible to the antenna, digitization of the RF signal requires the incoming signal to be sampled at a rate at least multiple times the Nyquist frequency. Additionally, the higher the data rate is, the higher the resolution required. Taken together, high-bandwidth, high-frequency transmissions require very high sampling rates. The ability to inexpensively support such sampling rates limits the range of signals that can be digitized.

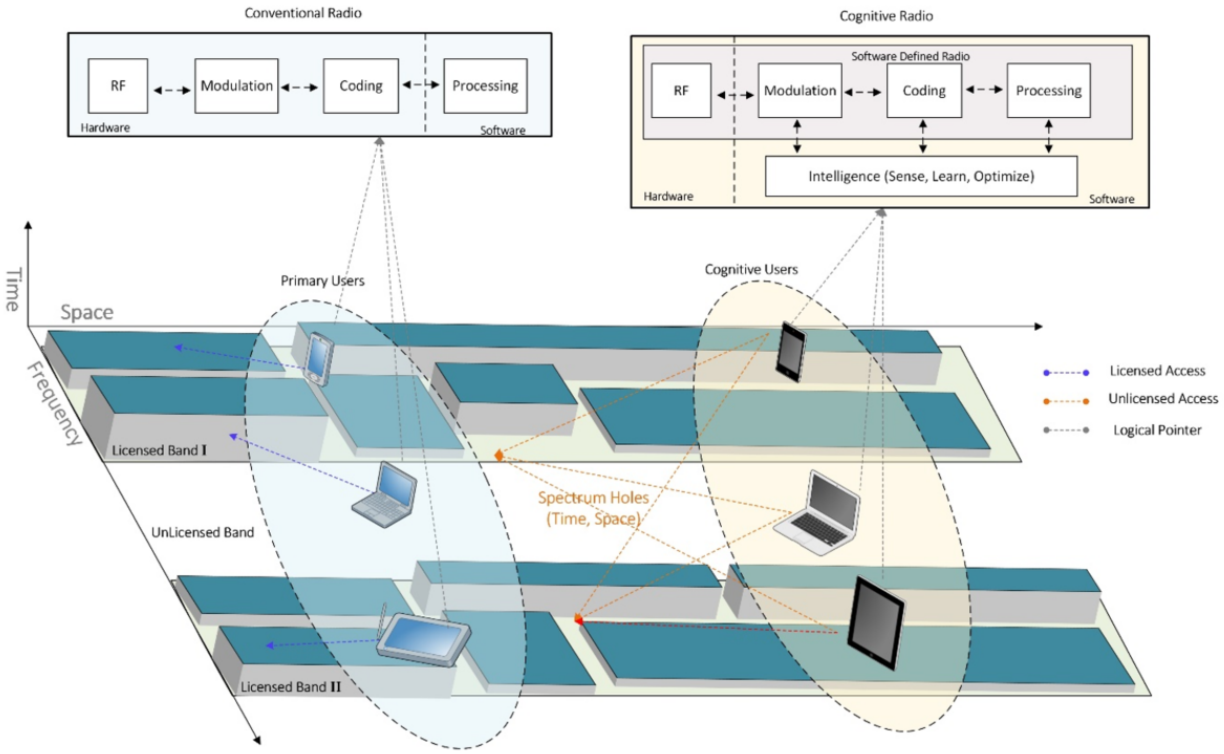


**Figure 5.1. Conceptual dynamic access network contrasting traditional radio, software radio, and cognitive radio.**

## 5.3. Cognitive Radio

The re-configurability offered by SDR enables on-the-fly adaptability of radio functionality and operations as needed. However, an SDR is not capable of optimal reconfiguration without user assessment and intervention. Conversely, a Cognitive Radio (CR) integrates model-based reasoning along with software radio, thus becoming trainable, perceptible, aware, and intelligent in a broad sense, analogous to the mental process of cognition [67, 68].

It follows from this discussion that cognitive radio functionality requires the system be at minimum: 1) Supple and agile−to change the waveform and other radio operational parameters on the fly, which is only possible when CRs are built on top of SDRs; 2) Sensible−to observe and measure the state of the environment surrounding the device (i.e., spectral occupancy, channel idle time, link quality and other wireless channel characteristics); and 3) Trainable and cognizant−to analyze sensory inputs, identify patterns, and recognize ambient characteristics, which accordingly allow the system to modify internal operational behavior as a result of the learning mechanism. This is not to be confused with methods that rely on pre-coded algorithms (e.g., IEEE 802.11 MAC layer, which adapts transmission activity to channel availability, by using a predefined listen-before-talk and exponential back-off algorithm as opposed to a cognitive cycle).

Figure 5.1 illustrates a conceptual dynamic access network involving both SDR and CR devices operating alongside conventional radio users. Notably, cognitive users apply sensing, learning, and optimization to their SDRs to opportunistically access spectrum holes available in licensed bands in which primary users occupy.

## 5.4. Software-defined Optics

Analyzing basic components of an SDR helps deduce its optical counterpart. Table 5.1 lists key SDR components and functionality combining them in three groups: a reconfigurable digital radio, a software tunable analog radio, and a software tunable antenna system. As shown in the table, most RF functionalities have a match or a near-match in the optical domain. The table also pinpoints the availability of these features in current MOWE implementation. Although some features are not currently available, most SDO functionalities can be realized, in a way or another, using programmable MOWE modules and arrays.

Constructing and generating customized waveforms is a basic feature of software radios. Specific optical waveforms can be similarly designed in advance and stored in memory to be generated later whenever needed. RF center frequency is utilized in many channel access schemes to provide multiple access or assist in canceling interference. Same concept can be adapted in optics by controlling wavelength. Switching between receivers and transmitters with different wavelengths (or using multi-wavelength LEDs and PDs) provides simultaneous, interference-free links and helps mitigate wavelength-related turbulence and interference.

SDRs are expected to multiplex various data streams with different antennas. In MOWE-based SDO, switching and multiplexing can be handled in software, and then applied to data streams. Although slower than all-optical systems, MOWE-based switching and beam steering still achieve much higher bandwidth−and better SWaP−than all available mechanical solutions, as demonstrated in the experiments in Section 6.2. Nonetheless, an all-optical, highly configurable, and intelligent system is also attainable by combining MOWE with fiber-bundle technology as suggested in Section 7.1.

Power control is another essential characteristic of any SDR. Similarly for optics, power control helps simultaneously avoid interference and preserve device battery. Power control can be implemented in MOWE by switching multiple transmitters at the same time, which yields higher intensity and larger beam footprint. This strat-

**Table 5.1. Comparing Software-defined Radio and Software-defined Optics**

| SDR Components | RF Functionality | Matching Optical Functionality | Available currently in MOWE? | Implementation Details |
|---|---|---|---|---|
| **Reconfigurable Digital Radio** | Waveform generation | Waveform generation | Yes | The MCU recalls stored waveforms and performs modulation, source and channel coding, etc. |
| | Frequency plan (e.g., bandwidth, center frequency) | Wavelength | Yes | Receivers/transmitters with different wavelengths can be switched on and off. |
| | Power spectrum specifications | Transmission power, receiver sensitivity | Yes | Multiple transmitters can be combined to increase TX power. |
| | Software tunable data converters (ADC, DAC) | ADC, DAC | Yes | TX is driven via PWM. |
| **Software Tunable Analog Radio** | PA, LNA | Optical amplifiers, electrical amplifiers | No | |
| | Filters | Optical filters, electrical filters | No | |
| | Duplexing devices | Switching/ Duplexing | Yes | DMAs can be used to switch, route, and multiplex signals. |
| | Power management | Power management | Yes | |
| | Impedance Synthesizer | - | No | Not needed. |

| | | | | |
|---|---|---|---|---|
| **Software Tunable Antenna System** | MIMO and spatial diversity | MIMO and spatial and angular diversity | Yes | Uncorrelated modules can be used in a MIMO configuration. |
| | Adaptive beamforming | Adaptive beamforming | Yes | Correlated modules can be used for beam-forming. Beam footprint and directivity can be adjusted with limitations. |

egy, however, results in discrete power control where only specific power levels can be obtained. Future MOWE designs might implement finer power control by utilizing programmable amplifiers inside each module. In fact, a more sophisticated TX/RX design, as detailed in Section 7.2.1, would provide MOWE with more flexibility and programmability, much like an SDO, but at the expense of higher cost and increased complexity. Section 6.3 presents an experiment demonstrating intelligent power control using MOWE. The experiment provides an example of SDO controlling its transmission power via machine learning, which gives the terminal cognitive abilities to function as CO. This is discussed in the next section.

One application for MOWE is acting as a tunable optical antenna where multiple parameters (e.g., directivity, sensitivity, and coverage, among others) can be controlled. Correlation factor, however, is important for such an antenna. Depending on the application, MIMO requires spatial un-correlation, while beam-forming requires spatial correlation. Correlation distance can be roughly controlled (e.g., halved or doubled) by switching modules on and off. Minimum correlation distance depends on many parameters, including optical resolution, array geometry, transmitter FoR, and receiver FoV, to name a few.

## 5.5. Cognitive Optics

"A cognitive radio is an SDR that is aware of its *environment*, *internal state*, and *location*, and autonomously adjusts its operations to achieve designated objectives" [69]. Joseph Mitola defines the functional components of an ideal cognitive radio (iCR), as described in Table 5.2. iCR is expected to sense both its environment (e.g., available spectrum, weather, motion, etc.) and its user (i.e., detecting user commands and gestures). Using MOWE, one can connect a vast array of sensors to the optical terminal via UART, I2C, SPI, and GPIO interfaces. The closed-loop, passive steering experiment presented in Section 6.2.4 demonstrates interfacing MOWE with an inertial measurement unit (IMU)−that contains a gyroscope and an accelerometer−via the I2C port. These sensors measure terminal motion intended for beam steering algorithms.

Cognitive abilities are considered the most defining characteristics for an iCR, along with its ability to run specific applications. Control, planning, and learning functions can be implemented on MOWE, as well, given that these algorithms are scaled down for small MCUs. Just as the iCR is expected to receive inputs from its surroundings, the radio is also expected to control its environment in one way or another. MOWE modules can control external devices and actuators via available interfaces (e.g., UART, I2C, SPI, GPIO, and PWM), as well as using intermediate drivers if needed. The misalignment testbed in Section 6.1 demonstrates using MOWE modules to control servo motors via PWM signals.

It should be noted that cognitive abilities are necessary in broadband RF communication and networking. It is not the case, though, for the traditional point-to-point optical wireless communication. However, with the advent of omnidirectional MOWE concept and design (multi-element, multi-user and mobile networking capabilities), cognition becomes applicable and necessary to segregate users, remove noise and adapt beam strength, among other applications.

**Table 5.2. Comparing Cognitive Radio and Cognitive Optics**

| CR Components | Details | Available currently in MOWE? | Implementation Details |
|---|---|---|---|
| **User sensory perception** | Interface includes haptic, acoustic, and video sensing and perception functions. | Yes | External sensors can be connected to the system via I2C, SPI, UART and GPIOs. |
| **Local environment sensors** | Location, temperature, accelerometer, compass, etc. | Yes | External sensors can be connected to the system via I2C, SPI, UART and GPIOs. |
| **System applications** | Media independent services like playing a network game. | Yes | Specific applications can be programmed in a local, central, or distributed fashion. |
| **SDR** | | Yes | See previous table. |
| **Cognition functions** | Symbol grounding for system control, planning, learning. | Yes | Can be implemented with algorithms running on the MCU. |
| **Local effector functions** | Speech synthesis, text, graphics, and multimedia displays. | Yes | External devices can be controlled by the system via I2C, SPI, UART and GPIOs. |

# Chapter 6: MOWE Demonstrations

In this chapter, a number of MOWE arrays and concepts that were introduced earlier are combined with sensors, actuators, and algorithms to build a collection of demonstrations covering a wide spectrum of topics. The purpose of these demonstrations is not to conduct comprehensive experiments or develop high-performance systems, but rather to show MOWE potentials and applicability for various scenarios.

In Section 6.1, a misalignment testbed built using MOWE modules, 3D-printing, and servo motors is explored. The testbed demonstrates optical beam detection, as well as closed-loop, real-time beam tracking. Active and passive beam steering are discussed in Section 6.2 with a survey of fine and coarse steering mechanisms. An active, closed-loop beam steering experiment that utilizes fine steering mirrors (FSMs) and an optimal linear quadratic controller (LQR) is presented. Then, MOWE-based passive steering is presented both in open-loop and closed-loop scenarios, utilizing feedback from an external inertial measurement unit (IMU). Finally, Section 6.3 features an intelligent optical terminal that utilizes machine learning to optimize transmission power given a particular noise environment.

## 6.1. Misalignment Testbed

The misalignment testbed consists of multiple 37-module, flat hexagonal arrays used as all-receiver, all-transmitter, or transceiver terminals. Each array is fitted with a 2-axis gimbal driven by two servo motors. The array and gimbal are linked together and affixed to an optical table via 3D-printed plastic holders and fixtures, which results in a complete terminal. The arrays are based on the streaming architecture detailed in Section 4.2 wherein a master module is responsible for synchronization and data

streaming in and out of the array. The master processes samples collected by other detector modules after each scan, and then forwards them to an external MATLAB-based PC software that analyzes and displays the measurements. The master is also responsible for switching on/off transmitter modules and controlling other array aspects (e.g., indicator LEDs and external sensors/actuators). Figure 6.1 illustrates the actual testbed setup. Multiple terminals can be used in the experiments, each running its own firmware and algorithms. Everything can be controlled and accessed

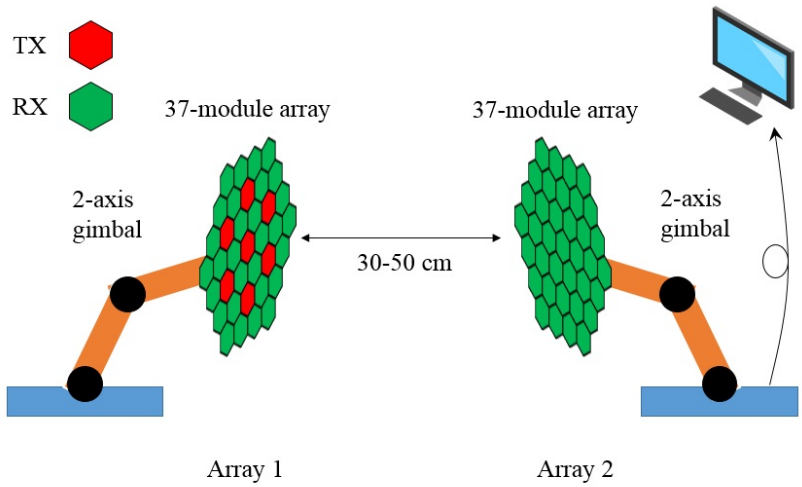


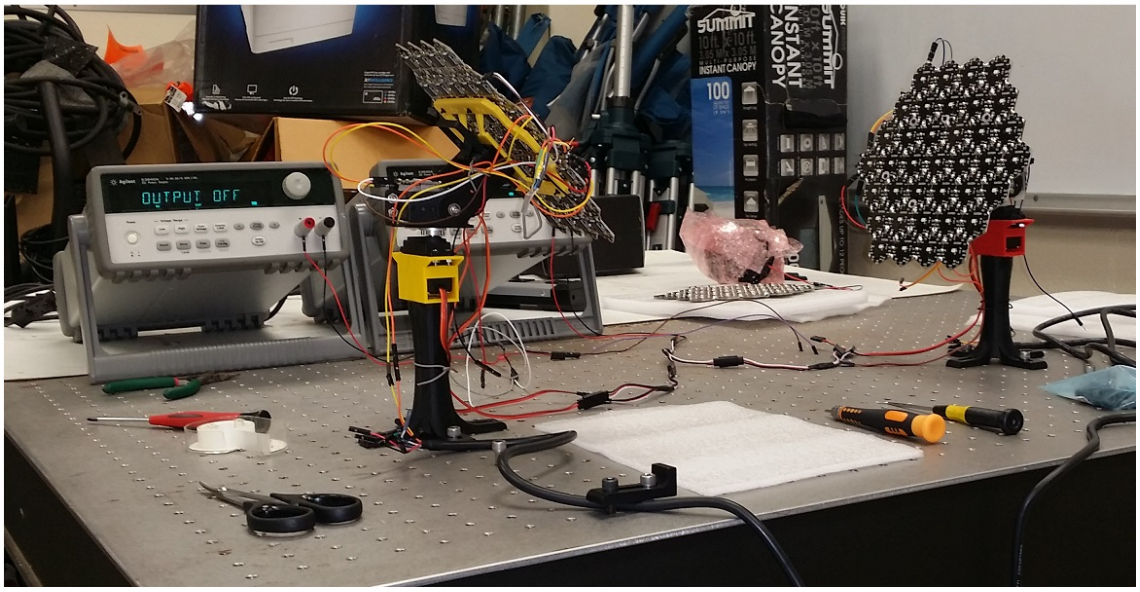


**Figure 6.1. Illustration and actual implementation of the misalignment testbed.**

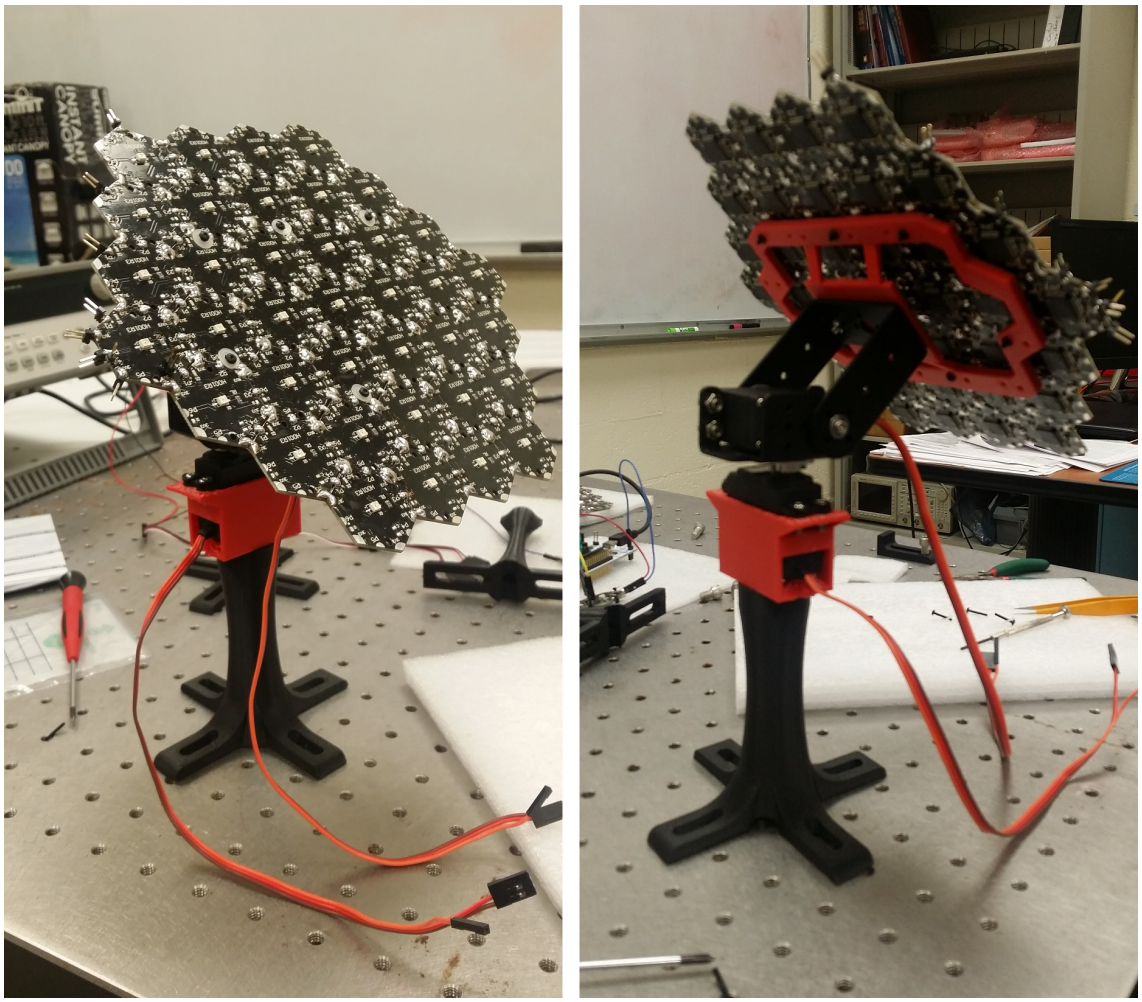

**Figure 6.2. An all-receiver terminal shown with its array, gimbal, plastic fixtures, and a four-legged optical table holder.**

from a software on PC. Note that the terminals are placed relatively close to each other since MOWE transmitter LEDs have a limited range.

An all-receiver terminal is shown in Figure 6.2, including its array, gimbal, and all fixtures. Gimbal servo motors are controlled using a separate MOWE module that performs as a servo controller by running a special firmware. In this way, the terminal is able to rotate about 120° in both azimuth and elevation directions. The master module commands the servo controller to position the array at particular azimuth/elevation angles or to run a pre-described misalignment profile, whether repetitive or random.

Figure 6.3 shows two snapshots photographed from Visualizations 6 [70] and 7 [71].

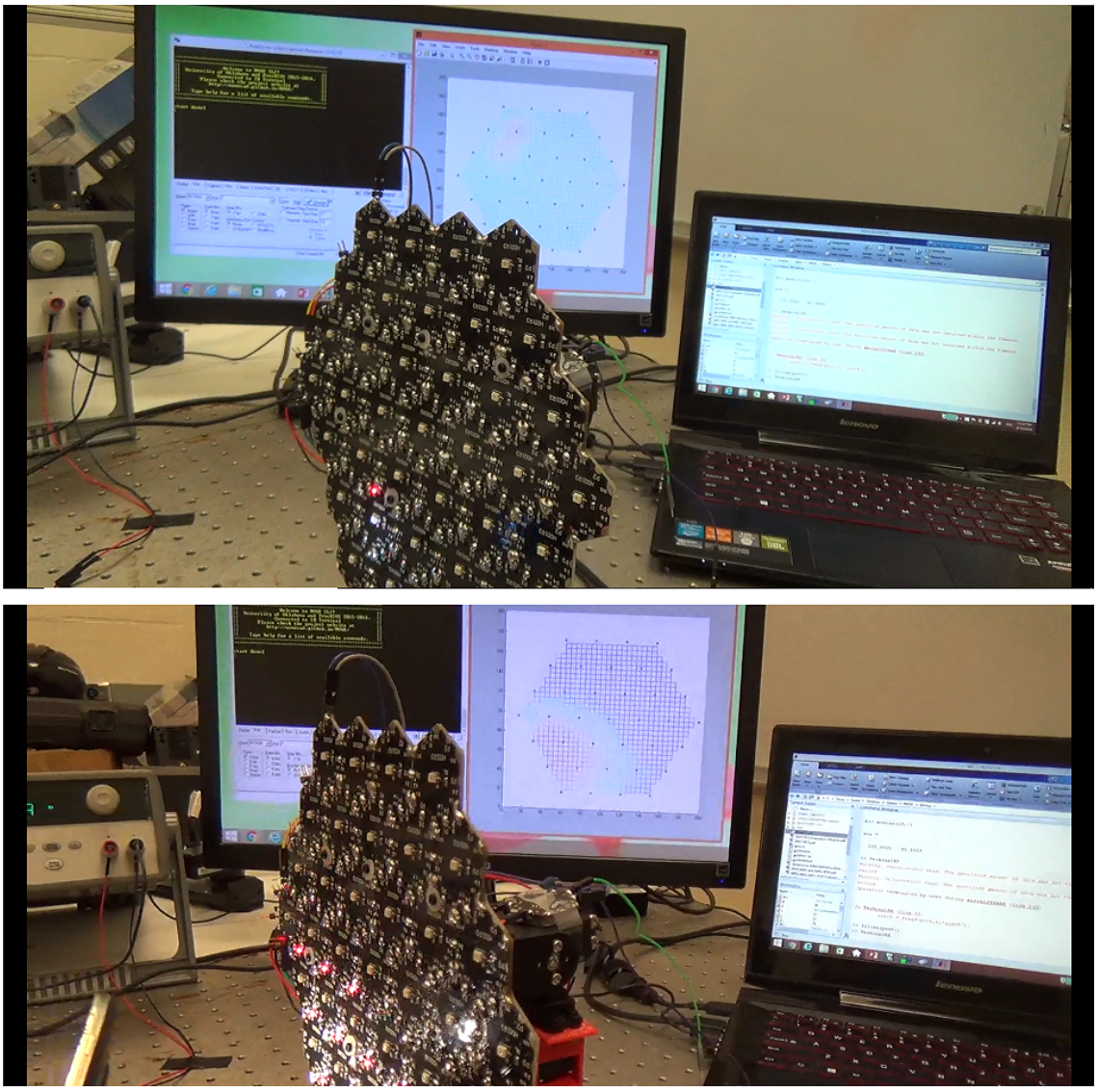

**Figure 6.3. Detecting and measuring light beams across multiple modules.**

The videos show a light beam covering a single module (up) and multiple modules (bottom) recorded in real-time. Module indicator LEDs are triggered automatically once received intensity crosses a particular threshold. Beams are also shown on a PC screen after being processed and analyzed by the software. Note that the arrays respond directly to beam movement and stream data in real-time. The MATLAB software, however, lags behind a bit due to surface interpolation processing delays.

### *Beam Tracking*

This experiment demonstrates real-time optical beam (user/noise source) tracking as presented in Visualization 8 [72]. The master module collects measurements and estimates beam footprint position at each scan. Position estimation is accomplished by calculating beam center-of-intensity COI (i.e., center-of-mass or weighted average), and then taking the distance error to array center:

$$X_{COI} = \frac{\sum_{i=1}^{37} I_i X_i}{\sum_{i=1}^{37} I_i}, \quad Y_{COI} = \frac{\sum_{i=1}^{37} I_i Y_i}{\sum_{i=1}^{37} I_i}, \tag{6.1}$$

and

$$\Delta X = X_{COI} - X_{arr}, \quad \Delta Y = Y_{COI} - Y_{arr}, \tag{6.2}$$

where $(X_{COI}, Y_{COI})$ represent beam COI Cartesian coordinates; $(X_{arr}, Y_{arr})$ is array center Cartesian coordinates; $(X_i, Y_i)$ is module $i$ Cartesian coordinates; $(\Delta X, \Delta Y)$ is the distance error; and $I_i$ is received intensity at module $i$. The appropriate azimuth ($\Psi$) and elevation ($\Theta$) angles for centering the beam on the array are then calculated as follows:

$$\Psi^\circ = \arctan(\Delta X, arm) \times \frac{180^\circ}{\pi}, \quad \Theta^\circ = \arctan(\Delta Y, arm) \times \frac{180^\circ}{\pi}, \tag{6.3}$$

where $arm$ is the distance from array center to terminal center-of-rotation (COR). A corrective action can be applied immediately in a single step by commanding the servo motors to move to calculated $(\Psi, \Theta)$ angles, thus, not requiring a controller. (Servo motors already employ a controller and a feedback loop.)

## 6.2. Optical Beam Steering

### *6.2.1 Introduction*

Gyro-stabilized, two-axis mechanical gimbals are the most common coarse alignment platforms, typically utilizing two brushless servo motors for tip/tilt (elevation/azimuth) movement. The gimbal is actively stabilized in a closed-loop fashion using either a MEMS-based IMU [73], especially a gyroscope, or an optical-fiber-based IMU [74]. With accuracies up to $100\mu rad$ or less, and a vast market for surveillance and aerial photography, gyro-stabilized mechanical gimbals are the most developed and trusted coarse alignment technology. They suffer, however, from bandwidth limitations. Typical update rates are about $200-300Hz$ limited by the mechanical drive system (whether geared or gearless). Hilkert [75] provides an excellent tutorial about inertially-stabilized platform concepts and technologies.

Other technologies contending for coarse alignment platforms, especially in high bandwidth regime, include spatially distributed optical nodes with electrical connections [30], all-optical tracking and steering using fiber bundles [9,24,28,37], biologically-inspired optics (e.g., elastomeric microlens arrays [18], Biomimetic Gradient Index (GRIN) Lenses [21], and tunable microdoublet lenses [19]). Although some of these technologies are only suitable for tracking, they are highly competitive in terms of lifetime, resolution, bandwidth, and cost. All are still, however, in the lab-prototype stage. Table 6.1 provides a rough comparison of some coarse alignment concepts and technologies based on their bandwidth, alignment accuracy, and technology-readiness level.

**Table 6.1. Comparison of Coarse Alignment Mechanisms**

| Technology | Readiness Level | Concepts | Alignment Accuracy ($\mu rad$) | Bandwidth ($Hz$) |
|---|---|---|---|---|
| Gyro-stabilized mechanical gimbals | Ready and tested | [73, 74] | 50 [1] – 200 [2] | 200 - 300 [2] |
| Fiber bundles | Lab prototype. Needs to increase coupling efficiency. Highest throughput. | Free-space combiner [22] | $\sim 65$ [3] | $20MHz$ [4] |
| Electrically-connected spatially distributed optical nodes | Lab prototype. Technology is ready but no major projects. Low throughput (O/E). | [30, 40] | $< 50$ [5] | $1KHz$ – $1GHz$ [6] |
| Bio-inspired optics | Lab prototype. Tracking; no clear steering capability. | Tunable doublet lens array [19] | $< 50$ [7] | $20MHz$ [4,8] |
| | | Elastomeric micro lens array [18] | $11.04°$ [2] | $20MHz$ [4,8] |
| | | GRIN [21] | NA [9] | $20MHz$ [4,8] |

[1] Special purpose platforms.
[2] Reported in literature.
[3] Approximation based on fiber cladding (dead areas) and $30cm$ fiber-to-lens distance.
[4] Based on typical switching speed of optical fiber switches [59].
[5] Assuming dense packaging. Actual numbers depend on LED divergence, PD angle of half sensitivity, and density factor.
[6] Depends mainly on electrical bus speed.
[7] Polymer-based receivers can be packaged much denser than regular silicon-based ones.
[8] Assuming received light is coupled into optical fibers.
[9] GRIN corrected lens have the highest resolution (i.e., no dead areas).

**Table 6.2. Comparison of Fine Alignment Mechanisms**

| Technology | Readiness Level | Concepts | Alignment Accuracy ($\mu rad$) | Total FoV (°) | Bandwidth ($Hz$) |
|---|---|---|---|---|---|
| Fast steering mirrors | Ready and tested. Easy to assemble. Small and lightweight. | MEMS [76] | $< 0.5$ [1,2] | $< 10°$ [1] | 1–10$KHz$ [1] |
| | | Acoustic actuation[3] | $\sim 1600$ [1] | $48°$ [1,4] | 0.5 – 80$MHz$ [1] |
| Micro mirrors | Ready and tested for interconnects and VCSEL-to-fiber [77]. | Thermal actuation [78] | 1.4 [1,2] | $4°$ [1] | NA |
| | | Electromagnetic actuation [79] | 14 [5] | $4.8°-18.4°$[1] | Several $KHz$ [1] |
| | | Piezoelectric actuation [80] | $\sim 80$ [5] | $< 10°$ [1] | 3.5$KHz$ [1] |
| Fiber bundles | Lab prototype. Needs to increase coupling efficiency. Highest throughput[6]. | Free-space combiner [22] | $\sim 65$ [7] | $\sim 4°$ [1,8] | 20$MHz$ [9] |
| | | Micro lens array with a piezoelectric transducer. [81] | $\sim 65$ [7] | $\sim 10°$ [1,8] | 1000 [1] |
| Modulating Retro-reflectors | Ready and tested. Small and lightweight. | Corner Cube, Cat's Eye [82–85] | $\sim 150$ [1] | 12.5°-40° [1] | 180$KHz$ [1], 10 – 25$MHz$ [10] |

[1]Reported in the literature.
[2]Depends mainly on driver resolution.
[3]Acousto-optics have higher bandwidth but are usually bigger and consume more power than other FSMs.
[4]Deflection angle range for a single element.
[5]Reported in the literature and depends mainly on driver resolution. This value assumes a 14-bit DAC.
[6]Fibers provide poor beam steering unless controlled by some mechanism
[7]Approximation based on fiber cladding (i.e., dead areas) and 30$cm$ fiber-to-lens distance.
[8]In theory, fibers can be geometrically distributed to cover a full 360° range
[9]Based on typical switching speed of optical fiber switches [59]
[10]Reported in the literature using a Multiple Quantum Well (MQW) modulator.

Several technologies contend for fine optical steering and tracking. Most common are fast steering mirrors (FSMs) [76]. These small reflecting mirrors can be tilted on two axes using various mechanisms. FSMs usually measure less than $10mm \times 10mm$. MEMS-based FSMs are compact, support high bandwidth, and are easy to manufacture and assemble [86,87]. Acousto-optic FSMs serve as another platform [88,89]. Micro mirrors are micro-sized mirrors, usually with sub-millimeter dimensions, and can be controlled by various mechanisms. Typically these mirrors are used for VCSEL-to-fiber [77] coupling and optical interconnects [90]. MEMS-based micro-mirrors with various actuation mechanisms are also being evaluated (e.g., electromagnetic [79], thermal [78], and piezoelectric actuation [80]). Modulating retro-reflectors are also popular candidates for fine alignment platforms [82,83]. This technology is lightweight and covers a large FoV of $20° - 40°$ per element. Arrays of retro-reflectors can be assembled to expand total FoV [84, 85].

New techniques are also garnering attention (e.g., fine steering with VCSEL arrays [91], steering and tracking with free-space-coupled fiber bundles [22, 26], and micro-nudging of fibers with piezoelectric transducers [81]). Table 6.2 summarizes and compares the various contending fine alignment technologies relative to accuracy, bandwidth, total FoV, and readiness level.

### *6.2.2 Optimal Active Steering using FSMs*

This section presents modeling and optimal control of an active steering mechanism for a fiber-coupling system. The system utilizes FSM and multiple sensors to couple laser beams from satellites or aircrafts into a single- or multi-mode fiber. The study was performed during an internship at the German Aerospace Center (DLR).

A typical fiber coupling system is shown in Figure 6.4 and is composed of a two-stage assembly. For coarse alignment, the entire system is mounted on steerable mechanical gimbals. With this, the system can point and track moving targets in an entire hemisphere surrounding the ground station. Certainly, the disadvantages are its modest pointing accuracy of several $100\mu rad$, as well as its low bandwidth limitation. To enhance system performance, the platform is expanded using a fine

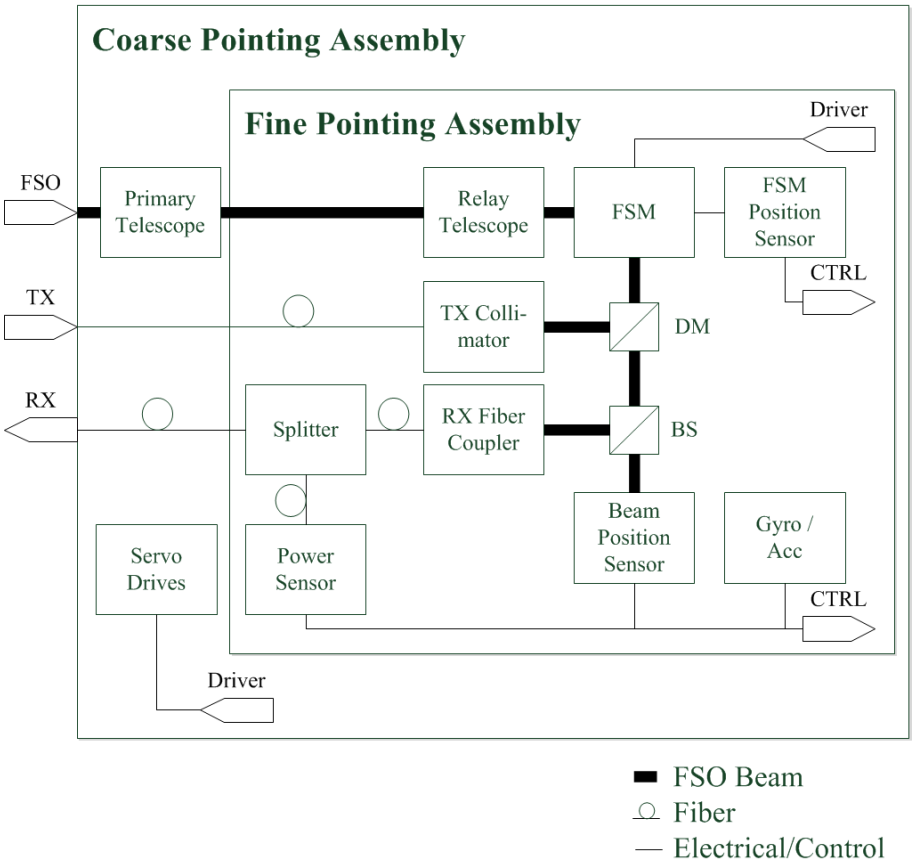


**Figure 6.4. Block diagram of a fiber coupling system.**

pointing assembly (FPA) based on a controlled beam reflection from a MEMS-based FSM.

Using the primary telescope, the incoming light is collimated to a certain diameter, depending on the focal lengths of the telescope mirrors or lenses. A secondary relay telescope is utilized to encompass an image of the entrance pupil on the FSM in a 45° angle within a diameter of only a few millimeters. This telescope performs as the interface between a given primary telescope and the fiber coupling system. As such, the main parameters that define the optical design are the diameter and the angular range of the FSM. Afterwards, a beam splitter reflects $\sim 90\%$ of the light on a fiber coupling assembly consisting of an aspheric lens and a fiber port that is adjustable in two rotational and three translational axes. The remaining $\sim 10\%$ is directed to a beam position sensor consisting of a lens that focuses the beam on a four quadrant InGaAs diode. The focal length of this last lens depends on the resolution required

from the sensor. For effective performance, a precise alignment between sensor and coupler is essential.

The MEMS FSM requires a high voltage driver. To achieve high resolution, this system uses a 16-bit DAC (effective 14 bits assumed). Given these parameters and a field-of-regard (FoR) of $\pm 22.7 mrad$, the FSM can internally resolve $2.75 \mu rad/bit$ with a bandwidth of $\sim 500 Hz$.

The fiber coupling system must handle several sources of interference. Atmospheric effects are not only problematic for data transmission but also for system control. Besides input angle displacement, input power scintillation resulting from the atmosphere is challenging. Sensors with high resolution and high dynamic range are necessary. The primary feedback sensor in the system consists of a lens that focuses the input beam on a four-quadrant diode. This sensor measures the input angle of the FSO beam, which can be used to control the FSM for centering the beam on the sensor and the fiber port. A power sensor measures the coupled power in

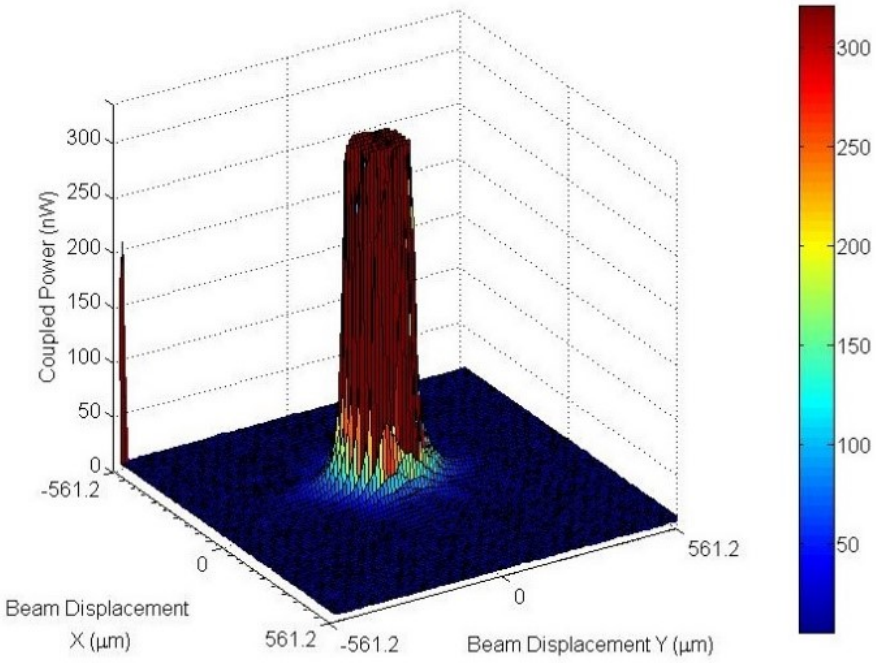


**Figure 6.5. A full scan test shows power coupled into the fiber.**

the fiber. This measurement can be used for either an initial calibration or directly integrated into the control loop. Combining beam position sensor with power sensor allows the controller to optimize power coupling. This is preferred over centering the beam, as centering might not yield optimum coupling due to alignment tolerances in the setup.

The CPA's mechanical gimbals movement and any external shock effects are measured using a 6-axis gyro/accelerometer sensor. Figure 6.5 shows fiber-coupled optical power measurements in a full-range FSM scan. Scan range covers about 0.5mm vertical and horizontal displacements in both directions. Fiber core radius measures $9\mu m$, and maximum coupled power is approximately $300nW$.

### System Modeling

A typical fiber coupling system can be modeled as a standard, closed-loop system with inputs including controlled signals, such as the FSM voltage, as well as disturbance (e.g., displaced input beam and mechanical vibrations). System output is measured in terms of output beam displacement or signal power coupled into the fiber. The controller seeks to regulate system output (i.e., maximize coupled power) and generate a control signal following a set value or an optimization function. The controller must measure (or estimate) the disturbance to achieve this goal.

The system state space equations can be written as follows:

$$\begin{bmatrix} \dot{\theta}_{mx} \\ \ddot{\theta}_{mx} \\ \dot{\theta}_{my} \\ \ddot{\theta}_{my} \end{bmatrix} = \begin{bmatrix} 0 & 1 & 0 & 0 \\ 0 & 0 & 0 & 0 \\ 0 & 0 & 0 & 1 \\ 0 & 0 & 0 & 0 \end{bmatrix} \times \begin{bmatrix} \theta_{mx} \\ \dot{\theta}_{mx} \\ \theta_{my} \\ \dot{\theta}_{my} \end{bmatrix} + 2 \begin{bmatrix} K_x & 0 & 0 & 0 \\ 0 & K_x & 0 & 0 \\ 0 & 0 & K_y & 0 \\ 0 & 0 & 0 & K_y \end{bmatrix} \times \begin{bmatrix} v_{mx} \\ \dot{v}_{mx} \\ v_{my} \\ \dot{v}_{my} \end{bmatrix}$$

$$+\begin{bmatrix} 1 & 0 & 1 & 0 & 0 & 0 & 0 & 0 \\ 0 & 1 & 0 & 1 & 0 & 0 & 0 & 0 \\ 0 & 0 & 0 & 0 & 1 & 0 & 1 & 0 \\ 0 & 0 & 0 & 0 & 0 & 1 & 0 & 1 \end{bmatrix} \times \begin{bmatrix} \theta_{Nx} & \dot{\theta}_{Nx} & \theta_{Bx} & \dot{\theta}_{Bx} & \theta_{Ny} & \dot{\theta}_{Ny} & \theta_{By} & \dot{\theta}_{By} \end{bmatrix}^T, \tag{6.4}$$

$$FCI(t) = \begin{bmatrix} K_{FC} & 0 & K_{FC} & 0 \end{bmatrix} \times \begin{bmatrix} \theta_{mx} \\ \dot{\theta}_{mx} \\ \theta_{my} \\ \dot{\theta}_{my} \end{bmatrix}, \tag{6.5}$$

where $\theta_{mx}$ and $\theta_{my}$ are the optical displacement angles of the output laser beam; $\theta_{Bx}$ and $\theta_{By}$ are the optical displacement angles of the incoming laser beam due to turbulence; $\theta_{Nx}$ and $\theta_{Ny}$ are used to model any mechanical disturbance caused by the CPA; $v_{mx}$ and $v_{my}$ are input voltages applied to the FSM; $K_x$ and $K_y$ are constants or functions describing FSM response to input voltage; and $K_{FC}$ is a linear coefficient linking the Fiber Coupling Index (FCI) with displacement angles. Power coupled into the fiber is considered dependent on displacement angle only. FCI takes a value of 0 when the beam is fully coupled into the fiber and a value of $\pm 1$ when coupling is not possible. The constant $K_{FC} = 1/(2\theta_{max})$ is calculated based on maximum displacement angle ($\theta_{max}$), which moves the beam completely outside the fiber core−assuming the relationship between beam displacement and coupled power is linear.

The MEMS FSM, however, is a second order system with an inherent delay that might not be negligible for fast input signals. Thus, constants $K_x$ and $K_y$ must be replaced with time-varying functions. A single-axis time response for a MEMS FSM is shown in Figure 6.6 and can be described by the following transfer function:

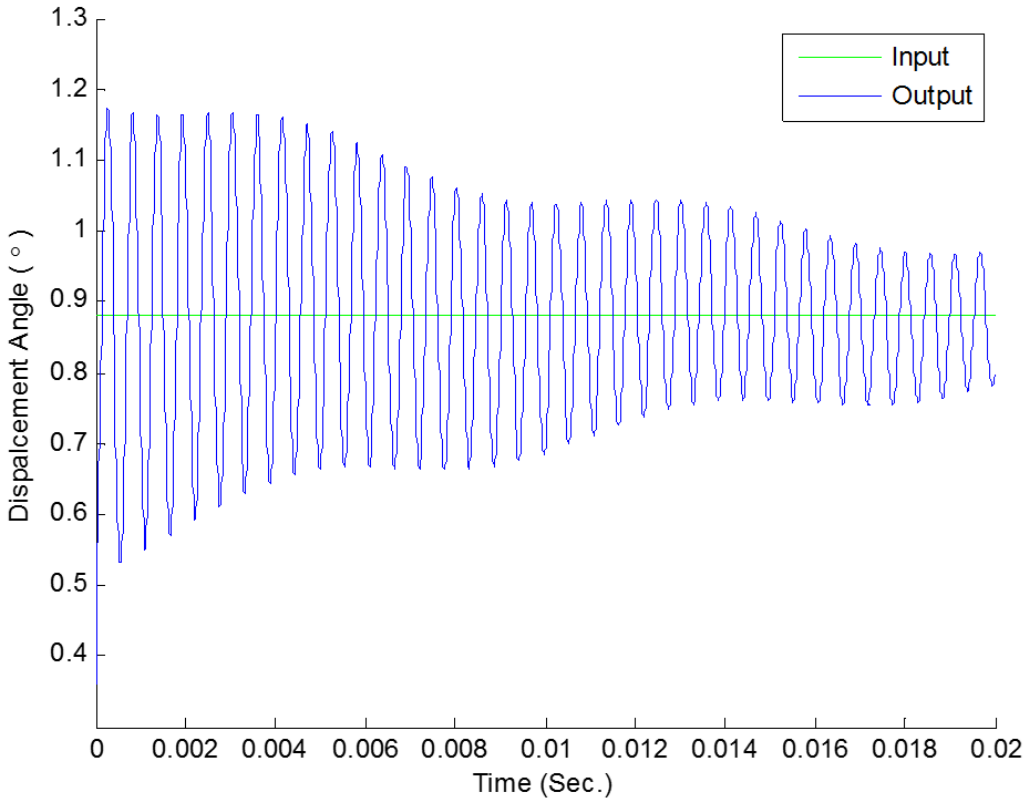


**Figure 6.6. Single-axis time response of a MEMS FSM.**

$$G(s) = K_{FSM} \cdot \frac{2.743 \cdot 10^{-15} s^4 + 1.525 \cdot 10^{-11} s^3 + 1.826 \cdot 10^{-6} s^2 + 1.417 \cdot 10^{-4} s + 1}{1.524 \cdot 10^{-19} s^5 + 1.527 \cdot 10^{-14} s^4 + 2.269 \cdot 10^{-11} s^3 + 1.969 \cdot 10^{-06} s^2 + 1.542 \cdot 10^{-4} s + 1}, \tag{6.6}$$

where $K_{FSM}$ is the single-axis steady-state gain.

### Finite-horizon Linear Quadratic Regulator

The Linear Quadratic Regulator (LQR) seeks to regulate the states (i.e., drive them to zero) while minimizing the performance index. For a finite-horizon LQR, performance

index (PI) is given by:

$$J(t_0) = \frac{1}{2}\int_{i=0}^{\infty}\Big(x'(t)Qx(t) + u'(t)Ru(t)\Big)dt, \tag{6.7}$$

where $Q$ and $R$ are weight factors for the states and the inputs, respectively. Conditions are $Q \geq 0$ and $R > 0$. Assuming identical FSM axes and no mutual coupling, the PI for a single axis can be expressed as:

$$J(t_0) = \frac{1}{2}\int_{i=0}^{\infty}\Big(q_1\theta_m^2(t) + q_2\dot{\theta}_m^2(t) + r_1 v_m^2(t) + r_2\dot{v}_m^2(t)\Big)dt, \tag{6.8}$$

where $q_1, q_2$ are factors weighing the output beam displacement angle and its rate of change, respectively; and $r_1, r_2$ are factors weighing the mirror voltage (i.e., mirror angle) and its rate of change, respectively. The PI here aims to regulate the output displacement angle (i.e., center the beam on the fiber) and minimize voltage signals applied to the mirror, minimizing noise and power consumption. Other weights can be included in the PI as well (e.g., weight for FCI) for regulating FCI instead of output displacement angles (i.e., maximizing coupled power instead of centering the beam).

Solving the arithmetic Riccati equation (ARE) offline yields the optimal gain $K_{opt}$:

$$0 = A'S + SA - SBR^{-1}B'S + Q, \tag{6.9}$$

$$K_{opt} = R^{-1}B'S = \begin{bmatrix} \frac{2s_1K_{FSM}}{r_1} & \frac{2s_2K_{FSM}}{r_1} \\ \frac{2s_2K_{FSM}}{r_2} & \frac{2s_3K_{FSM}}{r_2} \end{bmatrix}, \tag{6.10}$$

and the single-axis control signal is:

$$u(t) = -K_{opt}\cdot x(t) = -K_{opt}\begin{bmatrix} \theta_m(t) \\ \dot{\theta}_m(t) \end{bmatrix}. \tag{6.11}$$

The closed-loop, optimal, linear controller was simulated in MATLAB along with the second-order, nonlinear FSM model shown in Figure 6.6. The input beam is simulated using a band-limited white noise signal with RMS of $40\mu rad$ and band-

width of $100Hz$. Mechanical disturbance resulting from coarse alignment platform or mechanical structure is simulated as a band-limited white noise, as well, but with a much lower bandwidth of $5Hz$ and higher RMS of $200\mu rad$ (i.e., typical error for gyro-stabilized mechanical gimbals). 15-bit quantizers running at $10kHz$ sampling rate were added to the noise variables (i.e., input beam displacement and mechanical disturbance) to simulate the implemented ADCs in the actual system. A saturation filter is added to the controller to limit output voltage to $130V-$the maximum safe voltage for operating this FSM. The output voltage is also applied via 14-bit quantizer, simulating the use of DAC at $10kHz$ sampling rate. Although the controller is designed for linear systems, it handled the nonlinear FSM well, as shown in Figure 6.7. The analysis showed two stable (i.e., real) poles at -146287 and -4626, rendering the closed-loop system stable. Input, noise, and output displacement angles are shown in Figure 6.8, accordingly.

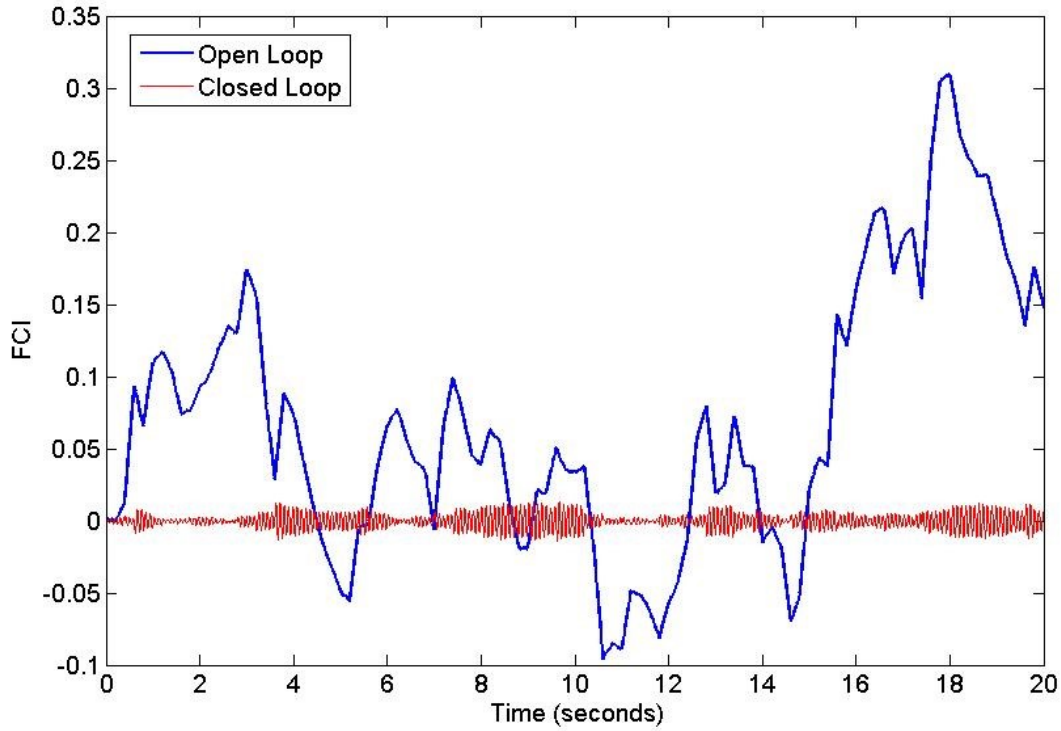


**Figure 6.7. Fiber coupling index in the open- and closed-loop simulation.**

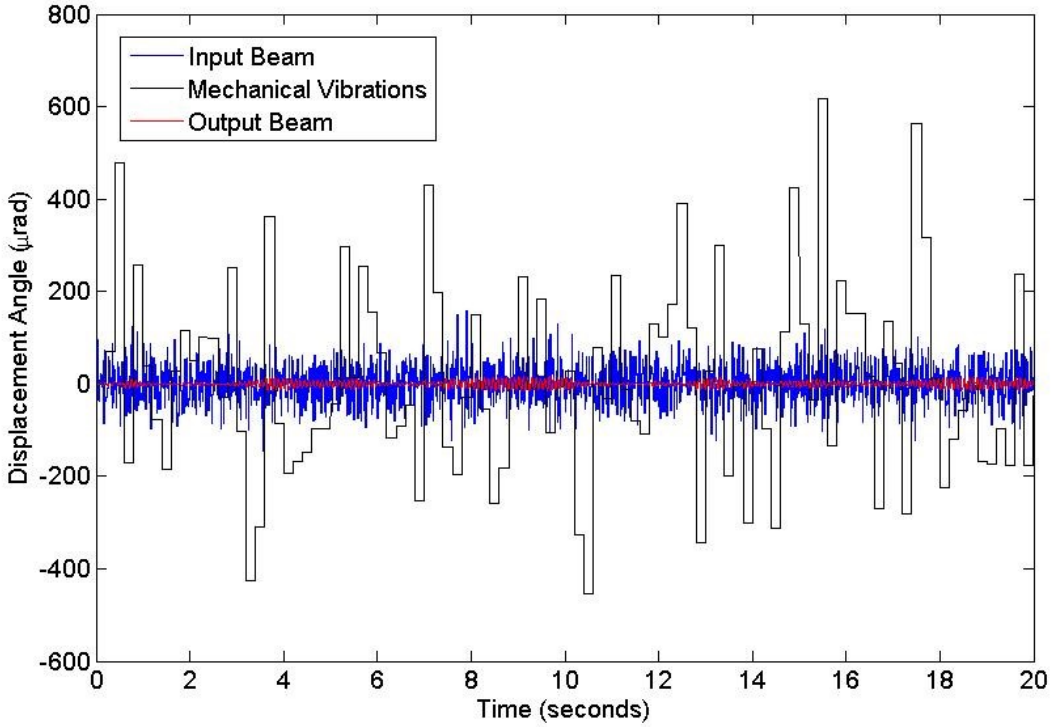


**Figure 6.8. Displacement angles of input and output beams.**

### *6.2.3 Open-loop Passive Steering*

Passive beam steering−one in which no mechanical device is involved−could be a prime application for MOWE. In this experiment, six transmitter modules (five hexagons and one pentagon) were assembled in a spherical dome shape, as shown in Figure 6.9. The experiment demonstrates the use of multiple DMA streams for streaming data in a SIMO configuration. The signal was streamed into the array by module A at an average data rate of $100kbps$. Next, the signal was transferred to module B, which transferred two exact copies of the same signal to modules C and D. Doing so rendered module B as a *switch*. All four modules transmited the same signal using their LEDs at $850nm$. This design leveraged MOWE spatial diversity to increase terminal FoR and transmission power, as well as steer the signal at predefined angles to maintain communication while tracking the mobile user.

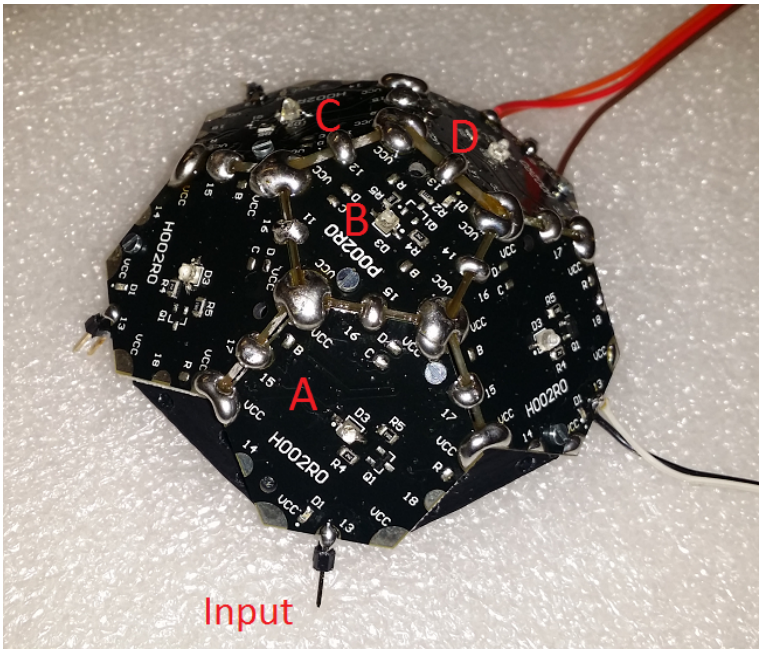


**Figure 6.9. Dome-shaped transmitter array.**

The measured shift delay for these data streams was approximately $11\mu sec$ per hop (See Figure 6.10), which can be compensated in firmware assuming that two different transmitters are required to be in precise synchronization. Timing error between duplicate streams inside a *switch* module was approximately $0.5\mu sec$.

Figure 6.11 shows beam steering behavior using switch module B. In this example, module B is streaming received data from module A and forwarding the data to either modules C or D. The dome shape, which was based on a truncated icosahedron, resulted in a 138.19° tilt angle between any two adjacent hexagons and a 142.62° tilt angle between the pentagon and any hexagon. This translates into steering angles of $\pm 37.38^o$ when switching from a pentagon to a hexagon and vice versa; and $\pm 41.81^o$ when switching between two adjacent hexagons. The terminal could potentially cover a large FoR by dynamically steering its beam. The beam in this experiment could be steered between two different modules in about $25\mu sec$ (i.e., a steering rate of $40kHz$). Steering rates of over $100kHz$ were recorded in experiments. Visualization 9 [92] demonstrates passive beam steering in a transceiver terminal in the MOWE misalignment testbed.

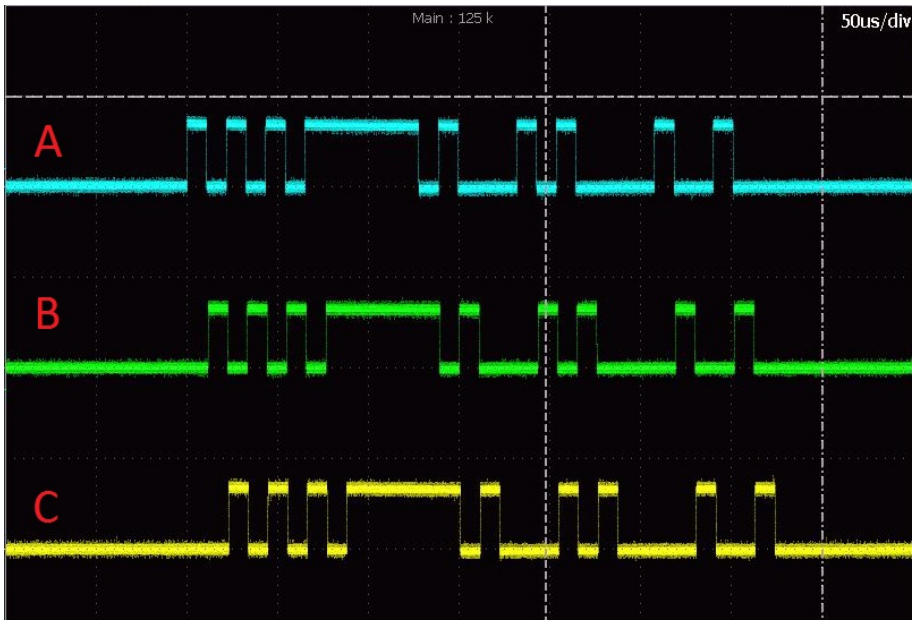


**Figure 6.10. Data transmission using three transmitter modules (A, B & C) with two hops. Shift delay is about $11\mu sec$ per hop.**

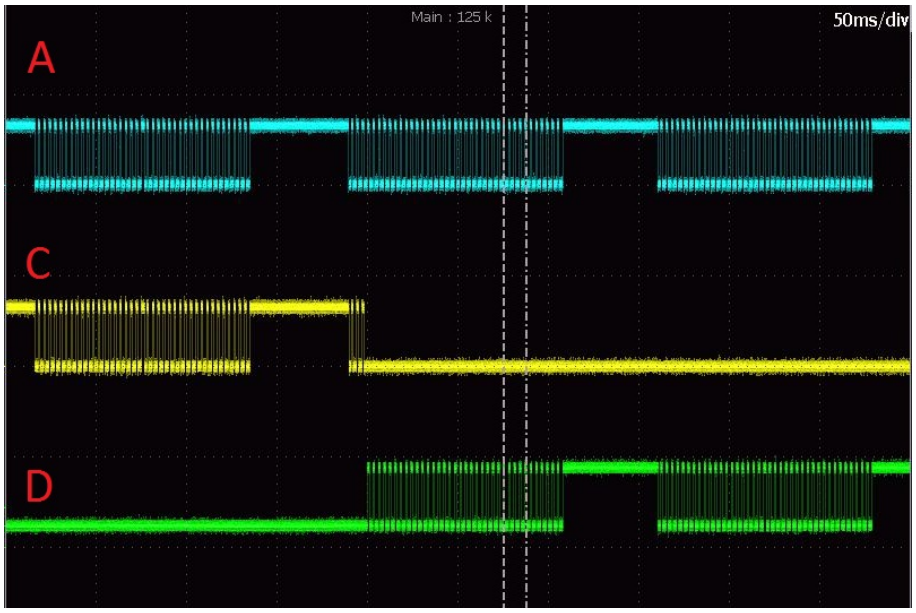


**Figure 6.11. Passive beam steering using a switch module. Data stream originating from module A is switched from module C to module D by the *switch* module B.**

### *6.2.4 IMU-aided, Closed-loop Passive Steering*

A transceiver terminal consisting of seven transmitter and 30 receiver modules was constructed for this experiment to demonstrate rudimentary closed-loop passive beam steering. The terminal, part of the misalignment testbed, was commanded to pan and tilt in a random pattern, emulating an unstable platform. These attitude perturbations were captured by an inertial measurement unit (IMU) consisting of a 3-axis gyroscope and a 3-axis accelerometer, and then fed to the regulator that steers the beam and tries to center it on the other (stable) terminal. No feedback was provided from the stable terminal to the unstable one. The experiment is shown in Visualization 10 [93].

IMU sensor MPU-6050 [94] was configured to generate measurements at about $4.3Hz$ and 16-bit per axis. Both gyroscope and accelerometer data were filtered and processed to estimate azimuth and elevation angles. A complementary filter was then used to fuse angle estimations from both sensors into a single output. This step is necessary since the gyroscope is notorious for its long-term drift, and the accelerometer is very sensitive to short-term disturbance. Fusing both estimations together will compensate for these errors. However, since gyroscope drift tends to get increasingly large overtime without calibration, the controller relied heavily on accelerometer estimations, which made the system a little bit sluggish. The attitude estimation algorithm inspired from [95] is explained in the block diagram in Figure 6.12.

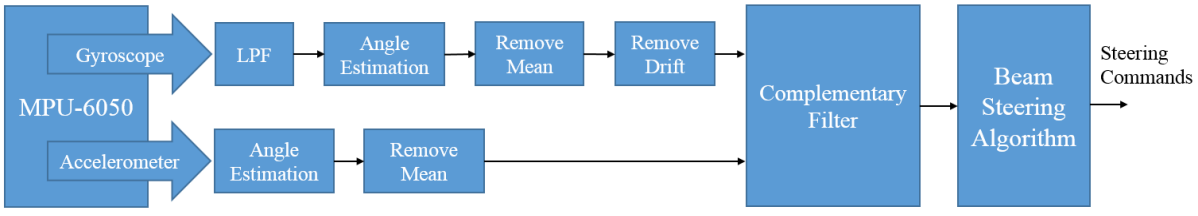


**Figure 6.12. Block diagram of attitude estimation and beam steering algorithm.**

### 6.3. Intelligent Power Control

This experiment combined multiple ideas and concepts from those described in previous chapters and provided a demonstration for basic SDO and CO capabilities. A transceiver array, consisting of seven transmitters and 30 receivers, was subjected to varying noise levels from multiple angles, using the noise generator (an all-transmitter, 37-module array). The transceiver terminal mimics an SDO with adaptive power control. Its transmission power can be controlled with seven power levels (1TX, 2TX, 3TX, etc.) The terminal is continually scanning background noise and must intelligently decide on optimum TX power level for achieving a minimum signal-to-noise (SNR) ratio while consuming the least amount of power.

Figure 6.13 shows the experimental setup with the noise generator on the left and the transceiver terminal on the right. Noise intensity was varied up and down between 14 power levels representing 14 hours of sunlight each day from 5AM to 6PM. For experiment purposes, sunlight noise variation is assumed to match these power levels throughout the day. Figure 6.13 shows left to right three noise snapshots from 8AM, 12PM, and 3PM, respectively. Note that the indicator LEDs are used to show the status of IR LEDs.

Background noise was scanned at $50Hz$. Each noise level in the experiments (i.e., representing a daylight hour) lasted for one second making each experiment about 16-20−second long. Experiments were repeated for 16 different orientations, listed in Table 6.3. (The noise source was moved around.) This yields $14 \times 16 = 224$ data records. At each new orientation, the terminals were first aligned to each other, and then the experiment commenced. Figure 6.14 plots received intensity at the 30 receiver modules in the transceiver terminal when both azimuth and elevation angles were zero. The figure also shows 14 vertical lines depicting the 14 sunlight hours in which intensity was sampled.

Each data record consists of the following information: total noise mean, total noise median, total noise variance, regional noise mean inside regions one to seven[1],

[1]Each region consists of the six receivers surrounding a given transmitter.

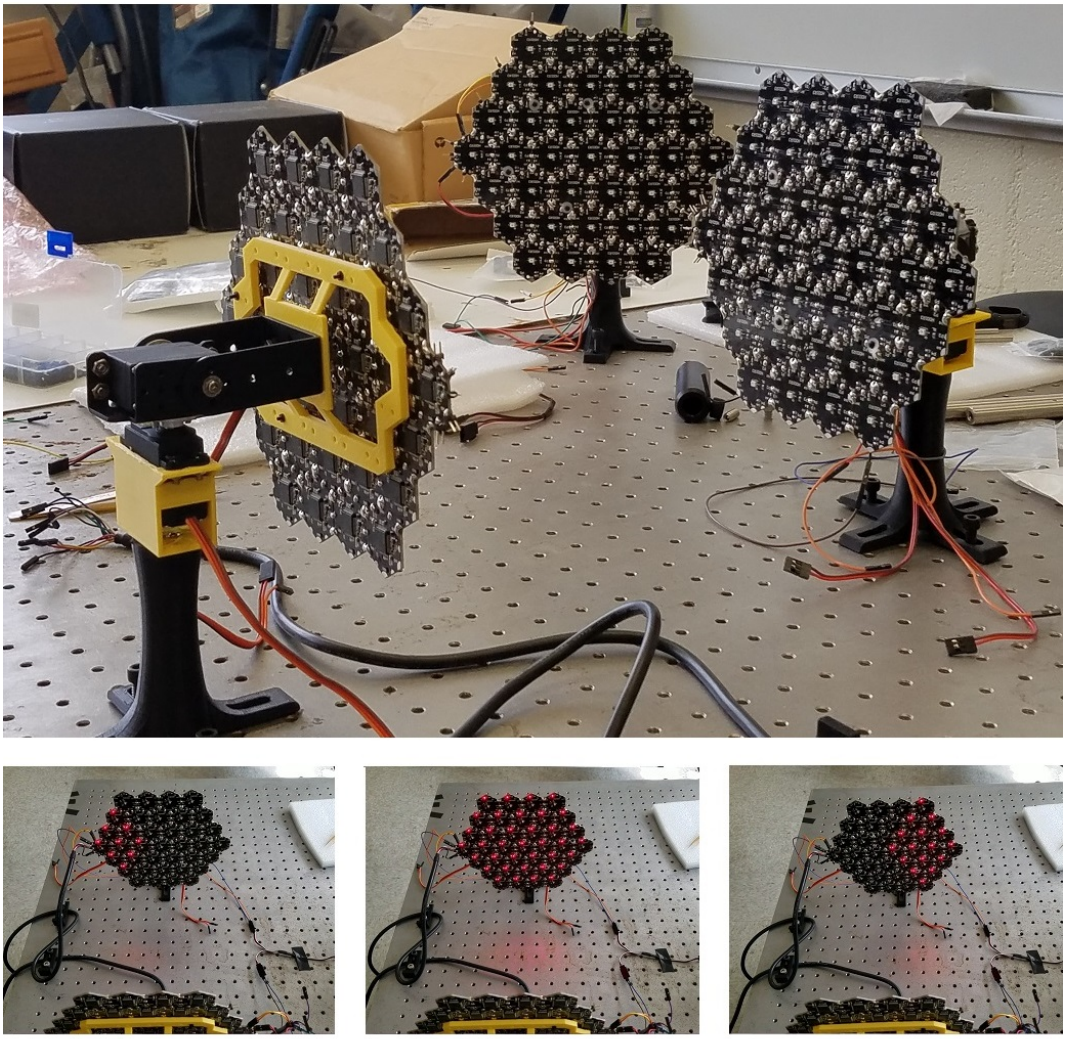

**Figure 6.13. The intelligent power control experiment. Top: Experimental setup at $(0°, 0°)$ orientation. Bottom: Snapshots from the noise generator.**

array minimum noise, array maximum noise, ID of module with minimum noise, ID of module with maximum noise, and time of day (5AM to 6PM). The 224 records, along with expert-set optimum power levels, were fed, offline, into a machine learning algorithm (a binary decision tree) to learn their patterns and build an intelligent classifier. The classifier would then be implemented on the master module to take in new records and deduce the appropriate power level, thus making the terminal cognitive. A minimum SNR ratio of $1dB$ was assumed for easy implementation. This figure does not represent, however, a good communication link.

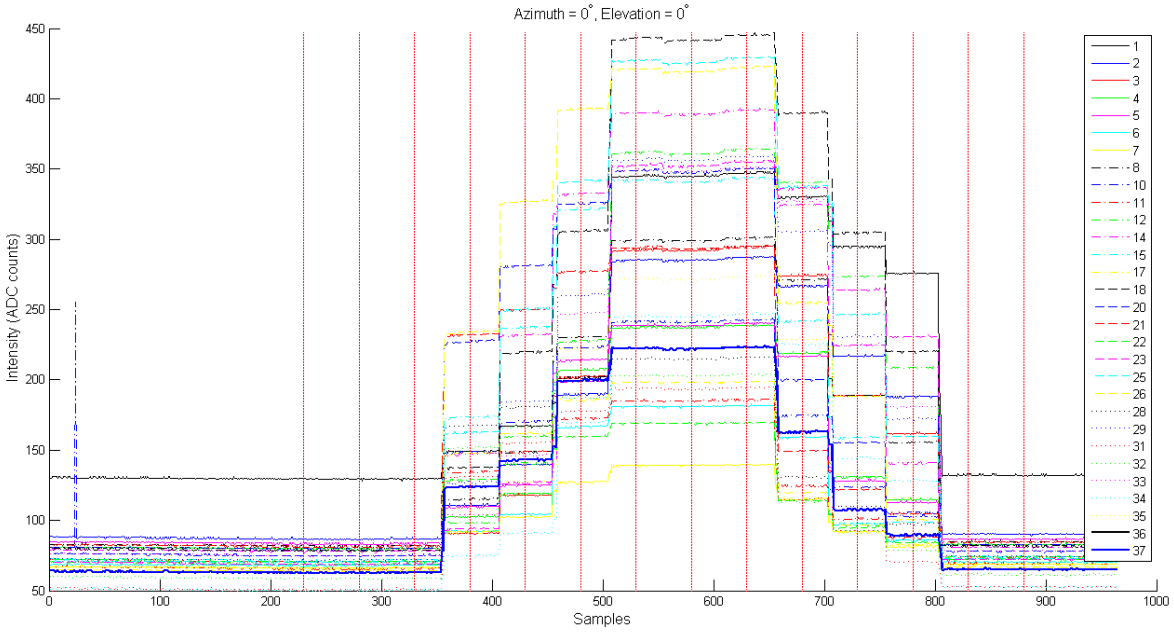


**Figure 6.14. Received optical intensity at receiver modules at $(0°, 0°)$ orientation.**

**Table 6.3. Azimuth and Elevation Angles in the Intelligent Power Control Experiment (Noise source with respect to intelligent terminal.)**

| Orientation | Azimuth (°) | Elevation (°) |
|---|---|---|
| 1 | 0 | 0 |
| 2 | 20 | 0 |
| 3 | 28.6 | 0 |
| 4 | 42.3 | 0 |
| 5 | 56 | 0 |
| 6 | 0 | 10.3 |
| 7 | 22 | 10.3 |
| 8 | 28.6 | 10.3 |
| 9 | 45 | 10.3 |
| 10 | 0 | 20 |
| 11 | 15 | 20 |
| 12 | 32.5 | 20 |
| 13 | 45 | 20 |
| 14 | 0 | 32.5 |
| 15 | 20 | 32.5 |
| 16 | 42 | 32.5 |


**Figure 6.15. Confusion matrix for the binary decision tree classifier. Classes one through seven represent transmitter power level.**

A medium-size, binary decision tree was trained on the data using MATLAB Classification Learner tool. A 10-fold cross-validation yielded 96.4% classification accuracy. Figure 6.15 shows the confusion matrix with true positive rates and false negative rates. The figure clearly shows that the classifier performed extremely well. Note that the transceiver maintained minimum SNR during all power levels except level seven, wherein noise level was sometimes high enough to drive SNR below $1dB$. The transmitter, however, was already saturated at the highest power level and could not respond. To show the performance advantage of this intelligent terminal, the optimal case calculated by the decision tree was compared with two static cases: (1) Setting transmission power to maximum (i.e., seven); and (2) Setting transmission

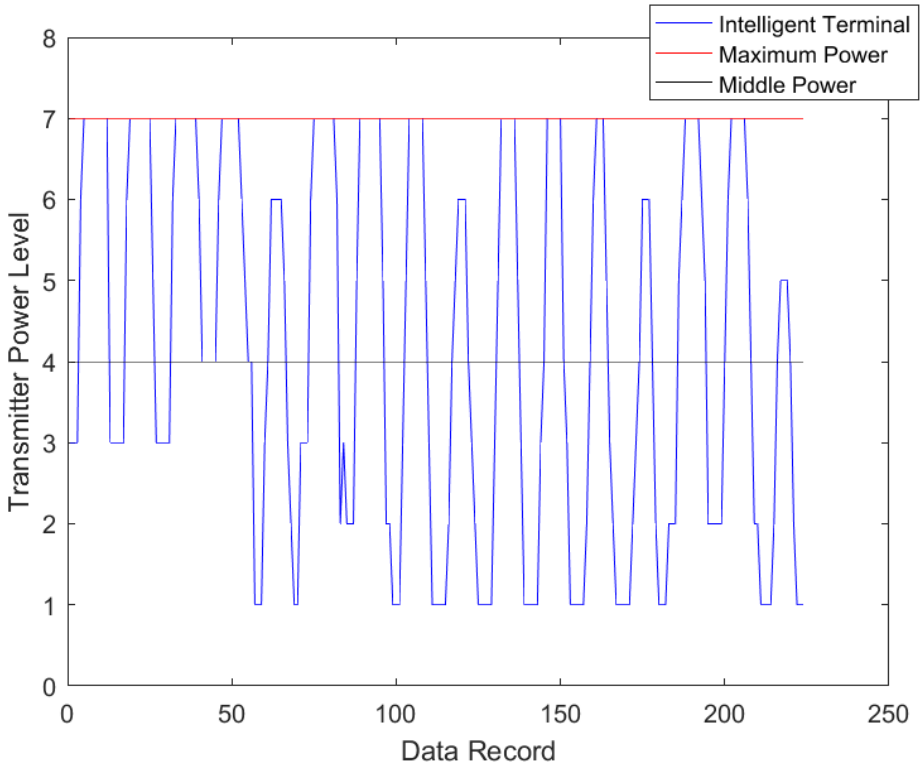


**Figure 6.16. Transmission power levels for the intelligent terminal case, the maximum power case and the middle power case during a complete noise cycle.**

power to the middle (i.e., four). Figure 6.16 compares power levels among these three cases. Table 6.4 shows performance gains of the intelligent terminal in terms of power consumption and SNR. The cognitive terminal was able to match the minimum SNR of the maximum power case while only consuming 61% energy. (Minimum SNR is less than the $1dB$ SNR threshold due to power saturation, as explained earlier.)

**Table 6.4. Performance Gains of the Intelligent Terminal**

| Model | Power Consumption (%) | Minimum SNR ($dB$) |
|---|---|---|
| **Maximum Power** | 100 | -1.14 |
| **Intelligent Terminal** | 61.29 | -1.14 |
| **Middle Power** | 57.14 | -3.23 |

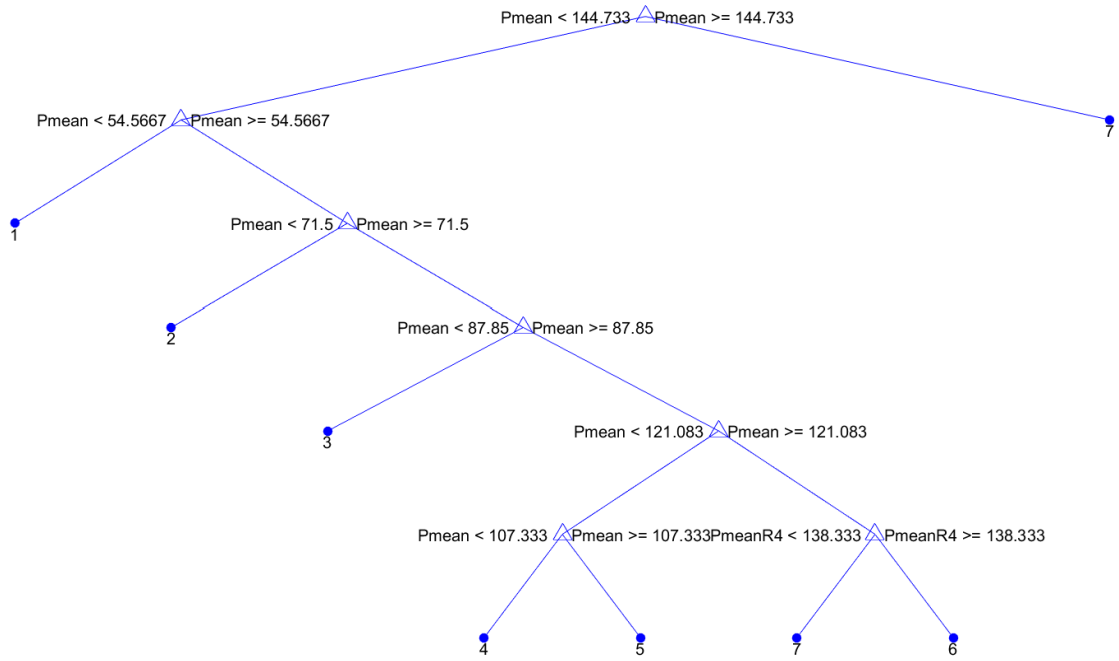


**Figure 6.17. Visualization of the binary decision tree classifier.**

Figure 6.17 visualizes the decision tree model, which has seven splits that makes it easy to implement on small MCUs. The tree classifier picked only first predictor (i.e., total noise mean) and yielded excellent results since the solution is straightforward thresholding. More complex scenarios might utilize more aspects of the data and use more advanced learning algorithms. The purpose of this experiment was to prove machine learning applicability and its ease-of-implementation within software-defined optical terminals built using MOWE architecture.

# Chapter 7: Next Generation MOWE

This chapter speculates about MOWE future by devising a possible development pathway toward better performance and exploring multiple ideas for incorporating MOWE within other technologies and platforms. Section 7.1 presents an innovative design concept that combines MOWE arrays and fiber-optic bundles in a hybrid system to combat misalignment in SWaP-constrained, high-data rate FSO links. Section 7.2 lays down a path toward a raw 1-Gbps MOWE architecture using high-end components and a more sophisticated RX/TX chain design. Section 7.3 discusses possible research directions for and using MOWE. Finally, Section 7.4 presents the concept of *Gnu Optics*, a theorized system that interfaces MOWE with the well-known Gnu Radio platform in order to create a true software-defined optical terminal and utilize Gnu Radio's powerful DSP and digital communication capabilities.

## 7.1. MOWE in a Hybrid System

Although MOWE can be used as a stand-alone system, it is beneficial to explore its incorporation with other technologies with the goal of creating hybrid solutions that offer higher performance and compensate for individual technology shortcomings. A novel concept was explored to combine MOWE with fiber bundles and combat misalignment in SWaP-constrained FSO links, such as the case of the International Space Station (ISS).

### *7.1.1 Problem Statement*

The International Space Station (ISS) is a space station, or a habitable artificial satellite, in low Earth orbit. (See Figure 7.1.) It is arguably the most expensive

device ever made with its cost expected to exceed $150 billion [96]. Payload sites available on the ISS, however, impose significant limitations for communicating large quantities of science data due to the limited throughput of outdated communication bus that was laid down in the 1990s ($\sim 10Mbps$).

One solution could be high data rate FSO links between ISS payload sites and the main cabin. The station, however, constantly undergoes random misalignment caused by rapid thermal changes and astronauts movement. This calls for a specially-designed, alignment-tolerant optical wireless technology. Here are the assumed design requirements for the intra-station FSO link:

- $10m - 20m$ range.
- At or above $1Gbps$ data rate.
- $10cm$ lateral misalignment and $0.2^\circ$ angular misalignment at or below $10Hz$.
- Minimum SWaP.
- Can be easily integrated into the existing ISS hardware.

There are two main mechanical steering technologies that help overcome misalignment: gimbals and fast steering mirrors (FSMs). Gimbals are excluded due to their heavy weight, power consumption, and the unreliability and complexity they add to the system. FSMs have the right level of integration and satisfy low SWaP requirements, but they suffer from small surface area and limited FoV.

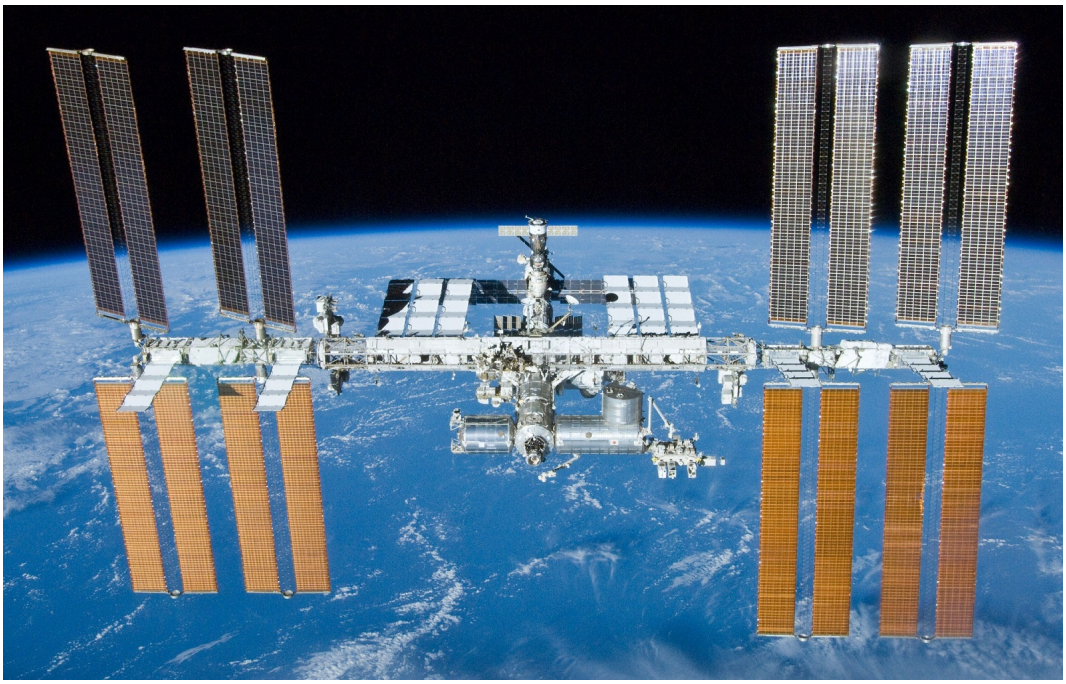

**Figure 7.1. A rearward view of the International Space Station.**

### *7.1.2 Hybrid Optical/Electrical Arrays*

Passive steering, which does not employ any mechanical devices and works instead by switching optical or electrical routes, is a promising solution for the aforementioned challenges. We present here a hybrid design that combines two technologies, MOWE and fiber bundles, into a single optical/electrical array.

Figure 7.2 illustrates array layout and cross-section. Each MOWE detector module is fitted with two optical fibers, one for data transmission and another for data reception. MOWE modules track the optical beam, process measurements locally, and control TX/RX fibers. In doing so they replace the three main components of a traditional closed-loop PAT system: sensing, control and actuation.

As a *sensor*, the MOWE detector array provides a high-resolution upgrade to the common four-quadrant detector (4QD). This results in more accurate tracking and larger terminal coverage. The array is also able to sense the environment and detect and track multiple beams at the same time due to its distributed sensing and computing architecture. This architecture plays an important role in MOWE array functioning as a local *controller*. Not only beam position and characteristics can

be resolved locally with minimum delay but also multiple beams can be detected, tracked or filtered out. Once a control action is determined, the array *activates* the appropriate TX or RX fiber(s) through optical switches.

This novel design eliminates the need for other sensors or controllers and, most importantly, simplifies terminal housing and construction without the need for complex and heavy fiber alignment structure. As can be seen in the cross section in Figure 7.2, the fibers are mounted directly on the module PCB making the array function as a support structure as well. Modularity and cost effectiveness of MOWE arrays transcend to this hybrid design opening the door for wider FoV and curved shell-like terminals.

Figure 7.3 illustrates optical paths in the receiver and transmitter fiber bundles. A mircolens affixed on module PCB collects light from a wide angle and directs it toward the RX fiber. A bundle of RX fibers attach to an array of optical switches and

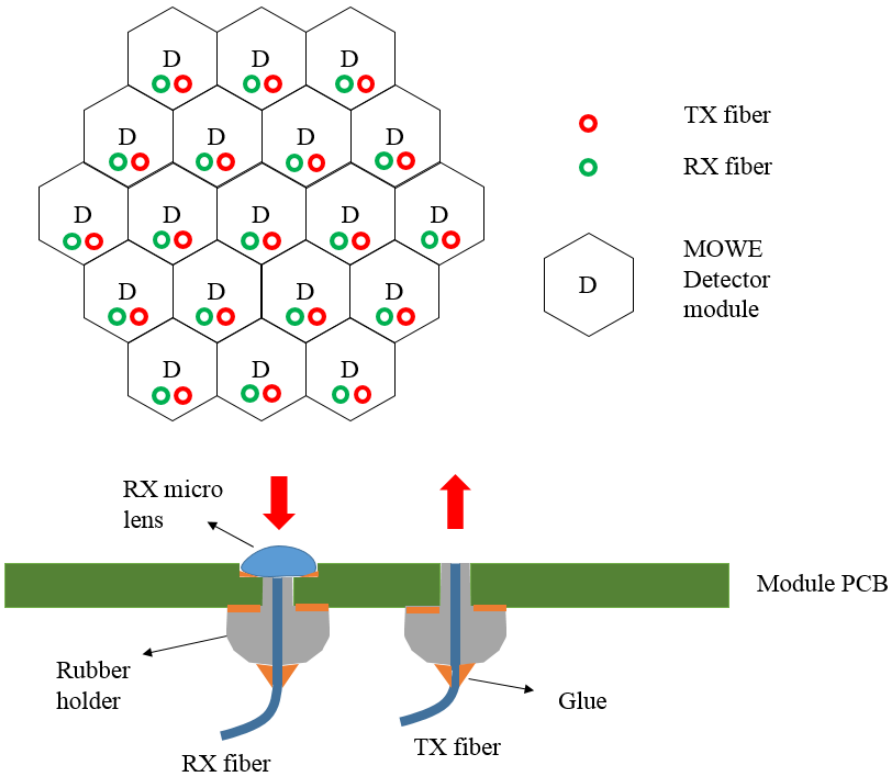


**Figure 7.2. Hybrid optical/electrical array layout (top) and module cross-section (bottom).**

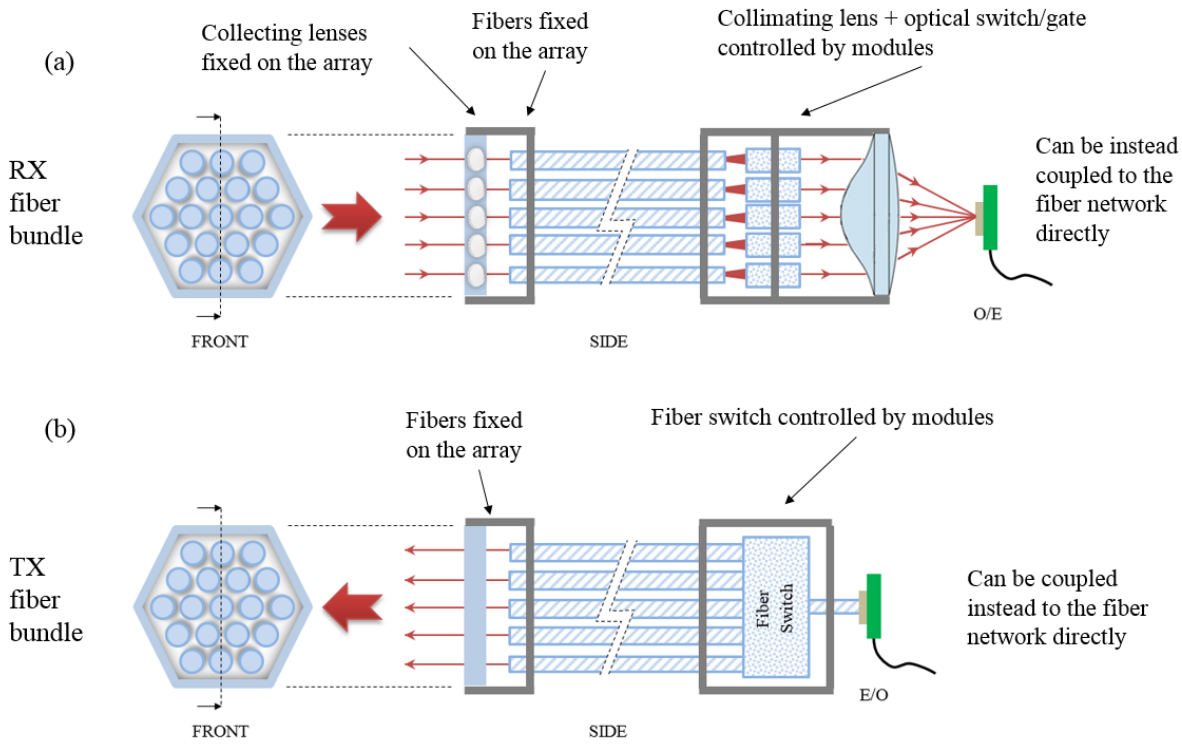


**Figure 7.3. Illustration of fiber-optic paths in the hybrid array. (a) Rx fiber bundle. (b) TX fiber bundle.**

collimating lenses that focus light beams on a convex lens. The latter combines all beams and directs them to a photo-diode or couples them directly to the fiber-optic network. MOWE modules control the optical switches to activate the required set of RX fibers at any given time and block light from others. As for the TX bundle, a VCSEL or a fiber injects the optical signal into another array of optical switches, each connected to a TX fiber. The bundle of fibers leave the TX switch matrix and each fiber attaches to a specific module. A microlens could be also used on top of the TX fiber to control beam spread. MOWE modules control the TX switch matrix, as well, to enable optical switching between single fibers or a group of fibers.

Table 7.1 lists advantages of each technology and shows how MOWE and fiber bundles complement each other to get the best of both worlds. Fiber bundles, as an all-optical system, can easily provide Gbps data rates and couple directly to terrestrial fiber-optic networks with minimum loss. The bundle, however, sums light from all directions and thus suffers from background and adjacent-user interference. MOWE

**Table 7.1. Combining Two Technologies in a Hybrid Optical/Electrical Array**

| | **Fiber Bundles** | **MOWE Array** |
|---|---|---|
| **Data Rate** | • High (all optical design)<br>• Direct coupling to fiber-optic networks. | - |
| **Switching Speed** | High (optical switching) | Switching control signals are fast (processed locally). |
| **Tracking Speed** | - | Fast (fast electrical bus and local processing) |
| **Tracking Accuracy** | - | • High (much higher resolution than 4QD)<br>• Can track spherically. |
| **Total FoV** | Very wide (up to 360°) | Very wide (up to 360°) |
| **Weight** | Lightweight (fibers assembled on the array, no heavy frame needed.) | Lightweight (shell design) |
| **Cost** | No expensive alignment or fixtures. | Can be mass-produced. |
| **Reliability** | Rigid and reliable (no moving parts) | |
| **Interference** | Solves the multi-user/interference problem in all optical terminals. Modules can activate/deactivate specific fibers. | |

modules help solve this problem by decoupling noise and interference and activating only required TX/RX fibers. Although MOWE, at its current specifications, has a limited data rate that does not live up to high-speed optical communication expectations, the data rate is enough to provide required environment sampling, beam tracking, and control tasks among others. It is also possible to establish a low-bandwidth link using MOWE for control, synchronization, and channel equalization, superimposed on the high-bandwidth link carried out by optical fibers.

## 7.2. Toward 1-Gbps Raw Datarate

Although we have demonstrated so far many unique characteristics and useful features that distinguish MOWE from other solutions, e.g., its modularity, design flexibility, the distributed architecture, and the embedded computing among others, there are still performance limitations that prevent MOWE use in high-data rate communication, an essential function for wireless broadband systems. Two main issues stand behind MOWE's modest data rate performance: design complexity and low-end components. The design imperative was to build a functioning, proof-of-concept system at the lowest cost, highest integration, and fastest time-to-market. This called for simplifying receiver and transmitter chains as much as possible and for utilizing low cost, lower-end components such as Cortex-M0 MCUs, embedded ADC, and low-end PTs and LEDs among others. The next two sections discuss possible enhancements around these issues.

### *7.2.1 More Sophisticated RX and TX Chains*

MOWE RX and TX chains were designed with bare minimum components. In part to achieve maximum integration and thus highest optical resolution without expensive miniaturization solutions, but also to isolate the development of firmware and system architecture from challenges concerning optimal design of optical receiver and transmitter paths. Figure 7.4 illustrates typical RX and TX chains (Figure 7.4.a and Figure 7.4.b, respectively) in an experimental 50-*Mbps* diffuse IR link presented by Khan and Barry in [97]. The figure also displays current MOWE RX and TX chains for comparison (Figure 7.4.c and Figure 7.4.d, respectively). A wide-band, wide-angle $850nm$ silicon NPN planar PT is connected to the MCU ADC through a simple current-to-voltage converter (a resistor) in MOWE RX chain. Another option of a $940nm$ PT with a daylight filter is also available. For the TX chain a BJT transistor controlled by MCU GPIO pin drives a narrow-angle $850nm$ infrared emitting diode.

In the diffuse IR link, the transmitter is comprised of a cluster of eight laser diodes with a translucent plastic diffuser shining $475mW$ at $806nm$. A hemispheri-

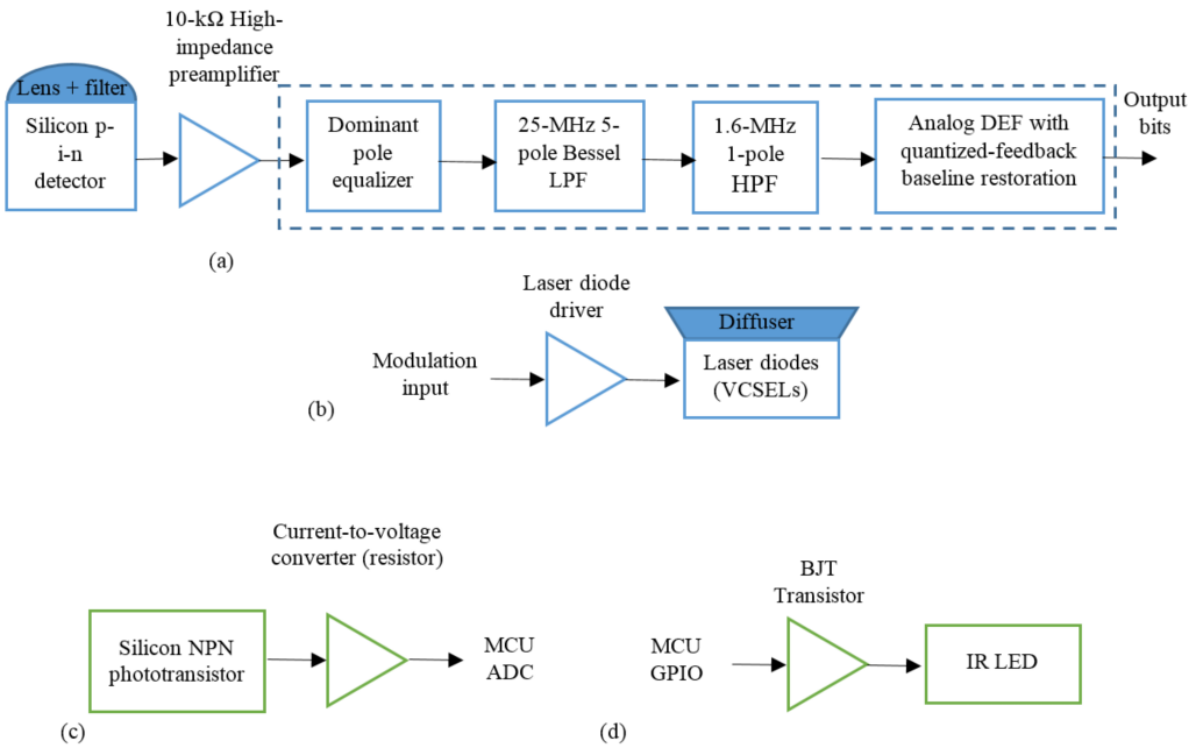


**Figure 7.4. Comparing a typical RX chain (a) and a typical TX chain (b) of a diffuse IR link (reproduced from [97]) with current RX (c) and TX (d) chains in MOWE.**

cal concentrator plus a hemispherical optical band-pass filter with $30nm$ bandwidth combined with 1-$cm^2$ silicon p-i-n detector resulted in a wide-FoV, narrowband receiver. A passive R-C equalizer was implemented to compensate the $455kHz$ pole created by photodiode capacitance in conjunction with a preamplifier load resistance. A 5-pole Bessel low-pass filter compensated for the preamplifier thermal noise, and a single-pole $1.6MHz$ high pass filter removed fluorescent lighting. A decision feedback equalizer (DFE) was employed to reduce multipath inter-symbol-interference (ISI), which is an essential step for diffused links. Note that nearly the entire receiver chain after the preamplifier−shown in dotted rectangle−could be implemented in software. This would require, though, a high-performance processor or an FPGA to execute in real-time.

Recent advances in indoor optical wireless, especially VLC technology benefiting from widespread adoption of LED lighting, have pushed performance limits even fur-

ther with blue-chip white LEDs using advanced pre- and post-equalization techniques and sophisticated OFDMA-derived modulations. Although still heavily experimental, data rates up to 1.6$Gbps$ were achieved on a single-link commercial white phosphorescent LED (1$m$ free-space) using 16QAM-OFDM and a cascaded pre-equalizer to extend the VLC system -3$dB$ bandwidth [98]. Wavelength diversity can be utilized to increase this data rate to several Gbps. An RGB-LED based WDM VLC system achieved 4.5-$Gbps$ (1.5$m$ free-space) using carrier-less amplitude (CAP) modulation and a recursive least square (RLS) equalizer to mitigate ISI [99]. Adding a hybrid post-equalization to an RGBY-LED system pushed the data rate up to 8$Gbps$ (1 m free-space) [100]. Such systems are still quite complicated, bulky, and expensive, but they envisage a near-future when semiconductor-based optical transceivers might reach the performance of fiber-optic communication.

### *7.2.2 High Performance Components*

Two parameters primarily define the maximum data rate at which MOWE arrays can communicate, namely the ADC sampling rate and the internal backbone speed (DMA streams). Maximum sampling rate for STM32F091 MCU is 1-$Msps$ (million sample per second). DMA streaming speed is related to MCU clock frequency and UART baudrate. Maximum streaming rate recorded during experimentation was about 3-$Mbps$ at 0% BER.

DMA streaming speed can be increased using faster MCUs with higher clock frequencies (e.g., Cortex-M4, Cortex-M7 or the high performance Cortex-A9 family). UART serial interface ceases to be useful after about 20-$Mbps$ and GPIO control must be implemented to achieve higher transmission rate. Nevertheless, when approaching the 1-$Gbps$ mark, even the GPIO control in a traditional, high-performance MCU becomes difficult. Therefore, hardware accelerators and FPGAs must be used to manage inter-array communication while a processor core runs the operating system and other algorithms. Figure 7.5 presents an anticipated roadmap for the digital side of MOWE transmitters, given present-day commercial technology.

The most significant roadblock, however, is not in the serial interface. Rather, it is

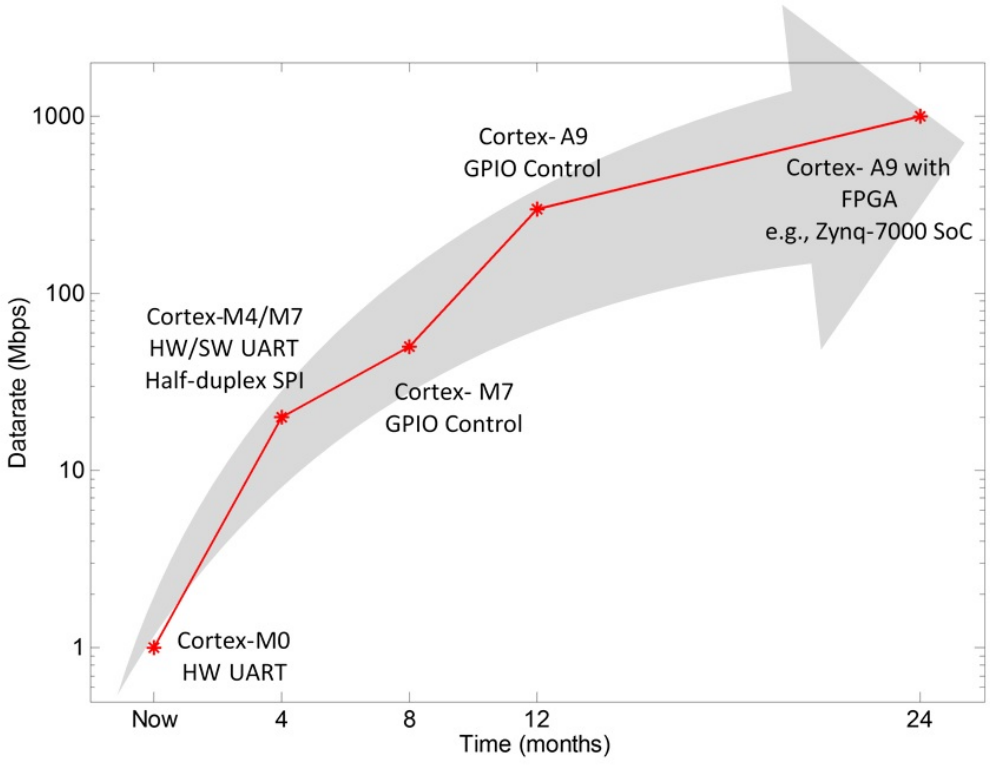


**Figure 7.5. Anticipated digital logic roadmap toward *Gbps*-speed MOWE transmitters using present-day technologies.**

in the ADC, which makes scaling up MOWE receiver's performance a tough challenge. Most MCUs feature low-end embedded ADCs with sampling rates of tens of *Mbps* at best. Fast ADCs are notoriously expensive, with *Gbps*-grade ADCs priced over $300 [101]. Whereas some high-end applications (e.g., a space terminal) might tolerate a $500-MOWE module, the design model described here is simply not sustainable for many others.

Eventually, a designer must make some difficult decisions. If budget does not allow a separate fast ADC per module, multiple receivers might share a single high-speed ADC to lower costs. Doing so, however, will hinder the concept of a single optical point per module and might affect system modularity and flexibility. Another solution might be a hybrid optical/electrical technology like the one presented in the previous section. The dilemma with regard to high cost of fast ADCs is a matter of scale economics: there is simply not enough demand for these high-end devices to drive

their production cost down. If the situation changes in the near future—and it will definitely change driven by the ubiquity of high-speed communication systems—the price tag on this technology might become more reasonable. There is no guarantee, however, that expectations for wireless communication data rates will not continue their exponential growth!

## 7.3. Research Directions

MOWE research and development can be pursued in multiple directions parallel to hardware development discussed in the previous section. For example, the development carried out for MOWE-Tandy simulator can be pushed forward to accurately model the behavior of complex and large arrays. Data streaming, broadcasting, and broad-sampling algorithms should be optimized and tested in hardware, and then ported to the simulator to scale up. The automatic topology generator can also be extended to handle additional topologies and configurations. More firmware APIs and CLI commands will make system design and use even easier for newcomers.

Research leveraging MOWE has endless possibilities. Low-resolution, high-speed optical tracking, for example, is an interesting application. Optical MIMO is a hot research topic that can be tested and prototyped with minimum effort. Distributed sensing and computing, as well as signal processing, are also interesting problems to pursue and test in hardware. MOWE arrays, especially omnidirectional arrays, can be used to measure and characterize background noise, scintillation, and atmospheric attenuation at various environments and across a wide FoV. Optical navigation and localization, as well as remote sensing, are also the kinds of problems that can be prototyped by MOWE after extending its optical capabilities. Last but not least, using MOWE for data communication, albeit the low data rates, provides many research opportunities in areas such as diversity, coding, and cognitive optical communication. A development shortcut by way of devising an interface between MOWE and Gnu Radio, which is a highly-regarded open-source project for all things wireless communication, is conceptualized below.

## 7.4. Gnu Optics

In order to utilize MOWE unique architecture and properties in an actual optical communication link, a certain amount of extensive coding and algorithm development is required. This includes implementing and adapting various modulation, coding, synchronization, error detection, and error correction algorithms, among others. Such development is not only time- and resource-consuming, the ability to execute efficiently on the small, low-power MCUs currently used in MOWE is questionable.

Building a *seamless* interface between MOWE and a great open-source software platform called **Gnu Radio** is suggested. Gnu Radio packs 10+ years of excellent DSP and digital communication software development and tens of thousands of users [48]. Typically, Gnu Radio algorithms run on PCs that are at least 2-3 orders of magnitude more powerful than Cortex-M0 MCUs. A Gnu Radio+MOWE combination (referred to as **Gnu Optics**) will provide a massive amount of resources for researchers to prototype optical wireless communication links using flexible MOWE architecture and extensive Gnu Radio software APIs.

Worldwide, Gnu Radio is the platform of choice for prototyping SDRs. The software interfaces seamlessly with Ettus Research Universal Software Peripheral Radio (USRP) [63]. Gnu Radio, however, was initially designed for RF communication. Hence, very few people have tried to utilize it for optical wireless. Most experiments simply replaced the RF antenna in a USRP with an LED driver to change transmission medium. This is no more than an RF link shifted in frequency and has little to do with software-defined optics. MOWE, on the other hand, offers control over many optical wireless degrees-of-freedom, namely power, wavelength, and angular and spatial diversity.

The following development model is suggested. MOWE will be used as a smart, multi-element optical antenna that can be fitted with algorithms to stream digital data in and out of the antenna, as well as perform basic signal processing, if needed. Gnu Radio running on a PC will receive, process, and transmit back these data points via an Ethernet port. An intermediary node is necessary to interface MOWE

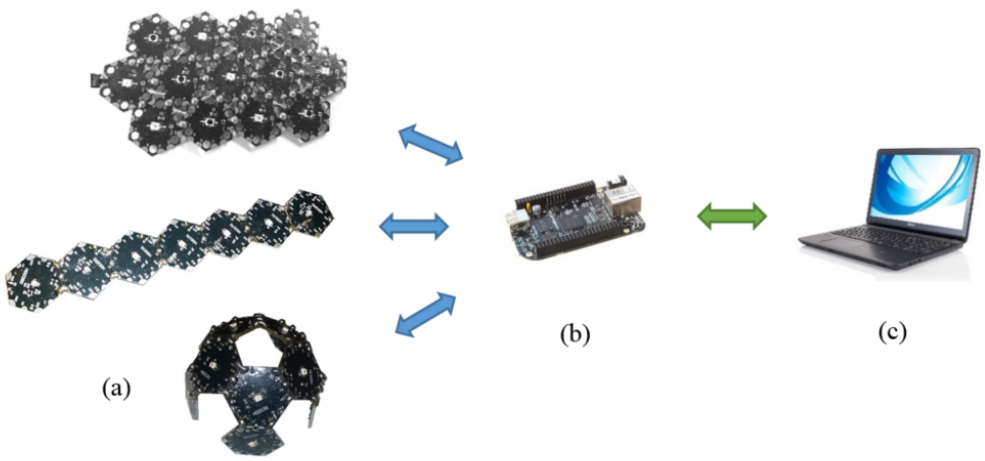


**Figure 7.6. Illustration of Gnu Optics architecture: (a) MOWE arrays function as smart optical antennas. (b) An intermediary interface node connects the arrays to an Ethernet port. (c) A PC running Gnu Radio acts as a central controller processing measurements and executing algorithms.**

arrays with an Ethernet transceiver as efficiently as possible (using DMA streams). Optimally, such a node should be designed using FPGAs. However, for prototyping purpose, a high-performance, IP-enabled computing platform (e.g., BeagleBone or Raspberry Pi) can be used to implement the interface node. The PC would access the node either directly via a client-to-client Ethernet connection or through a router. The same interface node could also be used to run Gnu Radio in the event that a stand-alone system is desired. This architecture is illustrated in Figure 7.6.

Most modulations and algorithms that are specific to optical wireless are not available as part of Gnu Radio. These APIs should be developed along with a special software driver that connects Gnu Radio's UHD interface with the intermediary node. Note that special MOWE arrays will be designed for each experiment. Like when a different RF antenna is swapped for different applications, designers should be able use different MOWE arrays according to application requirements. The system should be able to interface with all arrays regardless of their size or complexity. This dissertation has already illustrated the possibility of this feature via an optical detector array case study. A single reference design, along with coding templates, were used to generate multiple arrays with completely different shapes and configurations.

# Chapter 8: Conclusion

Scholars assert that research should create more questions than answers. This adage is particularly apt for this dissertation, as the project was merely an attempt to challenge some long-standing assumptions about optical wireless communication: that it is expensive, inflexible, immobile, and out-of-reach for many researchers and engineers.

MOWE, the developed solution, provides lightweight, inexpensive, and wide FoV terminals for various applications, ranging from user tracking to broadband connectivity. MOWE architecture was introduced beginning with modules, then arrays and their optical characteristics, and finally terminals. MOWE firmware and electrical/optical specifications have been discussed in detail. The novel architecture was instrumental in defining two original concepts in optical wireless, namely software-defined optics and cognitive optics. Both borrowed from the radio frequency world and adapted to MOWE-based optical terminals.

Demonstrations and examples have been an integral part of this work. Various examples of wide-area detector arrays, including non-flat arrays, were designed and built. Complex scenarios (e.g., intelligent power control using machine learning algorithms or closed-loop, IMU-enabled, passive beam steering) were proposed and implemented. None of the presented experiments was intended to be comprehensive or conclusive, rather to showcase MOWE potentials and applicability to a wide spectrum of ideas and applications.

Finally, a line of research is not complete if it does not consider and anticipate the future. An entire chapter of this work is devoted to future MOWE development and possible integration into other systems seeking high performance and platform agility.

The complete MOWE development platform, including hardware schematics, firmware code, and software tools, is available to the scientific community as open-source materials on MOWE website: http://ouwecad.github.io/MOWE/. I hope researchers, engineers, and students find MOWE useful, whether as a research and prototyping tool, or as an educational platform for various concepts in optical wireless communication, as well as in other domains (e.g., digital signal processing and distributed sensing, among others).

# Bibliography


[1] K. E. Wilson, J. R. Lesh, K. Araki, and Y. Arimoto, "Overview of the ground-to-orbit lasercom demonstration (GOLD)," *Proc. SPIE*, vol. 2990, pp. 23–30, 1997. [Online]. Available: http://dx.doi.org/10.1117/12.273703

[2] R. M. Sova, J. E. Sluz, D. W. Young, J. C. Juarez, A. Dwivedi, N. M. Demidovich III, J. E. Graves, M. Northcott, J. Douglass, J. Phillips, D. Driver, A. McClarin, and D. Abelson, "80 gb/s free-space optical communication demonstration between an aerostat and a ground terminal," *Proc. SPIE*, vol. 6304, pp. 630 414–630 414–10, 2006. [Online]. Available: http://dx.doi.org/10.1117/12.703216

[3] J. Cunningham, D. Foulke, T. Goode, D. Baber, B. Gaughan, M. Fletcher, D. W. Young, J. C. Juarez, J. E. Sluz, and J. L. Riggins, "Long range field testing of free space optical communications terminals on mobile platforms," in *MILCOM 2009 - 2009 IEEE Military Communications Conference*, Oct 2009, pp. 1–7.

[4] "LightPointe Communications, Inc." [Online]. Available: http://www.lightpointe.com/

[5] S. Lee and G. G. Ortiz, "Inertial sensor assisted acquisition, tracking, and pointing for high data rate free space optical communications," in *Lasers and Electro-Optics Society, 2003. LEOS 2003. The 16th Annual Meeting of the IEEE*, vol. 1, Oct 2003, pp. 87–88 vol.1.

[6] "ViaLight Communications GmbH." [Online]. Available: http://www.vialight.de/

[7] "IJK Controls Gyro-stabilized Gimbals." [Online]. Available: http://www.ijkco.com/gyro-stabilized-gimbal-design

[8] "UAV Vision Gyro-stabilized Gimbals." [Online]. Available: http://uavvision.com/

[9] A. Kaadan, H. H. Refai, and P. G. LoPresti, "Multi-element FSO transceivers alignment for inter-UAV communications," *Lightwave Technology, Journal of*, vol. 32, no. 24, pp. 4183–4193, 2014.

[10] J. Katz, "Power combining of semiconductor lasers: A review," Jet Propulsion Laboratory, Report, May and June 1982.

[11] D. F. Welch, "A brief history of high-power semiconductor lasers," *Selected Topics in Quantum Electronics, IEEE Journal of*, vol. 6, no. 6, pp. 1470–1477, 2000.

[12] G. A. Evans, N. W. Carlson, J. H. Abeles, Y. Narayan, M. Ettenberg, and J. K. Butler, "Surface-emitting semiconductor lasers and laser arrays," *Sadhana*, vol. 17, no. 3-4, pp. 355–371, 1992.

[13] L. Jingsi, C. Xiangfei, N. Zhou, J. Zhang, X. Huang, L. Linsong, W. Huan, L. Yanqing, and H. Zhu, "Monolithically integrated 30-wavelength DFB laser array," in *Communications and Photonics Conference and Exhibition (ACP), 2009 Asia*, vol. 2009-Supplement, 2009, Conference Proceedings, pp. 1–6.

[14] A. Rogalski, "History of infrared detectors," *Opto-Electronics Review*, vol. 20, no. 3, pp. 279–308, 2012. [Online]. Available: http://dx.doi.org/10.2478/s11772-012-0037-7

[15] "The Aizenberg Biomineralization and Biomimetics Lab." [Online]. Available: http://aizenberglab.seas.harvard.edu/index.php?show=research_topic&top=3&wh=1920x1017x1920x1080

[16] J. J. Walish, "Bio-inspired optical components," Doctoral Dissertation, Massachusetts Institute of Technology, 2008.

[17] L. P. Lee and R. Szema, "Inspirations from biological optics for advanced photonic systems," *Science*, vol. 310, no. 5751, pp. 1148–1150, 2005. [Online]. Available: http://science.sciencemag.org/content/310/5751/1148

[18] Y. M. Song, Y. Xie, V. Malyarchuk, J. Xiao, I. Jung, K.-J. Choi, Z. Liu, H. Park, C. Lu, R.-H. Kim, R. Li, K. B. Crozier, Y. Huang, and J. A. Rogers, "Digital cameras with designs inspired by the arthropod eye," *Nature*, vol. 497, no. 7447, pp. 95–99, 2013. [Online]. Available: http://dx.doi.org/10.1038/nature12083

[19] U. of California Berkeley, "Tunable doublet lens array." [Online]. Available: http://www.ti.com/product/ads54j60

[20] K.-H. Jeong, J. Kim, and L. P. Lee, "Biologically inspired artificial compound eyes," *Science*, vol. 312, no. 5773, pp. 557–561, 2006. [Online]. Available: http://science.sciencemag.org/content/312/5773/557

[21] J. Shirk, M. Sandrock, D. Scribner, E. Fleet, R. Stroman, E. Baer, and A. Hiltner, "Biomimetic gradient index (GRIN) lenses," *NRL Review*, pp. 53–61, 2006.

[22] D. Zhou, P. G. LoPresti, and H. H. Refai, "Enlargement of beam coverage in FSO mobile network," *Lightwave Technology, Journal of*, vol. 29, no. 10, pp. 1583–1589, 2011.

[23] D. Zhou, Z. Shi, W. Yi, P. LoPresti, and H. Refai, "Evaluation of optical transceivers for mobile FSO applications," in *Proc. SPIE 8380, Atmospheric Propagation IX, 83800B*, 2012, Conference Proceedings, 10.1117/12.919576.

[24] D. Zhou, P. G. LoPresti, and H. H. Refai, "Evaluation of fiber-bundle based transmitter configurations with alignment control algorithm for mobile FSO nodes," *J. Lightwave Technol.*, vol. 31, no. 2, pp. 249–256, 2013.

[25] K. Takahashi and N. Nakajima, "Design and evaluation of fiber direct coupling optical antennas for next generation optical wireless communication systems," in *Broadband, Wireless Computing, Communication and Applications (BWCCA), 2010 International Conference on*, 2010, Conference Proceedings, pp. 129–136.

[26] K. H. Heng, W.-D. Zhong, and T. H. Cheng, "Multipoint free-space optics system for short-range communications between flight platforms," *Applied Optics*, vol. 49, no. 2, pp. 258–266, 2010.

[27] A. M. Brown, D. V. Hahn, D. M. Brown, N. W. Rolander, C.-H. Bair, and J. E. Sluz, "Experimental implementation of fiber optic bundle array wide FOV free space optical communications receiver," *Applied Optics*, vol. 51, no. 18, pp. 3995–4002, 2012.

[28] D. V. Hahn, D. M. Brown, N. W. Rolander, J. E. Sluz, and R. Venkat, "Fiber optic bundle array wide field-of-view optical receiver for free space optical communications," *Optics Letters*, vol. 35, no. 21, pp. 3559–3561, 2010.

[29] W. Yi, "Experimental evaluation of wavelength diversity based on fiber-bundle receiver design," Master Thesis, The University of Tulsa, 2013.

[30] A. Sevincer, M. Bilgi, and M. Yuksel, "Automatic realignment with electronic steering of free-space-optical transceivers in MANETs: A proof-of-concept prototype," *Ad Hoc Networks*, vol. 11, no. 1, pp. 585–595, 2013.

[31] M. Yuksel, J. Akella, S. Kalyanaraman, and P. Dutta, "Free-space-optical mobile ad hoc networks: Auto-configurable building blocks," *Wireless Networks*, vol. 15, no. 3, pp. 295–312, 2009. [Online]. Available: http://dx.doi.org/10.1007/s11276-007-0040-y

[32] M. Bilgi, "Multi-transceiver free-space-optical structures for mobile ad-hoc networks," Doctoral Dissertation, University of Nevada, 2010.

[33] T. Shang, Y. Yang, W. Li, X. Wang, and J. Jia, "An omni-directional optical antenna and its beam control method based on the EC-KPA algorithm for mobile fso," *Optics Express*, vol. 21, no. 2, pp. 2307–2323, 2013.

[34] B. Nakhkoob, M. Bilgi, M. Yuksel, and M. Hella, "Multi-transceiver optical wireless spherical structures for MANETs," *Selected Areas in Communications, IEEE Journal on*, vol. 27, no. 9, pp. 1612–1622, 2009.

[35] M. Bilgi and M. Yuksel, "Multi-element free-space-optical spherical structures with intermittent connectivity patterns," in *INFOCOM Workshops 2008, IEEE*, 2008, Conference Proceedings, pp. 1–4.

[36] M. Bilgi, M. Yuksel, and N. Pala, "3-D optical wireless localization," in *GLOBECOM Workshops (GC Wkshps), 2010 IEEE*, Dec 2010, pp. 1062–1066.

[37] A. Kaadan, D. Zhou, H. H. Refai, and P. G. LoPresti, "Modeling of aerial-to-aerial short-distance free-space optical links," in *Integrated Communications, Navigation and Surveillance Conference (ICNS), 2013*, 2013, Conference Proceedings, pp. 1–12.

[38] A. Kaadan, "A study of unmanned aerial systems stability for lasercom applications," Thesis, School or Electrical and Computer Engineering, 2013.

[39] A. Kaadan, H. H. Refai, and P. G. LoPresti, "Spherical FSO receivers for UAV communication: Geometric coverage models," *IEEE Transactions on Aerospace and Electronics Systems*, vol. 52, no. 4, 2016.

[40] ——, "On the development of modular optical wireless elements (MOWE)," in *2015 IEEE Globecom Workshops (GC Wkshps)*, Dec 2015, pp. 1–7.

[41] P. A. Janmey and D. E. Discher, "Developmental biology: Holding it together in the eye," *Nature*, vol. 431, no. 7009, pp. 635–636, 2004, 10.1038/431635a. [Online]. Available: http://dx.doi.org/10.1038/431635a

[42] H. W. Kroto, J. R. Heath, S. C. O'Brien, R. F. Curl, and R. E. Smalley, "C60: Buckminsterfullerene," *Nature*, vol. 318, no. 6042, pp. 162–163, 1985, 10.1038/318162a0. [Online]. Available: http://dx.doi.org/10.1038/318162a0

[43] Disney, "Visible light communication." [Online]. Available: http://www.disneyresearch.com/project/visible-light-communication/

[44] Fraunhofer Heinrich Hertz Institute, "Optical wireless communication." [Online]. Available: http://www.hhi.fraunhofer.de/departments/photonic-networks-and-systems/research-topics/optical-indoor-networks/optical-wireless-communication.html

[45] Boston University, "NSF Smart Lighting Engineering Research Center (ERC)." [Online]. Available: http://www.bu.edu/smartlighting/

[46] Google, "Balloon-powered internet for everyone." [Online]. Available: http://www.google.com/loon/

[47] Facebook, "Announcing the Connectivity Lab at Facebook," 2014. [Online]. Available: https://internet.org/press/announcing-the-connectivity-lab-at-facebook

[48] "Gnu Radio." [Online]. Available: http://gnuradio.org/redmine/projects/gnuradio/wiki

[49] "OpenVLC," 2016. [Online]. Available: http://www.openvlc.org/

[50] T. Davis, "Geodesic domes." [Online]. Available: http://mathcircle.berkeley.edu/BMC6/ps0405/geodesic.pdf

[51] H. Willebrand and B. S. Ghuman, *Free space optics: Enabling Optical Connectivity in Today's Networks*. SAMS publishing, 2002.

[52] "FreeRTOS." [Online]. Available: http://www.freertos.org/

[53] "Tandy Supercomputing Center." [Online]. Available: http://www.tandysupercomputing.org/

[54] A. Rogalski, "Optical detectors for focal plane arrays," *Opto-Electronics Review*, vol. 12, no. 2, pp. 221–245, 20014.

[55] S.-B. Rim, P. B. Catrysse, R. Dinyari, K. Huang, and P. Peumans, "The optical advantages of curved focal plane arrays," *Opt. Express*, vol. 16, no. 7, pp. 4965–4971, Mar 2008. [Online]. Available: http://www.opticsexpress.org/abstract.cfm?URI=oe-16-7-4965

[56] D. Floreano, R. Pericet-Camara, S. Viollet, F. Ruffier, A. Brückner, R. Leitel, W. Buss, M. Menouni, F. Expert, R. Juston, M. K. Dobrzynski, G. L'Eplattenier, F. Recktenwald, H. A. Mallot, and N. Franceschini, "Miniature curved artificial compound eyes," *PNAS*, vol. 110, no. 23, pp. 9267–9272, 2013.

[57] *"Unequalized passive detection in a flat array"*, visualization. Available at https://goo.gl/rJbphC, [retrieved 1 May 2016].

[58] *"Equalized passive detection in a flat array"*, visualization. Available at https://goo.gl/rJbphC, [retrieved 1 May 2016].

[59] *"Active detection and tracking in a flat array"*, visualization. Available at https://goo.gl/rJbphC, [retrieved 1 May 2016].

[60] *"Detecting two light beams in a flat array"*, visualization. Available at https://goo.gl/rJbphC, [retrieved 1 May 2016].

[61] *"Active object rotating around a spherical array"*, visualization. Available at https://goo.gl/ZsKjkK, [retrieved 1 May 2016].

[62] J. M. Hilkert, "Guest editorial on software radios," *IEEE Journal on Selected Areas in Communication*, pp. 509–512, 1999.

[63] "Ettus research." [Online]. Available: https://www.ettus.com/

[64] M. Channegowda, R. Nejabati, and D. Simeonidou, "Software-defined optical networks technology and infrastructure: Enabling software-defined optical network operations," *J. Opt. Commun. Netw.*, vol. 5, no. 10, pp. A274–A282, Oct 2013. [Online]. Available: http://jocn.osa.org/abstract.cfm?URI=jocn-5-10-A274

[65] J. Mitola, "The software radio architecture," *Comm. Mag.*, vol. 33, no. 5, pp. 26–38, May 1995. [Online]. Available: http://dx.doi.org/10.1109/35.393001

[66] G. Sklivanitis, A. Gannon, S. N. Batalama, and D. A. Pados, "Addressing next-generation wireless challenges with commercial software-defined radio platforms," *IEEE Communications Magazine*, vol. 54, no. 1, pp. 59–67, January 2016.

[67] S. Haykin, "Cognitive radio: brain-empowered wireless communications," *IEEE Journal on Selected Areas in Communications*, vol. 23, no. 2, pp. 201–220, Feb 2005.

[68] J. Mitola and G. Q. Maguire, "Cognitive radio: making software radios more personal," *IEEE Personal Communications*, vol. 6, no. 4, pp. 13–18, Aug 1999.

[69] *Cognitive Radio, Software Defined Radio, and Adaptive Wireless Systems*, ser. Signals and Communication Technology. Springer Netherlands, 2007.

[70] *"Beam Detection & Tracking - Small Footprint"*, visualization. Available at https://goo.gl/4dHZlM, [retrieved 18 September 2016].

[71] *"Beam Detection & Tracking - Large Footprint"*, visualization. Available at https://goo.gl/W7ejhS, [retrieved 18 September 2016].

[72] *"Optical Beam Tracking"*, visualization. Available at https://goo.gl/eXqLNG, [retrieved 18 September 2016].

[73] 2012. [Online]. Available: http://www.dst.se/gimbal/otus-u135

[74] [Online]. Available: http://gyrostabilizedsystems.com/products/c520

[75] J. M. Hilkert, "Inertially stabilized platform technology concepts and principles," *Control Systems, IEEE*, vol. 28, no. 1, pp. 26–46, 2008.

[76] "Fast steering mirrors," 2013. [Online]. Available: http://www.ballaerospace.com/page.jsp?page=103

[77] M. J. Daneman, O. Solgaard, N. C. Tien, K. Y. Lau, and R. S. Muller, "Laser-to-fiber coupling module using a micromachined alignment mirror," *IEEE Photonics Technology Letters*, vol. 8, no. 3, pp. 396–398, March 1996.

[78] K. Ishikawa, J. Zhang, A. Tuantranont, V. M. Bright, and Y.-C. Lee, "An integrated micro-optical system for vcsel-to-fiber active alignment," *Sensors and Actuators A: Physical*, vol. 103, no. 1–2, pp. 109–115, 2003. [Online]. Available: http://www.sciencedirect.com/science/article/pii/S0924424702003138

[79] I.-J. Cho and E. Yoon, "A low-voltage three-axis electromagnetically actuated micromirror for fine alignment among optical devices," *Journal of Micromechanics and Microengineering*, vol. 19, no. 8, p. 085007, 2009. [Online]. Available: http://stacks.iop.org/0960-1317/19/i=8/a=085007

[80] W. Liu, Y. Zhu, K. Jia, W. Liao, Y. Tang, B. Wang, and H. Xie, "A tip–tilt–piston micromirror with a double s-shaped unimorph piezoelectric actuator," *Sensors and Actuators A: Physical*, vol. 193, pp. 121 – 128, 2013. [Online]. Available: http://www.sciencedirect.com/science/article/pii/S0924424712007844

[81] D. V. Hahn;, D. M. Brown;, A. M. Brown;, C.-H. Bair;, M. J. Mayr;, N. W. Rolander;, J. E. Sluz;, Venkat, and Radha, "Conformal free-space optical communications terminal designs for highly confined vehicles," *JOHNS HOPKINS APL TECHNICAL DIGEST*, vol. Volume 30, no. Number 4, 2012.

[82] P. G. Goetz, W. S. Rabinovich, R. Mahon, J. L. Murphy, M. S. Ferraro, M. R. Suite, W. R. Smith, B. B. Xu, H. R. Burris, C. I. Moore, W. W. Schultz, B. M. Mathieu, W. T. Freeman, S. Frawley, M. Colbert, and K. H. S. Reese, "Modulating retro-reflector lasercom systems at the naval research laboratory," in *MILITARY COMMUNICATIONS CONFERENCE, 2010 - MILCOM 2010*, 2010, Conference Proceedings, pp. 1601–1606.

[83] P. G. Goetz, W. S. Rabinovich, R. Mahon, J. L. Murphy, M. S. Ferraro, M. R. Suite, W. R. Smith, H. R. Burris, C. I. Moore, W. W. Schultz, W. T. Freeman, S. J. Frawley, B. M. Mathieu, K. Hacker, and S. Reese, "Modulating retro-reflector lasercom systems for small unmanned vehicles," *Selected Areas in Communications, IEEE Journal on*, vol. 30, no. 5, pp. 986–992, 2012.

[84] O. Topcu, H. Henniger, L. Grobe, M. Haardt, A. Mitschele-Thiel, and T. Simon, "Lightweight, mobile free-space optical communications in disaster scenarios for transmission of earth observation data: feasibility study," in *Proc. SPIE 8162, Free-Space and Atmospheric Laser Communications XI*, vol. 8162, 2011, Conference Proceedings, pp. 816 203–816 203–13. [Online]. Available: http://dx.doi.org/10.1117/12.898800

[85] W. S. Rabinovich, R. Mahon, P. G. Goetz, E. Waluschka, D. S. Katzer, S. C. Binari, and G. C. Gilbreath, "A cat's eye multiple quantum-well modulating retro-reflector," *Photonics Technology Letters, IEEE*, vol. 15, no. 3, pp. 461–463, 2003.

[86] C. Fuchs, "Fine tracking system for aeronautical fso links," in *15th Ka and Broadband Communications, Navigation and Earth Observation Conference*, 2009, Conference Proceedings.

[87] A. A. Portillo, G. G. Ortiz, and C. Racho, "Fine pointing control for optical communications," in *Aerospace Conference, 2001, IEEE Proceedings.*, vol. 3, 2001, Conference Proceedings, pp. 3/1541–3/1550 vol.3.

[88] A. Harris, J. J. J. Sluss, H. H. Refai, and P. G. LoPresti, "Comparison of active beam steering elements and analysis of platform vibrations for various long-range fso links," in *Proc. SPIE 5819, Digital Wireless Communications VII and Space Communication Technologies*, vol. 5819, 2005, Conference Proceedings, pp. 474–484. [Online]. Available: http://dx.doi.org/10.1117/12.603667

[89] 2013. [Online]. Available: http://www.quanta-tech.com/Acousto_optic_products/deflectors.php

[90] N. HENDRICKX, J. VAN ERPS, T. ALAJOKI, N. DESTOUCHES, D. BLANC, J. FRANC, P. KARIOJA, H. Thienpont, and P. Van Daele, "Towards low cost coupling structures for short distance optical interconnections," in *Proceedings of the 16th European Microelectronics and Packaging Conference (EMPC), Oulu, Finland*, 2007, pp. 247–252.

[91] A. C. Lehman, J. J. Raftery, and K. D. Choquette, "Beam-steering in photonic crystal vertical cavity surface emitting laser arrays," in *Semiconductor Laser Conference, 2006. Conference Digest. 2006 IEEE 20th International*, 2006, Conference Proceedings, pp. 77–78.

[92] *"Passive Optical Beam Steering and Control"*, visualization. Available at https://goo.gl/JFKs5n, [retrieved 20 September 2016].

[93] *"Closed-loop Passive Optical Switching & Beam Steering"*, visualization. Available at https://goo.gl/AbZ3Jt, [retrieved 20 September 2016].

[94] InveSense, "MPU-6050 Six-Axis (Gyro + Accelerometer) MEMS MotionTracking Devices." [Online]. Available: https://www.invensense.com/products/motion-tracking/6-axis/mpu-6050/

[95] P.-J. V. de Maele, "Reading a IMU Without Kalman: The Complementary Filter." [Online]. Available: http://www.pieter-jan.com/node/11

[96] "International Space Station." [Online]. Available: https://en.wikipedia.org/wiki/International_Space_Station

[97] J. M. Kahn and J. R. Barry, "Wireless infrared communications," *Proceedings of the IEEE*, vol. 85, no. 2, pp. 265–298, Feb 1997.

[98] X. Huang, Z. Wang, J. Shi, Y. Wang, and N. Chi, "1.6 gbit/s phosphorescent white led based vlc transmission using a cascaded pre-equalization circuit and a differential outputs pin receiver," *Opt. Express*, vol. 23, no. 17, pp. 22 034–22 042, Aug 2015. [Online]. Available: http://www.opticsexpress.org/abstract.cfm?URI=oe-23-17-22034

[99] Y. Wang, X. Huang, L. Tao, J. Shi, and N. Chi, "4.5-gb/s rgb-led based wdm visible light communication system employing cap modulation and rls based adaptive equalization," *Opt. Express*, vol. 23, no. 10, pp. 13 626–13 633, May 2015. [Online]. Available: http://www.opticsexpress.org/abstract.cfm?URI=oe-23-10-13626

[100] Y. Wang, L. Tao, X. Huang, J. Shi, and N. Chi, "8-gb/s rgby led-based wdm vlc system employing high-order cap modulation and hybrid post equalizer," *IEEE Photonics Journal*, vol. 7, no. 6, pp. 1–7, Dec 2015.

[101] Texas Instruments, "Dual channel 16-bit 1.0 GSPS analog to digital converter." [Online]. Available: http://biopoets.berkeley.edu/category/biologically-inspired-optical-systems/

# Chapter A: Nomenclature

| Symbol | Unit | Description |
|---|---|---|
| $d$ | $m$ | Optical resolution |
| $\theta_r$ | $radian$ | PD/PT angle of half sensitivity |
| $s$ | $m$ | Hexagon/pentagon side length |
| $d_{rr}$ | $m$ | Receiver contact distance |
| $d_{Rr}$ | $m$ | Receiver convergence distance |
| $r_r$ | $m$ | FoV cross-section radius at the contact distance |
| $R_r$ | $m$ | FoV cross-section radius at the convergence distance |
| $MAA$ | $mm^2$ | Maximum Aperture Area |
| $h$ | $m$ | Vertical distance from a given plane to module surface |
| $TAA$ | $mm^2$ | Total Aperture Area |
| $TAA_{\%}$ | % | Percentage Total Aperture Area |
| $BlindSpots_{\%}$ | % | Percentage Blind Spots Area |
| $v$ | $m/sec$ | Node velocity |
| $t_{off,max}$ | $sec$ | Maximum blockage time |
| $d_{rt}$ | $m$ | Transmitter contact distance |
| $d_{Rt}$ | $m$ | Transmitter convergence distance |
| $r_t$ | $m$ | FoR cross-section radius at the contact distance |

| | | |
|---|---|---|
| $R_t$ | $m$ | FoR cross-section radius at the convergence distance |
| $\theta_t$ | $radian$ | LED FWHM divergence angle |
| $\alpha$ | $radian$ | Tilt angle between two modules |
| $R_L$ | $\Omega$ | PT load resistor |
| $S$ | $dBm$ | Receiver optical power sensitivity |
| $P$ | $dBm$ | Transmitter optical power |
| $A_L, A_G$ | $dBm$ | Atmospheric, Geometric attenuation |
| $\sigma$ | $km^{-1}$ | Attenuation coefficient |
| $\lambda$ | $nm$ | Wavelength |
| $V$ | $km$ | Atmospheric visibility |
| $q$ | - | Size distribution of the scattering particles |
| $\zeta$ | $cm$ | Receiver radius |
| $\gamma$ | $cm$ | Transmitter radius |
| $R$ | $m$ | Communication range |
| $I_{c_{min}}, I_{c_{max}}$ | $A$ | Minimum, maximum PT collector light current |
| $X_{COI}, Y_{COI}$ | $mm$ | Beam center-of-intensity (COI) Cartesian coordinates |
| $X_{arr}, Y_{arr}$ | $mm$ | Array center Cartesian coordinates |
| $X_i, Y_i$ | $mm$ | Module $i$ Cartesian coordinates |
| $\Delta X, \Delta Y$ | $mm$ | Distance error between array center and beam COI |
| $I_i$ | ADC counts | Received intensity at module $i$ |
| $arm$ | $mm$ | Distance from array center to terminal center-of-rotation (COR) |
| $\Psi$ | $^\circ$ | Array azimuth angle |
| $\Theta$ | $^\circ$ | Array elevation angle |

| | | |
|---|---|---|
| $\theta_{mx}, \theta_{my}$ | $radian$ | Output laser beam optical displacement angles |
| $\theta_{Bx}, \theta_{By}$ | $radian$ | Incoming laser beam optical displacement angles (due to turbulence) |
| $\theta_{Nx}, \theta_{Ny}$ | $radian$ | Course pointing platform (CPA) mechanical disturbance |
| $v_{mx}, v_{my}$ | $volt$ | FSM input voltages |
| $K_x, K_y$ | $radian/volt$ | FSM response |
| $FCI$ | | Fiber Coupling Index |
| $K_{FC}$ | $radian^{-1}$ | Fiber coupling coefficient |
| $\theta_{max}$ | $radian$ | Maximum displacement angle |
| $K_{FSM}$ | $radian/volt$ | FSM single-axis steady-state gain |
| $J$ | | LQR performance index (PI) |
| $Q$ | | LQR states weight factor |
| $R$ | | LQR inputs weight factor |
| $A, B, C$ | | States space system, input, output matrices |
| $S$ | | Arithmetic Riccati equation (ARE) variable |
| $K_{opt}$ | $volt/radian$ | LQR optimal gain |
| $u_t$ | $volt$ | FSM control signal |

# Chapter B: Navigating the Website

MOWE is hosted on the well-known code sharing website GitHub. The website home page is available here http://ouwecad.github.io/MOWE/ where one can read a short introduction and browse through projects and publications. Three buttons on the top of the page enable users to reach the project GitHub site available at https://github.com/OUWECAD/MOWE or download the entire repository as a .zip or .tar.gz file.

In the MOWE GitHub site, users can access and download project repository from the *Code* section, review and submit issues in the *Issues* section, submit pull requests from the *Pull requests* section to merge their modified code in the main repository, and learn about platform fundamentals and example projects in the *Wiki* section.

## Repository

MOWE repository contains the following folders and documents:

- **Compiled Test Firmware**: This folder contains various pre-compiled firmware files (.hex files) that can be directly downloaded to individual modules for testing purposes. Both RTOS and Non-RTOS versions are available for all module types.

- **Documentation**: This folder contains some presentation, posters, and papers about MOWE. Links to other publications are available on the website home page as well.

- **Firmware**: The Firmware folder contains the actual code for an individual

module that can be used as code template for project development. Both RTOS and Non-RTOS versions are included.

- **Hardware**: This folder contains schematics and mechanical specification for all available modules as well as data sheets for some of the electronic components.
- **Projects**: Various projects are available as design examples. Each project has a dedicated wiki page to showcase its setup and implementation. The project folder contains firmware code as well as other materials, (e.g., pictures and videos, MATLAB code, and 3D design files among others).
- **Tools**: The Tools folder contains software tools useful for MOWE development such as *MOWE Automatic Topology Generator* and the *ST Flash Loader Demonstrator* used to update module firmware via bootloader. The folder also contains topology files for various arrays.
- **LICENSE**: This file contains the MIT license as well as the copyright notice and disclaimer statement.
- **README.md**: A ReadMe file introducing MOWE and project home page.

### License